2019

A Complete Approach to Predict Biodistribution of Nanomaterials Within Animal Species from In-vitro Data

Edward Price
University of Central Florida

A COMPLETE APPROACH TO PREDICT BIODISTRIBUTION OF NANOMATERIALS WITHIN ANIMAL SPECIES FROM IN-VITRO DATA

by

EDWARD PRICE

B.S. University of Central Florida, 2014

M.S. University of Central Florida, 2016

A dissertation submitted in partial fulfillment of the requirements
for the degree of Doctor of Philosophy
in the Department of Chemistry
in the College of Sciences
at the University of Central Florida
Orlando, Florida

Spring Term

2019

Major Professor: Andre Gesquiere

ABSTRACT

Smart drug-design for antibody and nanomaterial-based therapies allows for optimization of drug efficacy and more efficient early-stage pre-clinical trials. The ideal drug must display maximum efficacy at target tissue sites, but to track and predict distribution to these sites, one must have a mechanistic understanding of the kinetics involved with the individual cells of the tissue itself. This process can be tracked through biological simulations coupled with in-vitro approaches, which result in a rapid and efficient in-depth understanding of drug transport within tissue vasculature and cellular environment. As a result, it becomes possible to predict drug biodistribution within live animal tissue cells without the need for animal studies. Herein, we use in-vitro assays to translate transport kinetics to whole-body animal simulations to predict drug distribution from vasculature into individual tissue cells for the first time. Our approach is based on rate constants obtained from an in-vitro assay that accounts for cell-induced degradation, which are translated to a complete animal simulation to predict nanomedicine biodistribution at the single cell level. This approach delivers predictions for therapies of varying size and type for multiple species of animals solely from in-vitro data. Thus, we expect this work to assist in refining, reducing, and replacing animal testing, while at the same time, giving scientists a new perspective during early stages of drug development.

ACKNOWLEDGMENTS

I would like to express my gratitude to my advisor Professor Andre Gesquiere for his support of my research, as well as his patience and input to all of the work done herein. He helped guide me in the right direction and develop a better writing style.

I would also like to thank the rest of my thesis committee, Drs. Matthew Rex, .Dmitry Kolpashchikov, Steven Ebert, and Qun Huo for their support in this project. Also, thank you to my parents and Hosanna for dealing with the long hours and early mornings.

TABLE OF CONTENTS

LIST OF FIGURES

ACRONYMS/ABBREVIATIONS

AAS Atomic Absorption Spectroscopy

CC Cell Control

CKD Cell Kinetics Data

CSI Cell System Interactions

DRF Dose Range Finding

EPA Environmental Protection Agency

FBS Fetal Bovine Serum

FDA Food and Drug Administration

ICHS International Conference on Harmonisation of Technical Requirements for Registration of Pharmaceuticals for Human Use

MPE Media and Protein Effects

MPS Mononuclear Phagocytic System

NAM New Approach Methodology

NIEHS National Institute of Environmental Health and Safety

NIH National Institutes of Health

NHP Non-Human Primate

NM Nanomedicine

NNI National Nanotechnology Initiative

PBPK Physiologically-Based Pharmacokinetics

PS Polystyrene

QD Quantum Dot

QSH CdSe Quantum Dot

RCF Ratiometric Calibrated Fluorescence

CHAPTER I. INTRODUCTION

Nanomedicines (NMs) like antibodies and synthetic nanomaterials are an attractive development to complement conventional small molecule medicines due to their active tissue targeting, variable circulation time, adjustable biodistribution, and added stability, all stemming from their inherent physical properties*(1, 2)*. Medical applications of these NMs as well as growing presence in consumer products has made these nanomaterials ubiquitous in our daily lives*(3)*. These developments both increases chance of exposure to these materials and brings the need for robust high-throughput methodologies to assess and quantify NM biodistribution accurately *(4-6)*. Current methods to determine NM biodistribution in the blood supply often require animal sacrifice and tissue resection for further processing *(7)*. This develops a severe dependence on animal testing, where empirical quantitative values of mass of NM per mass of tissue are obtained. This approach, however, brings questions about ethics and surges in time and cost *(8)*. This process is time-consuming and requires substantial resources, as often only one time point is available per animal*(9)*. Furthermore, variations in physicochemistry and the number of cells in the body (approximately 200 types and $3x10^{13}$ cells*(10)*) create an impossible workload for conventional quantitative histological analysis to keep up with the rapid expansion of NM usage. Moreover, direct in vivo tissue dose analysis may be difficult to quantify, as biological matrix interferences*(11)* may mask delivered dose to individual cells of a particular tissue*(12)*. This matrix interference, as well as the destruction of tissue architecture eliminate critical knowledge of NM transport within the tissue cells and vasculature.

Increased NM exposure poses additional risks, as biodistribution can cause toxic, innocuous, or therapeutic (in the case of drug development) effects, depending on cellular exposure dose at tissue sites. This exposure dose (or NM biodistribution) is heavily dependent on NM

physicochemistry*(13, 14)* as well as cell type*(15)*. "Smart nanomedicine" can be used to adjust physicochemical properties in order to control the dose delivered to individual target and peripheral tissue cells to achieve maximum efficacy and minimal toxicity during pre-clinical and clinical development, as well as develop products in consumer goods that may not be harmful upon exposure to adults or small children. Government agencies such as the National Institutes of Health (NIH) and the Environmental Protection Agency (EPA) have created The National Nanotechnology Initiative (NNI) in 2001 as a consortium of twenty government agencies to improve human health and standard of life, strengthen the U.S. economy, create jobs, and support national defense*(16)*. Recently, NNI members collaborated and developed a triennial strategy focused on betterment of these priorities. Four goals were articulated:

1. Advance a world-class nanotechnology research and development program through,
    a. Advancing basic science and applications research
    b. Strengthening interdisciplinary research through merging various areas of science and technology
    c. A cultivation of new approaches that include data analytics and modeling and simulation
2. Promote the transfer of new technologies into products for commercial and public benefit
3. Advance nanotechnology through development and maintenance of educational resources, workforce, and toolsets and infrastructure.
4. Support responsible development of nanotechnology

Additionally, Nano-EHS at NIH (NIEHS) outlined a strategy*(17)* to establish a NM measurement infrastructure that produces reproducible data coupled with predictive modeling to assess human exposure. Concerns have also been raised by the US EPA*(18)* and the Food and Drug Administration (FDA)*(19)*, calling for the development of new approach methodologies (NAMs) to

help develop and implement alternative test methods and strategies to “reduce, refine, and replace” vertebrate animal testing. Thus, we cannot perform pre-clinical and clinical trials on every existing NM in the market on animals, so we need a way to predict and assess human safe exposure before running these time-consuming trials. This can be addressed through in-vitro and in-silico methods, which we addressed herein. This combination could direct early prioritization of in-vivo testing for increased efficiency and assist in understanding dosing regimens and potential toxic response *(20)*. This proposed methodology can also address current guidelines for animal safety testing set by the International Conference on Harmonisation of Technical Requirements for Registration of Pharmaceuticals for Human Use (ICH S5) wherein they require investigation of hazardous materials using minimal animal testing. Cross-species capabilities is critical to capture as well as e.g. non-human primates (NHP) do not undergo dose range finding (DRF) studies, so it is critical to be able to predict what dose can be given to an NHP in order to deliver the correct quantities to a desired tissue before actually running these tests. Thus, our work focuses heavily on implementation of flexible in-vitro analysis for 1) extrapolation to animal species with 2) cross-species capabilities.

Simulation-based approaches provide a means of mechanistically tracking the transport of conventional small molecule drugs in human and animal tissues*(21)* in order to guide a more efficient drug development process*(22)*. This is feasible through physiologically based pharmacokinetic (PBPK) models, but their development often requires data from vertebrate animals for a fitted description of outcomes rather than a fully predictive approach*(23)*. These simulations, when constructed for NMs, are often descriptive of empirical animal biodistribution data and assume immediate diffusion of drug from blood to whole tissue based on partitioning coefficients, k_p*(24-30)* estimated from animal (in-vivo) datasets. This assumption is not

descriptive of real processes involved in NM transport from the interstitial space to the cellular environment, as for a NM to reach the cells within a tissue, it must primarily pass through gaps (fenestrations) in tissue vasculature, which will vary in size and quantity depending on the tissue diseased state and type. These fenestrations as well as NM physicochemistry both dictate the critical transport of the drug through the micro-vessel wall into infected or normal tissue cell environment. This complexity is compounded due to the fact that the body is a working system filled with tissues of variable vasculature porosity and diameter that are highly dependent on diseased state and tissue type. Furthermore, tissue cell types will all interact with the NMs differently, affecting delivered dose. Thus, general tissue-blood partitioning is not sufficient to describe NM-biological interactions and needs substantial improvement. Moreover, the micro vessel endothelial cells as well as epithelial tissue cells interact with these NMs primarily through active transport through endocytotic or phagocytic pathways unless they are ultra-small*(31-33)(34)* (**Fig. 1a**).

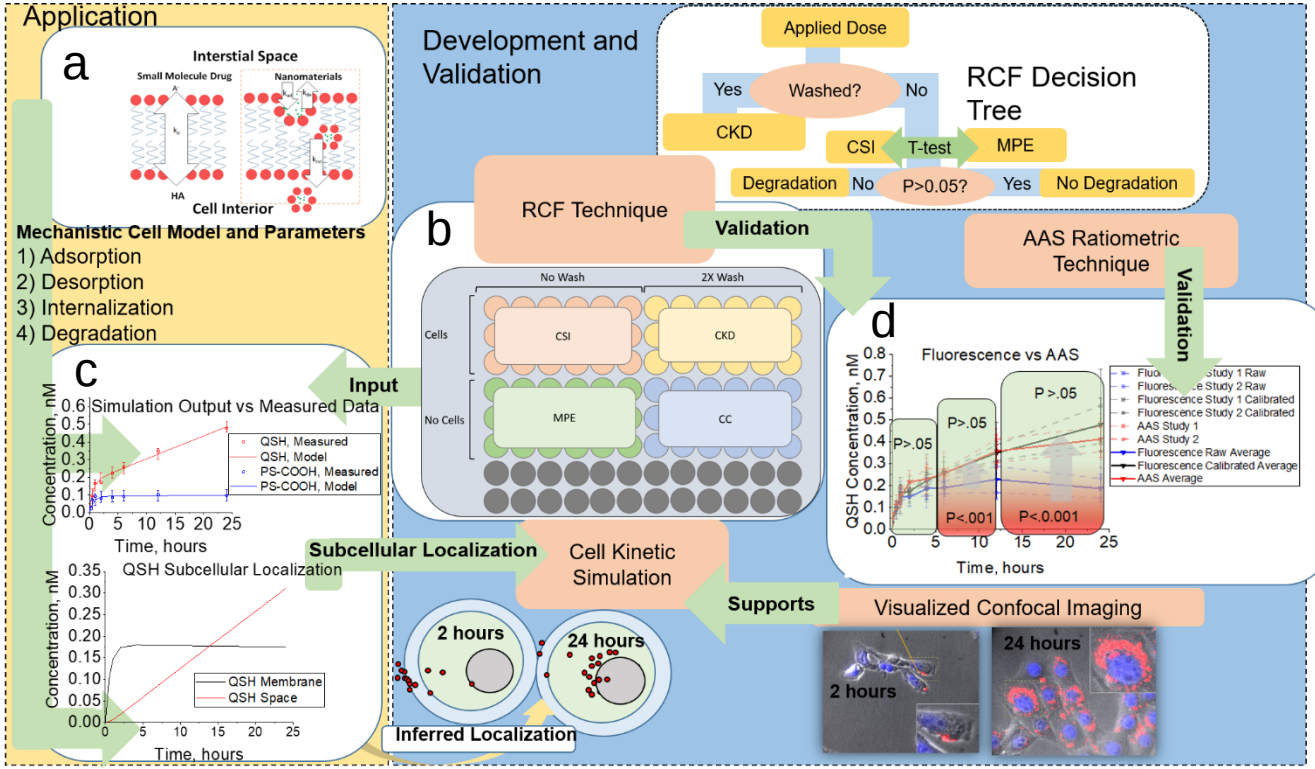

Figure 1. Schematic overview of fluorescence assay. The RCF assay is coupled to an in-vitro kinetics simulation. . (**a**) Traditional partition coefficients (k_p) commonly used for small molecule partitioning between blood supply and cell interior. For NMs, rate constants for adsorption (k_{ad}), desorption (k_{de}), internalization (k_{int}), and degradation (k_{deg}) more accurately represent uptake processes incident on a NM when exposed to cell environment. (**b**) Layout of RCF assay, including CSI compartment (ratiometric standard and descriptive of cellular degradation), CKD compartment (descriptive of kinetics of NM-cell interactions), MPE compartment, (descriptive of media degradation), and CC compartment (descriptive of control with cells without NM exposure). The RCF decision tree illustrates how these are connected in the assay. RCF outputs were then used to build a simulation (**c**) with parameters descriptive of adsorption, desorption, internalization, and degradation pathways. Data from RCF was also (**d**) validated to AAS outputs.

Thus, the reliance of current NM PBPK models on estimation of tissue and blood k_p from experimental animal data*(27, 28, 35)* make them empirically descriptive as well as eliminate the scientific merit of understanding what is occurring between, vasculature, interstitial space, and individual tissue cells, while limiting their predictive power. These obstacles often leave scientists uncertain if a drug will exhibit optimal plasma pharmacokinetics, reach tissue vasculature, interact with epithelial tissue cells, and exhibit desirable effects in pre-clinical or human trials and has long been overlooked for NM development. In order for us to truly understand and predict if a NM will reach cells localized within a tissue, simulations must thus be built on mechanistic fundamental processes involving real mechanistic transport of these materials.

Current software models are still lagging with respect to tracking the mechanistic processes involved in transport of these materials within the tissue and blood supplies. These simulation-based approaches*(21)* have proven to be a possible solution to solve this growing problem, as they have proved successful for predicting biodistribution in animals for the small molecule market*(22)*. Efforts have been made using simulations to account for paracellular transport processes through vascular reflection coefficients (σ_v) representative of fenestrations in endothelial vasculature, but are constrained by their optimization to NMs of one particular size*(36-38)* , assume only two tissue pore sizes, and require fitting to animal datasets. This impedes predictive capabilities, as variations in NM diameter, changes in animal species, and differences in tissue or diseased states can alter the vessel diameters, which then causes the reflection coefficient to change, thereby requiring further animal testing*(39)*. Moreover, the unique NM transport properties that dictate interactions within cells of a tissue*(31-34)* are currently addressed through time-dependent cell permeation*(40)* and in-vitro macrophage rate kinetics*(41)*, but current simulation approaches still treat tissues as a “black box” without the critical epithelial or

endothelial cell content. This imposes a substantial burden for the replacement, refinement, and reduction of animal studies for all current NM PBPK simulations*(28, 40)*, as running animal experiments for every NM type in the market for safety is not feasible*(42)*. Some studies have, however, utilized in vitro assays to quantify dose-response accurately and successfully matched in vivo dose-response upon inhalation of NM particles*(43)*. To achieve in-vivo predictive capabilities for NMs, simulations must 1) be built from the ground-up using in-vitro methods and 2) represent mechanistic biology involving cell-NM rate-driven transport kinetics. Such information is difficult to obtain with routine in-vitro techniques for high-throughput analysis*(44-47)*, and often times, cell-induced degradation of the NM itself is overlooked. Thus, a means of rapid screening of these materials can assist in providing an integrated high throughput approach to quantitatively predict NM biodistribution in preclinical and clinical species to aid in rapid NM development and to protect human health through estimation of exposure dose in single cells of a tissue. In-vitro methods could help address these knowledge gaps, but so far there exists a limited connection between in-vitro quantitative outputs and in-vivo biodistribution. The reason is that data obtained in cell and animal studies are primarily observational quantities acquired from tissue homogenization. Different studies also tend to be based on different methods that are difficult to quantitatively correlate, for example flow cytometry and atomic absorption spectroscopy (AAS).

In-vitro techniques can help bridge the current knowledge gap through mechanism-based models, specifically assays that show translational capabilities across multiple species. However, in-vitro bioassay information may be difficult to translate into a context where the data can be useful for assessing human health. This problem is outlined specifically in a paper published by a consortium of academics and industry partners *(48)* wherein they state that mechanism-based approaches can provide better information for regulatory decision-making. If in-vitro/in-silico

studies yield optimal dose/response profiles in-vivo, DRF studies may be minimized, which can reduce animal testing substantially. Delivery of NM dose to tissues occurs inside individual cells, which are primarily responsible for toxic response. Lack of cellular resolution thus severely hinders accurate prediction of biodistribution and subsequent toxic response. In vitro dose-response connections have been successfully extrapolated to in vivo toxicity data for the respiratory tract using simulations*(49)* through the use of the Multiple Path Particle Dosimetry (MPPD) model. Here, dose-response modeling successfully connected in-vitro predicted outputs to animal measured outputs. However, once a NM deposits onto the respiratory tract, it will also absorb into the blood supply*(50)* where it poses a new set of potential toxic effects on a variety of organs including liver and kidney*(51-54)* . For instance, there is evidence of human exposure and death due to systemically absorbed Ni-based nanoparticles post-inhalation exposure, including severe toxicity in kidneys *(55)*. Such cases suggest the need for not only predicting deposition and delivered dose to cells of the respiratory tract, but the need to track systemic distribution of NMs after inhalation, oral, or intravenous exposure*(56)*. Currently, no PBPK NM systemic simulation model exists for translation of systemic tissue and cell circulation to address this issue.

Experimental results that can 1) give knowledge on particular cell uptake processes and 2) provide mechanistic translational cell kinetics that can be used to understand how and why a particular NM can get around an animal are key in connecting in-vitro data to animal biodistribution. Current efforts have attempted this for tissue macrophages, but are still in development for tissue epithelial cells*(41)*. Tissue epithelial cells are crucial to consider, as they are the fundamental unit of a tissue and are responsible for the primary interactions of NM with whole-tissue. Currently, whole-tissues are looked at as a black box with no additional resolution,

which limits predictive capabilities for those performing in-vitro and in-vivo testing. A combination of high-throughput in-vitro methods and predictive computational models can help bridge the gap between in-vitro cell uptake results and in-vivo biodistribution *(4, 5, 22, 57)*. This could provide an avenue towards reduction of animal testing.

Here, we report a series of experiments to systematically and precisely predict NM biodistribution in multiple species of animals at the single cell level from in-vitro data alone. Essentially, it is a combination of a high-throughput quantitative fluorescence in-vitro assay (**Fig. 1b**) coupled with a cell simulation (**Fig. 1c**) that uses an artificial intelligence algorithm*(58)* to optimize rate constants representative of an average of individual tissue cell interactions with a NM. Our method quantifies the kinetics of mechanistic biological processes (adsorption to cell membrane, desorption from cell membrane, internalization, and degradation) for NMs with single cells to obtain rates quantitatively descriptive of their interaction with the cells, which we validated by Atomic Absorption Spectroscopy (**Fig. 1d**). So far, the issue of degradation on the fluorescent signal given off by NMs has been difficult to address when using fluorescence as a tool for uptake quantification in-vitro*(59)*. Thus, the in-vitro fluorescence assay takes into account effects of cell-induced and media induced degradation through ratiometric analysis (ratiometric calibrated fluorescence, or RCF).*(60)* We demonstrated this capability through the use of degradable quantum dots (QSH)*(61)*, and compare the results with stable dye loaded polystyrene NMs (PS-COOH) in the first phase of experiments. To truly understand how physicochemistry can affect raw data obtained from the RCF assay, we studied a library of compounds with differing cores. Here, we answered questions on how differences in size and charge can affect uptake as well as if the uptake processes are primarily first order at exposure doses given in-vivo. This is critical, as animal studies often utilize materials of differing 1) type, 2) charge, and 3) size, so an understanding of these contributions is needed in order to proceed with any assumptions made

herein. Once biochemical analysis was completed for the library, the RCF assay was run to quantify uptake of fluorescent quantum dots (QDs) in cells commonly encountered in living tissue (liver, kidney, endothelial, and macrophage). Data from the in-vitro RCF assay fed directly to the cell simulation to extract rate kinetics involved in mechanistic biological processes. These kinetics included NM adsorption to cell membrane (k_{ads}), desorption from cell membrane (k_{des}), internalization (k_{int}), and degradation (k_{deg}), which are central to cell interaction with NMs. Thus, the this full in-vitro/in-silico approach gives vital information on factors including 1) NM stability, 2) quantitative kinetics of cellular uptake, and 3) localization with subcellular resolution that can be transferred to in-vivo simulations.

The above kinetic rate constants were extracted from these NM-tissue cell interactions in-vitro and translated through mechanistic biology to deliver a fully predictive animal simulation of drug biodistribution with cellular resolution within tissues. The in-vitro rate kinetics for an averaged population of tissue cells obtained from the in-vitro portion of this work were translated to simulations built for multiple species of animals including mice, rats, and NHP according to their tissue volumes, cellular content, and blood flow rates.

Our approach solves problems with current in-vitro analytical approaches for quantitation of cellular NM content, where results are difficult to translate directly to animal studies and lack mechanistic perspective*(44-47)*. We also addressed current issues with cell-induced degradation of NM fluorescence that is often overlooked, which can produce false negatives*(59, 60)*. Validation of our in-vitro work was performed through simulated lysosomal analysis coupled with Atomic Absorption Spectroscopy (AAS). Lastly, our in-vivo simulation was validated against published whole-body animal data for rats, mice, NHP as well as single cell data. QDs were used

as a model system because of their known potential in nanomedicine while also considering their limitations such as degradation under acidic conditions with cadmium leakage from the core. We show here that we are able to fully account for the complexities in such a NM platform, and we fully extended this capability to antibody and metal/polymer based NMs.

This research significantly improves on current scientific understanding through the now ability to translate data from cell studies to full animal cell uptake for calculation of in vivo target cellular dose, with cross-species translation. This high-throughput makes significant advancements toward reduction of experimental animal studies through extrapolation of in-vitro data to in-vivo biodistribution. Results are obtained in minutes through optimization of software architecture on desktop hardware. Current evaluation of nanomaterial safety involves time consuming data collection and piecing together available exposure and toxicity information, and it this must be completed one material at a time. For many chemicals in consumer products these issues have been successfully addressed with software tools, but such efficient tools are still lacking for nanomaterials' hazard evaluation. This in vitro to in vivo extrapolation for potential in hazard assessment*(62)* delivers true effective doses at sites of interest which benefits for those interested in development of therapeutics, regulation, and protection of human health in the consumer space.

CHAPTER II. IN-VITRO CELL UPTAKE ANALYSIS AND VALIDATION OF FLUORESCENT ASSAY

In vitro systems are considered viable “bottom-up” approaches for identification, characterization, and quantification of NM interactions for a variety of tissue cell types because of their ability to provide data in a more controlled environment. Thus, in vitro assays can be used as benchmarks for prediction of animal biodistribution and subsequent toxicity. In vitro simulation-based approaches exist to predict dose at target cell site for NMs (ISDD)*(57)*, but with limitation such as limitations to only spherical particles, do not predict degradation of the NM upon exposure to cellular environment*(63)*, and may not differentiate between internalized and membrane-bound particles*(64)*, given that particles are internalized via endocytotic/phagocytic pathways*(31-33)(34)* These issues must be addressed, as supported by a recent EPA review*(65)*, that states in vitro systems still require significant improvement for proper interpretation and translation of 1) dose and 2) response data. In some cases, doses are misinterpreted through false positives/negatives due to substantial NM-dye*(45)* or NM-biological degradative effects*(66)*. The result is data non-representative of the true dose, which can be disastrous for drug development*(67)*. Furthermore, particle size can change in biological serum as well as usage of improper solvent during uptake experiments will often yield faulty uptake and subsequent toxicity measurements. The EPA also discusses the importance of utilizing *mechanistic biology* in in vitro assays in order to elucidate, interpret, or translate to in vivo animal studies and questions current practices in relying solely on in vitro approaches*(65)*. For instance, the Faustman group recently supported this by determining benchmark dose (BMD) from exposure dose and is the true dosimetric dose*(68)*. To achieve in-vivo predictive capabilities for NMs, simulations must represent physical processes a NM undergoes with the animal vasculature and cells, while accounting for any significant cell-induced degradation that is often overlooked *(12, 63, 69, 70)*.

Here, cell-NM uptake was captured through the fluorescence signal emitted by the fluorescent CdSe/ZnS COOH (QSH or QD) and dye-loaded carboxy-functionalized polystyrene (PS) due to their known degradation and stability in-vitro, respectively *(71)*. Hepa1-6 was chosen as the model cell line to demonstrate development of this fluorescent approach due to the aggressiveness of murine liver hepatoma *(13)*. We allowed cells to reach 90% confluence and establish membrane integrity*(72)* after 48 hours. Comprehensive analysis on toxicity **(Appendix A1)** and stability **(Appendix A2)** reveal minimal toxicity and sedimentation for a 10nM dose of the NMs chosen for this study, indicating minimal cell detachment and constant exposure dose. All data are within the linear dynamic range, as well as within the limits of detection and quantitation (**Appendix A3, Appendix B1**).

The RCF assay is built starting from the (schematic in **Fig. 1)** application of cells on a 96-well plate in 3 "compartments": the Cell System Interactions (CSI) compartment (*cells + NM (unwashed), accounts for cell-induced NM degradation*), the Cell Kinetic Data (CKD) compartment (*cells + NM (washed), measurement of NM uptake*), and the Cell Control (CC) compartment (*cells in media + no NM (unwashed), control with untreated cells to subtract background signal*). The Media and Protein Effect (MPE) compartment (*no cells + NM in media (unwashed)*) accounts for media and protein induced degradative effects on the NM in the absence of exposure to cells. Note that the CSI and MPE compartments are never washed and therefore maintain the initial applied dose of NM (10 nM in this demonstration of the method). The CKD compartment is washed at each time, *t,* to remove NMs that are not cell membrane bound or internalized by cells. Control experiments on blank wells showed minimal NM adhesion to the sides and surface of wells, indicating all fluorescence should strictly come from NM interacting with cells. For RCF assay development and validation to AAS for QSH, we used 18 wells per

compartment, which resulted in one 96-well plate per time point. In applications of the method, such a large statistical group is not required. Therefore, wells will be freed up to allow for multiple time points and cell types on the same plate.

At time zero, the CSI, CKD, and MPE compartments were dosed with 10nM QSH or PS (10% FBS DMEM suspension), with one NM type per plate. Comparing (by t-test) the fluorescence signal for wells in the CSI compartment at time *t* with the fluorescence signal from wells in the MPE compartment at time *t* gives insight into cell-induced degradation (see **Fig. 1** RCF decision tree). If they are statistically different we conclude cell induced NM degradation is present and the quantity of fluorescence signal loss due to this effect is determined from the difference of CSI and MPE at time *t* (see **Fig. 2a-c**).

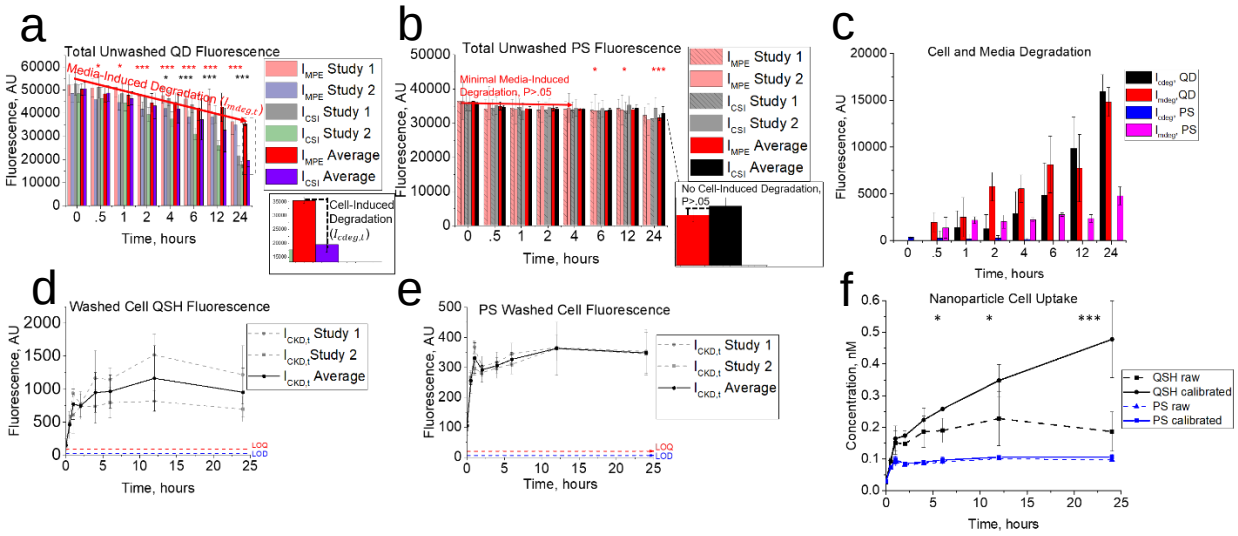

Figure 2. Fluorescence data from cell kinetic studies for 0, .5, 1, 2, 4, 6, 12, and 24 hours. Total fluorescence for wells with (CSI) and without (MPE) cells exposed to 10nM for **(a)** QSH and **(b)** PS. Fluorescent intensities $I_{CSI,t}$ and $I_{MPE,t}$ for **(a)** differ significantly (P<0.05) for QSH at approximately 4 hours, indicating cell-induced cellular induced degradative effects. Fluorescent intensities $I_{MPE,t}$ and $I_{MPE,0}$ differ significantly from 30 minutes, indicating media degradation at this time. For PS (**b**), no significant cell induced degradation is present (P>0.05). Media induced degradation begins at 6 hours (P<0.05). Differences between $I_{CSI,t}$ and $I_{MPE,t}$ and $I_{MPE,t}$ with $I_{MPE,0}$ were plotted in (**b**), showing a steady increase for QSH and constant intensity for PS. Media (I_{mdeg}) and cell (I_{cdeg}) induced degradative values were calculated from **(a, b)** and plotted against time in **(c)**. Fluorescent intensities were taken after washing 2X with complete growth medium and further trypsinization for **(d)** QSH and **(e)** PS. Cell fluorescence values from CKD **(d, e)** were ratiometrically used to determine concentration (nM) of QSH and PS NM uptake/adsorption in **(f).** The ratiometric calibrated concentration of QSH (black, solid) shows significantly higher values (P<0.05) than raw values (black, dashed). However, PS does not degrade, so calibrated (blue, solid) and raw (blue, dashed) concentrations are not significantly different. Statistical t-test p-values are described as follows: ***P<0.001, **P<.01, and *P<0.05.

Similarly, comparing the fluorescence signal (by t-test) from wells in the MPE compartment at time *t* with respect to MPE at time zero gives a description of media-induced degradation. These critical steps guide NM uptake calculations, especially if degradation is present.

Fluorescence data on NM-cell total uptake (adsorbed + internalized) were obtained from the CKD compartment after washing 2X, trypsinizing, and mixing (**Fig. 2d,e**), with minimal trypsin

interference on signal found (**Appendix A4**).The CKD fluorescence signal at time *t* ($I_{CKD,t}$) is representative of adsorbed and internalized NM. Comparison of signal obtained from CKD to CSI at time *t* ($I_{CSI,t}$) for a given concentration of NM applied (nM, [Dose]) will yield the ratiometric calibrated concentration of NM taken up by cells ($[Uptake]_{c,t}$) as follows,

$$[Uptake]_{c,t} = \frac{I_{CKD_t}}{I_{CSI_t}} * [Dose] \quad (1)$$

Here, NM located within CKD and CSI compartments have both undergone media and cell-induced degradation. This ratiometric approach thus implicitly accounts for NM degradation without further data processing and requires no external calibration curve. For comparison, raw concentrations were obtained from the intensity of the CKD compartment at time *t* relative to the CSI compartment at time 0 (replace $I_{CSI,t}$ with $I_{CSI,0}$ in equation 1) to understand the degradative effect cells and media can have on a NM. **Figure 2f** shows results obtained from usage of equation (1) for ratiometric calibrated and raw data calculations.

To ensure repeatability, the RCF assay was completed approximately 2 months apart with a new batch of thawed cells for both NM types (n=2), with reproducible results (**Fig. 2, Appendix A5,A6)**.

Comparing Results from Assay for QSH and PS

A key consideration to make was that data from the CSI compartment in **Figure 2a** indicate media induced degradation from 30 minutes and cell induced degradation from 4 hours for QSH, while **Figure 2b** shows no cell induced degradation and minimal media induced degradation occurring after 6 hours for PS. This was further tested by prolonged intracellular exposure studies, which resulted in a continued decrease in fluorescence signal (degradation) observed for QSH QD and full stability for PS (**Appendix A7**). These results indicate that the collected fluorescence signal

can be sensitive to the intracellular and media environment depending on the NM studied. All averaged cell- and media-induced degradation values ($I_{cdeg,t}$ and $I_{mdeg,t}$, respectively) are quantified in **Figure 2c**. Evidence of cell-induced degradation is given by lysosomal colocalization studies, observation of substantial Cd^{2+} core leakage (**Appendix A8**) under simulated lysosomal conditions (**Figure 3d, top and bottom inset, respectively**),*(73),(74)* and fluorescence data under cell exposure (**Appendix A9**) and lysosomal conditions (**Appendix A10**). However, our in-vitro studies with cells also showed minimal export of free Cd^{2+} from cells to the supernatant (**Appendix A11**). We also noticed minimal Cd^{2+} induced toxicity in cell culture (**Appendix A12**). Raw fluorescence data for QSH and PS collected from the CKD compartment (**Fig. 2d,e**) show an overall increase of raw fluorescence signal over time for both NMs, but with different profiles. The raw QD profile rises to a maximum at approximately 12 hours, while the raw PS profile rises and saturates within 1 hour. Note that these raw fluorescence signals represent data that include degradation effects in the case of QSH.

Application of equation 1 ensures that degradation effects are accounted for during calculation of NM concentrations (refer to methods for proof) since we compare $I_{CKD,t}$ with $I_{CSI,t}$ at their respective time points. By doing so, we internally calibrate the raw fluorescence signal collected from the (washed) CKD compartment to the (unwashed) CSI compartment (internal standard), knowing that both compartments degrade under the same conditions, and we obtain ratiometric calibrated NM concentrations that are independent of NM degradation. Ratiometric calibrated QSH concentrations (**Fig. 2f**) show a completely different profile from QD concentrations calculated based on the corresponding raw fluorescence data (for calculation, see online). A non-saturable uptake is found for the ratiometric calibrated QSH concentration as a function of time with C_{max} occurring at 24 hours (0.478 ± 0.122 nM), and significant deviation between calibrated and raw profiles is observed for QSH starting from approximately 4 hours, which is when cell-induced

degradation begins (**Fig. 2a**). Raw fluorescence-based QSH concentrations (**Fig. 2f**) indicate saturable cell uptake, with maximum concentration (C_{max}) occurring at approximately 12 hours (0.228 ± 0.0852 nM). In comparison, the calibrated and raw PS uptake profiles are not statistically different (P > 0.05), and reach saturability within 1 hour of exposure (**Fig. 2f** blue, solid and dashed). Overall, we find a fraction of up to 4.78±1.22% QSH and 1.07±0.085% PS was adsorbed to/internalized by cells after 24 hours with respect to the initial applied dose.

Atomic Absorption Spectroscopy Analysis and Validation of Assay

AAS was run to validate the RCF assay using absolute cadmium content with respect to QSH for the two studies (n=2) discussed above. Samples were collected from all compartments in the RCF assay at each time *t*, degraded in 33% v/v aqua regia (AR), and measured for absolute cadmium content. Note that AR treatment leads to a dilution of [Dose] from 10nM to 6.66 nM that is accounted for in calculations (see methods). AAS measurements were referenced to a 6-point cadmium calibration curve (**Appendix A13**) constructed with equal %v/v AR. As expected, AAS data obtained from the CSI and MPE compartments show that the cadmium concentration in both scenarios remained equal (P>0.05) at constant concentrations of approximately 3.60±0.0602 mg/L and 3.54±0.0841 (**Fig. 3a**), respectively, since no cadmium is removed from the system for these samples (unwashed).

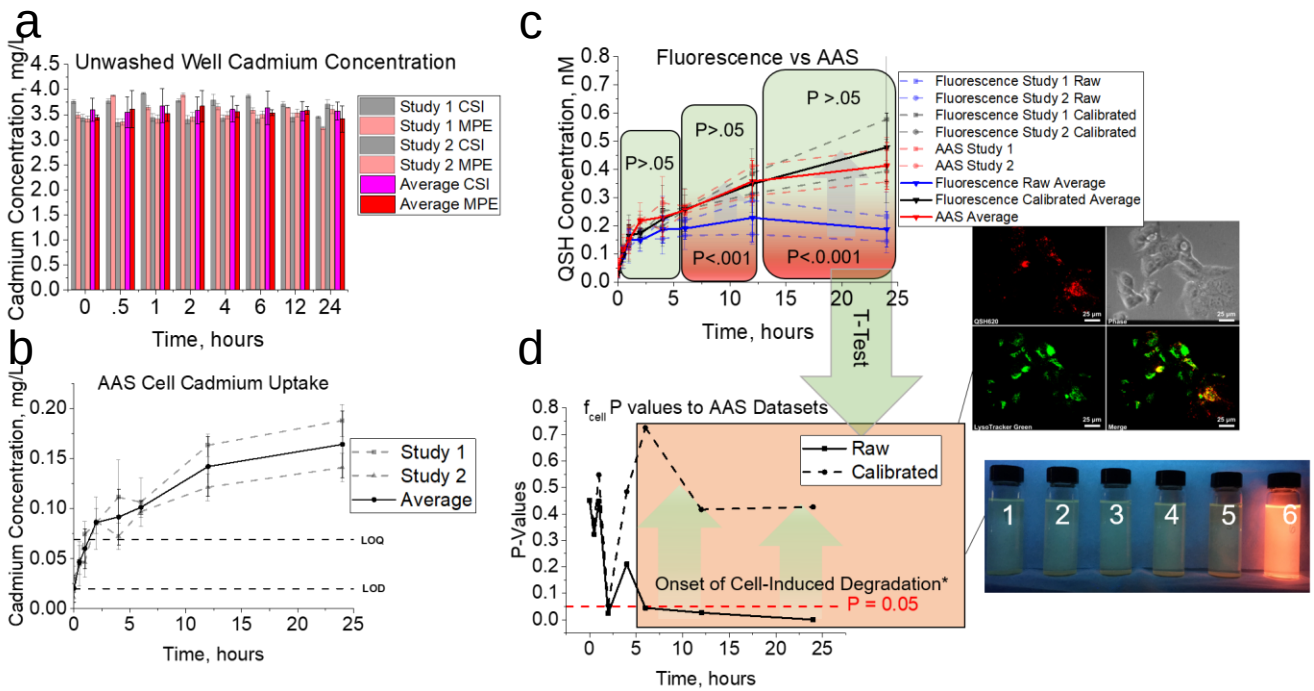

Figure 3. AAS analysis and validation to RCF method. MPE and CSI compartments **(a)** contain 3.60±0.0403 mg/L and 3.54±0.0839 mg/L cadmium concentration, respectively. Data for CKD in **(b)** show gradual increase in cadmium concentration. Nanomolar quantities of QSH calculated from AAS and compared to fluorescence are shown in **(c)**, with ratiometric calibrated fluorescence results closely matching AAS average outputs. AAS average outputs were determined using a serial dilution of QSH with reference to a 6-point Cd calibration curve. **(d)** A two-tailed t-test p-value analysis between QSH concentrations adsorbed/internalized as determined by AAS, and ratiometric calibrated (dotted line) or raw (solid line) data from in-vitro assay accounting for or not accounting for cell-induced degradation, respectively, was performed. Nanomolar quantities shows increase in p-value when correcting for cell-induced degradation (calibrated). Asterisk after cell-induced degradation implies onset of significant increase in p-value when accounting for cell induced degradation. Top inset shows lysosomal colocalization studies performed for QSH after cell exposure, with significant lysosomal sequestration. Bottom inset gives visual evidence of fluorescence loss upon exposure to lysosomal conditions. After 24 hours, a snapshot was taken to illustrate the diminished fluorescence due to citric acid exposure. Solutions 1-6 with equal concentrations of 10nM QSH with varying pHs (2.5-7.4, left to right) of 25mM stock citric acid buffer solution was made in complete growth medium (DMEM supplemented with 10%FBS). Solution 1, pH 2.5; Solution 2, pH 3.0; Solution 3, pH 3.5; Solution 4, pH 4.0; Solution 5, pH 4.5; Solution 6 pH 7.4, no citric acid.

Parallel studies using a sample of QSH stock diluted to 6.66nM showed no significant difference ($P>0.05$, **Appendix A14**), indicating quantitative collection of Cd^{2+} from the 96-well plates (RCF assay). Extraction and harvest efficiencies for each time point were also determined to understand if the full dose of cadmium was extracted from the cells and harvested from the wells, with all results showing full extraction and harvest efficiency (**Appendix A15, A16**).

AAS data obtained from the CKD compartments (**Fig. 3b**) show a gradual increase in total Cd^{2+} content, up to an average of 0.164 ± 0.0332mg/L, which corresponds to $4.56 \pm 0.925\%$ of the applied dose. All experimental data lay significantly above both the limits of detection and quantitation (LOD and LOQ, respectively) with Pearson's coefficient of 0.999 (**Appendix B2**). Using these data, cadmium concentrations from AAS were converted to nM concentrations of QSH through a linear correlation of the slopes of the QSH and $Cd(NO_3)_2$ AAS calibration curves (**methods** and **Appendix A17**). We also performed a standard additions method and 6-point calibration method in parallel for the 24 hour time point (**Appendix A18**). Results did not differ significantly ($P>0.05$, **Appendix A18**), indicative of minimal cell matrix interference on AAS data.

All data in **Figure 3c** indicate similar QSH uptake up to 4 hours ($P > 0.05$, **Fig. 3d**) suggesting no significant degradation occurs. After 4 hours, as CSI and MPE intensities in **Figure 2a** indicate, cell-induced degradation takes effect, and raw QSH concentrations obtained from the in-vitro assay begin to saturate and deviate from AAS as well as from the RCF-based QSH concentrations (**Fig. 3c,d)**. AAS and RCF-based QSH concentration uptake profiles are equivalent for all time points and do not differ with statistical significance. Profiles for the ratiometric calibrated fluorescent concentrations match AAS, thus validating the fluorescence portion of the research herein.

Cell simulation gives insight on subcellular localization and degradative rate.

A kinetics-based in-vitro model was built to extract rate constants for adsorption, desorption, internalization and degradation of both NMs from the RCF assay. This cell kinetic model was guided by a variety of biological processes for NM internalization including NM adhesion, desorption, internalization, and degradation through fist-order rate constants k_{ads}, k_{des}, k_{int}, and k_{deg}. The model consists of compartments representative of 1) media 2) cell membrane and 3) cell space. The cell kinetic model assumes a simple 3 compartment model, enough to provide sufficient understanding of whether a NM has made it inside the cell, remained outside, and how much it degraded.

Media Compartment. This compartment includes the media environment from which cells receive their respective NM dose. The initial dose condition was taken as the 10nM applied in the RCF assay. The media compartment NM dose evolution with time is then described as:

$$\frac{d[Med]}{dt} = -k_{ads} * [Med] + k_{des} * [Mem] \quad (2)$$

where [Med] is concentration (nM) of NM in media, [Mem] is the concentration (nM) of NM adhered to cell membrane, and k_{ads}, k_{des} are the first-order rate constants for adsorption and desorption to and from the cell membrane, respectively.

Cell Membrane Compartment. The cell membrane compartment includes the outer portion of the cell with which the NM interacts. This compartment separates the media from the internal space of the cell. NMs that are internalized by the cell must first adsorb to this compartment through the adsorption rate constant, k_{ads}. Once adsorbed, NMs can 1) leave this compartment through desorption, k_{des} or 2) enter the cell via k_{int} as expressed by:

$$\frac{d[Mem]}{dt} = k_{ads} * [Med] - k_{des} * [Mem] - k_{int} * [Mem] \quad (3)$$

with parameters described above.

Cell Space Compartment. The cell space compartment receives NMs that have transported inside the cell via the first order rate constant for internalization (k_{int}). Here, NMs can become degraded if the process occurs (determined through RCF assay). The cell space compartment NM dose evolution as a function of time is then described as:

$$\frac{d[Cell]}{dt} = k_{int} * [Mem] - k_{deg} * [Cell] \quad (4)$$

where [Cell] is the concentration (nM) of QSH in cell interior at time t and k_{deg} is the first order rate constant for degradation of QSH obtained from optimization to raw datasets (see below).

All above equations were fit to RCF data (QSH ratiometric calibrated, PS, i.e. degradation effects removed) through optimization of parameters k_{ads}, $k_{des,}$ and k_{int}. Here, the genetic algorithm (GA), originally developed by Holland in the early 1970s*(58)* was used as an artificial intelligence algorithm for a robust optimization of parameters based on evolutionary ideas of natural selection. For optimization, initial vectors ("chromosomes") comprised of rate constants ("genes") were randomly populated by the GA, fed to the cell kinetic model, calculated for fitness, underwent selection, crossover, and mutations to maximize diversity and produce better fitness at each iteration ("generation"). At model convergence (20-50 generations, **Appendix A19**), the optimized parameters provided reasonable correlation coefficients (R = 0.994 and 0.938 at P < 0.001), coefficients of determination (R^2 = .989 and .880), standard errors (S = 0.0152 and 0.0158nM), and residuals for QSH and PS respectively (**Appendix B3** and **Appendix A20**). Next, we reconsidered QSH raw concentration values containing degradation effects to determine the rate of degradation (k_{deg}), holding the previously optimized adsorption, desorption, and internalization rates (k_{ads}, $k_{des,}$ and k_{int}) as constant. At model convergence (**Appendix A21**), visuals of model outputs show reasonable fit to measured RCF data for QSH and to raw QSH assay data with degradation (ratiometric calibrated and raw datasets, respectively in **Fig. 4a)**.

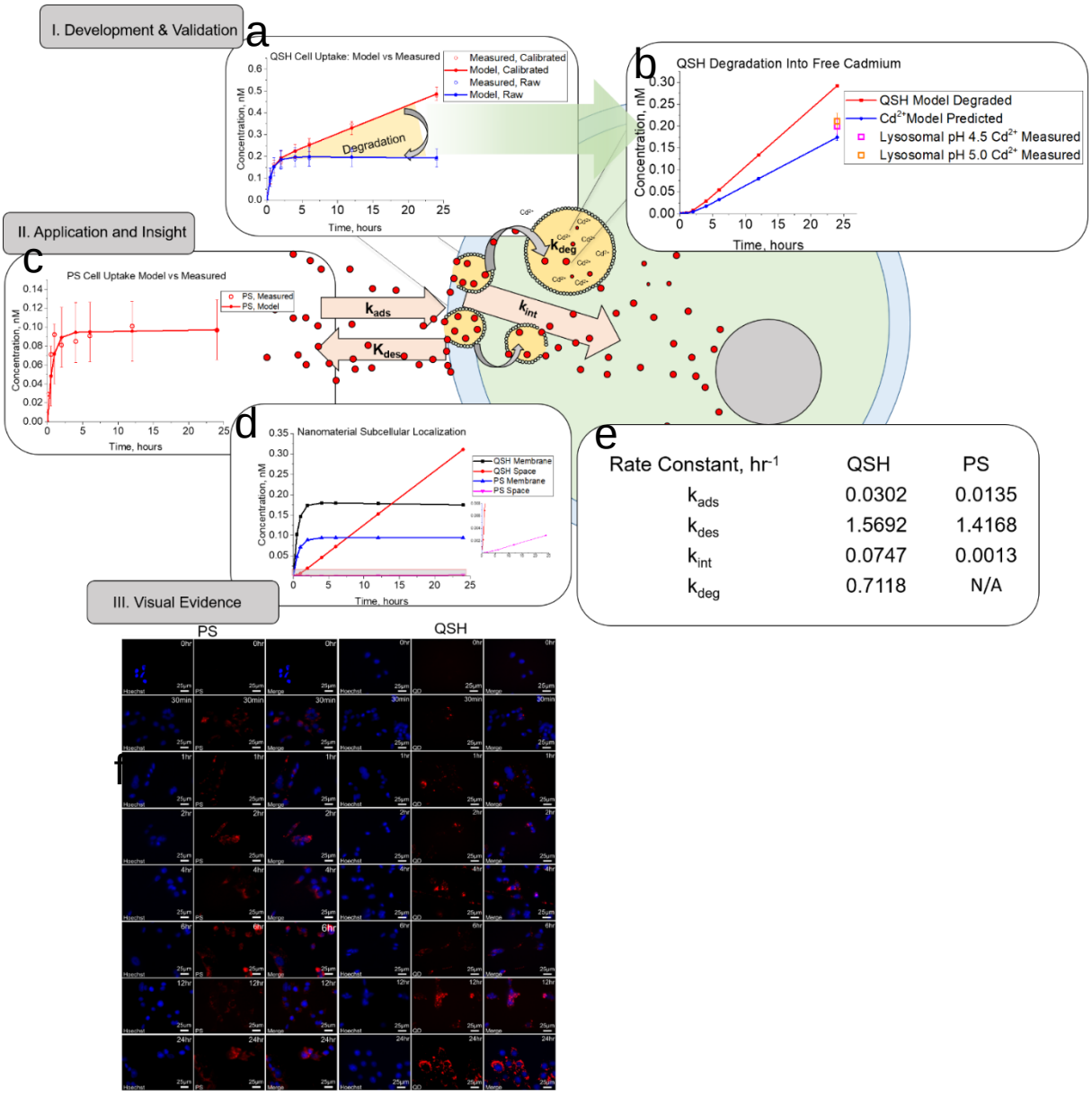

Figure 4. Outputs of cell simulation quantify rates of adsorption (k_{ads}), desorption (k_{des}), internalization (k_{int}) and degradation (k_{deg}) of NMs. (**a**) QSH model fits (line) to data (open circle) for cell samples taken from CKD for raw (blue) and calibrated (red) RCF datasets. Error bars indicate 95% confidence for model fit to data. (**b**) Model output prediction for amount of QSH degraded (red) and subsequent free cadmium formation (blue) predicted by model. Experiments with simulated lysosomal buffer give comparable free cadmium release from degrading QSH (purple and orange squares). (**c**) Application of RCF assay and cell simulation to stable PS nanoparticles shows early saturation compared to QSH QDs. (**d**) Cell simulation provides data on subcellular localization of NMs from RCF datasets, showing membrane and internalized quantities. (**e**) Table summarizing kinetic rate constants obtained from FORECAST.

Rate constants include adsorption (k_{ads}), desorption (k_{des}), internalization (k_{int}), and degradation (k_{deg}) for QSH QDs and PS NMs. (**f**) Confocal imaging of Hepa1-6 cells dosed with 10nM QSH and PS. Cells were collected from RCF assays. PS and QSH (red) images are shown above. Hoechst33258 (blue) is the nuclear stain. QSH shows no saturability for all time points from 0 to 24 hours. PS shows saturable uptake around 2 hours.

Interestingly, with the optimized rate of degradation k_{deg}, the model predicted the concentration of QSH degraded (nM), and when converted to Cd^{2+}, predicted absolute cadmium content that fits very closely to measured Cd^{2+} release from QSH under lysosomal conditions (**Fig. 4b**). This further illustrates our model's predictive power to quantify NM degradation when used in conjunction with the RCF assay. For the PS NM, **Figure 4c** shows the model fit to measured data. Subcellular level analysis (**Fig. 4d**) shows remarkable differences for both NM types. QSH membrane quantities were initially higher, until 12 hours, where internalized quantities dominated the total cell space. PS maintained high membrane binding with minimal internalization for all time points. Rate constants (**Fig. 4e**) indicate that membrane binding is the rate limiting step for QSH, while internalization is the rate limiting step for PS. Confocal microscopy (**Fig. 4f**) qualitatively supports these findings, with saturable uptake for PS within 2 hours and limited saturability for QSH with higher internalization.

Overall, NMs can be prone to degradative processes within the cellular environment, which can cause fluctuations in fluorescent signal and result in inaccurate representation of tissue level delivered dose. This issue has prevented fluorescence from being a useful tool for extracting rate kinetics. Here, we showed that cellular degradative effects are present and accounted for in our in-vitro assay and corresponding cell kinetics simulation. We ran QSH (unstable under biological conditions) and PS (polystyrene, stable control) NMs against an aggressive murine liver Hepa1-6 cell line,*(13)* and found that the NM prone to degradation (QDs like QSH) exhibited substantial

deviations in fluorescence, while PS fluorescence remained constant. Our findings in **Figure 4** showed that degradative factors must be accounted for when aiming to extract rate kinetics for translation towards animal studies from in-vitro fluorescence data. However, questions do arise when understanding how physicochemistry affects total uptake quantities and must be addressed.

CHAPTER III. APPLICATION OF RCF ASSAY TO LIBRARY OF COMPOUNDS AND ANALYSIS

NM physicochemistry strongly affects the uptake and toxic response of cells. There is a need to understand and develop correlations between physicochemistry and uptake, as the dose will inherently affect the response*(75)* in live animals. This structure-activity relationship is important for understanding and developing important assumptions for predicting NM uptake from in-vitro data. Research is still in relatively new, as most of the correlative analysis has only been performed for metal (iron)-oxide nanoparticles*(76)*. A few recent studies have included libraries of at least 109 differently surface-modified iron-oxide nanoparticles and their subsequent structural surface ligand correlations with cell uptake*(77, 78)*, but the influence of the core composition of a NM cannot be ignored, as evidence shows it is a huge influential factor in cell interactions*(79)*. However, the most sensitive descriptors of physicochemistry found in literature so far are lipophilicity*(76)*, size*(78)* , and charge*(79)*. Taking this into account, we rapidly screened a variety of hydrophilic (water soluble) NMs to understand the influence of size and charge on total NM uptake. Addressing these factors ensures that target cell dose is accurate so that proper dose-response modeling lead to correct dose*(68)* determination.

To understand how size and charge can influence uptake of NMs and potentially track these correlations, the RCF assay was used to analyze uptake of NMs with various diameters and charges. Specifically, PS, ZnSe (ZQD), and CdSe (CQD) were used as model systems to quantify and understand results from changes in physicochemical parameters. PS consisted of NMs with diameters of 50, 100, and 500nm. 50nm PS particles were also analyzed as positively charge (amine functionalized, APS), negatively charged (carboxy-functionalized, CPS), and naked (hydroxyl-functionalized, NPS). ZQDs and CQDs both consisted of single

diameters of 10 and 30nm, respectively. 10nm ZQDs consisted of a positive, negative, and neutral charge and 30nm CQDs consisted of solely carboxy-functionalized motifs on the surface.

Size of particles is an influential factor within a range.

Overall, CPS with sizes of 50, 100, and 500nm exhibited first order kinetics, with their fraction of dose uptake at approximately 0.02-0.06 or 2-6% of dose taken up (**Fig. 5**). This implies that particles within the range of 50 to approximately 500nm in diameter most likely are taken up by a similar uptake process, primarily clathrin or caveolin mediated endocytosis. This is critical, as the first order kinetic assumption implies that the total uptake of NMs is dependent on dose, ie. as dose increases the total uptake increases, but the fraction of uptake remains relatively the same. Furthermore, first order rate constants would be an accurate description of this process for the next chapter.

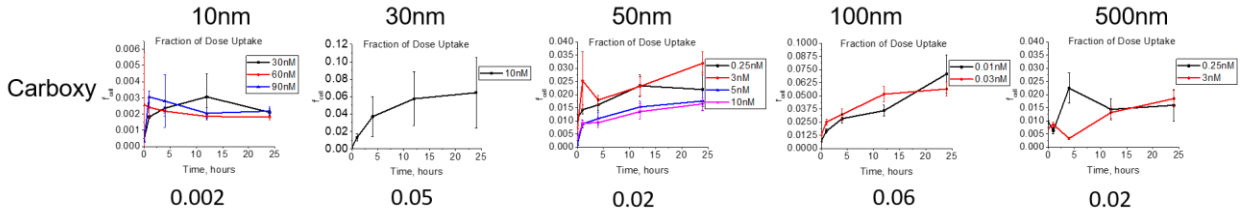

Figure 5. Carboxy-functionalized total NP uptake for liver cell line with NP of varying size.

Once particles reach over 500nm in diameter, we believe internalization will proceed via a different uptake process, primarily macropinocytosis. Thus, particles below 500nm in diameter, we expect to follow first order kinetics and rate of uptake would be properly described by first order rate kinetics. Carboxy-functionalized ZQDs of 10nm diameter exhibited very minimal uptake, with cells only taking up approximately 0.002 or 0.2% of the applied dose (**Fig. 5**).

However, when the size increased to 30nm, carboxy-coated CQDs internalized approximately 0.06 or 6% of the dose. Again, this jump in uptake of relative fraction of applied dose is described by differences in uptake processes. Smaller particles are expected to enter the cellular environment primarily through pinocytosis (cell drinking) or passive diffusion, which is a less aggressive form of uptake. As the particle size increases (~30nm), the uptake process of endocytosis (clathrin or caveolin-mediated) is predominant. Thus, particles of <=10nm in diameter must be analyzed carefully when extrapolating in-vitro uptake results to live animal in-vivo uptake in cells. Although these particles all contained carboxy-functionalization, it is important to note that the core structure of the material for 10 and 30nm particle types is both a different class (metal) and type Zn and Cd, respectively. These results indicate that particles within the 30 to 500nm range, with negative charge, will behave similarly when extrapolating total uptake to animal tissue cells. Particle types less than 30 or larger than 500nm must be looked at carefully, as other mechanism of uptake must be addressed, or these particles must have rate constants optimized to these particles specifically.

Charge of particles is the greatest influencer when analyzing total uptake of NM within cells.

Overall, positively charged particles exhibited a higher fraction of uptake than negatively charged particles for both ZQD and PS datasets (**Fig 6**).

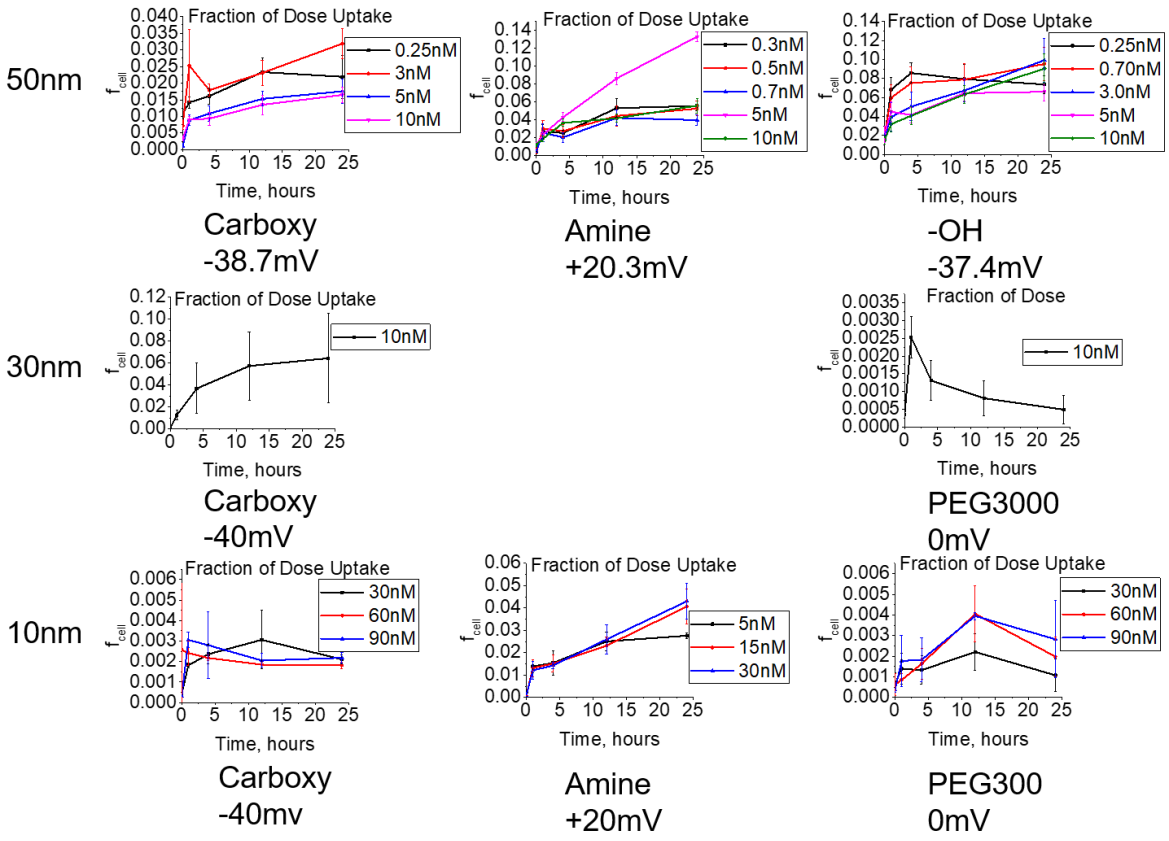

Figure 6. Total cell uptake of NPs of varying size and charge.

Interestingly, both 50nm and 10nm diameter positively charged APS and ZQD were taken up by cells at an average of 0.07 or 7% and 0.03 or 3% uptake, respectively. This indicates that although the particles are similar charge (positive), the optimal 50nm size does cause a significant increase in uptake to that of the smaller 10nm particle. This suggests that size and charge work together to influence total uptake. Comparing particles of like negative charge, 50nm CPS exhibited about a 10-fold higher uptake than their 10nm counterpart (0.03 or 3% versus 0.003 or 0.3%, respectively). Smaller positively charged particles only exhibited approximately 2-fold less uptake than the larger particles of similar charge, while smaller negatively charged particles exhibited over 10-fold less uptake than their larger counterpart.

This difference suggests that uptake of negative particles is heavily dependent on steric hindrance and electrostatic attraction to the cell membrane may cause a significantly greater influence and masks the difference in size of the particles. Neutrally charged 10nm ZQDs exhibited similar fraction of dose internalized to that of carboxy, indicating that when particles of equal or neutral charge rely more heavily on steric hindrance than the electrostatic effects.

Nanomaterials predominantly internalized exhibit more degradation.

Unwashed (CSI and MPE) datasets were analyzed for cell and media-induced degradation for all NM types (**Fig. 7a-j**).

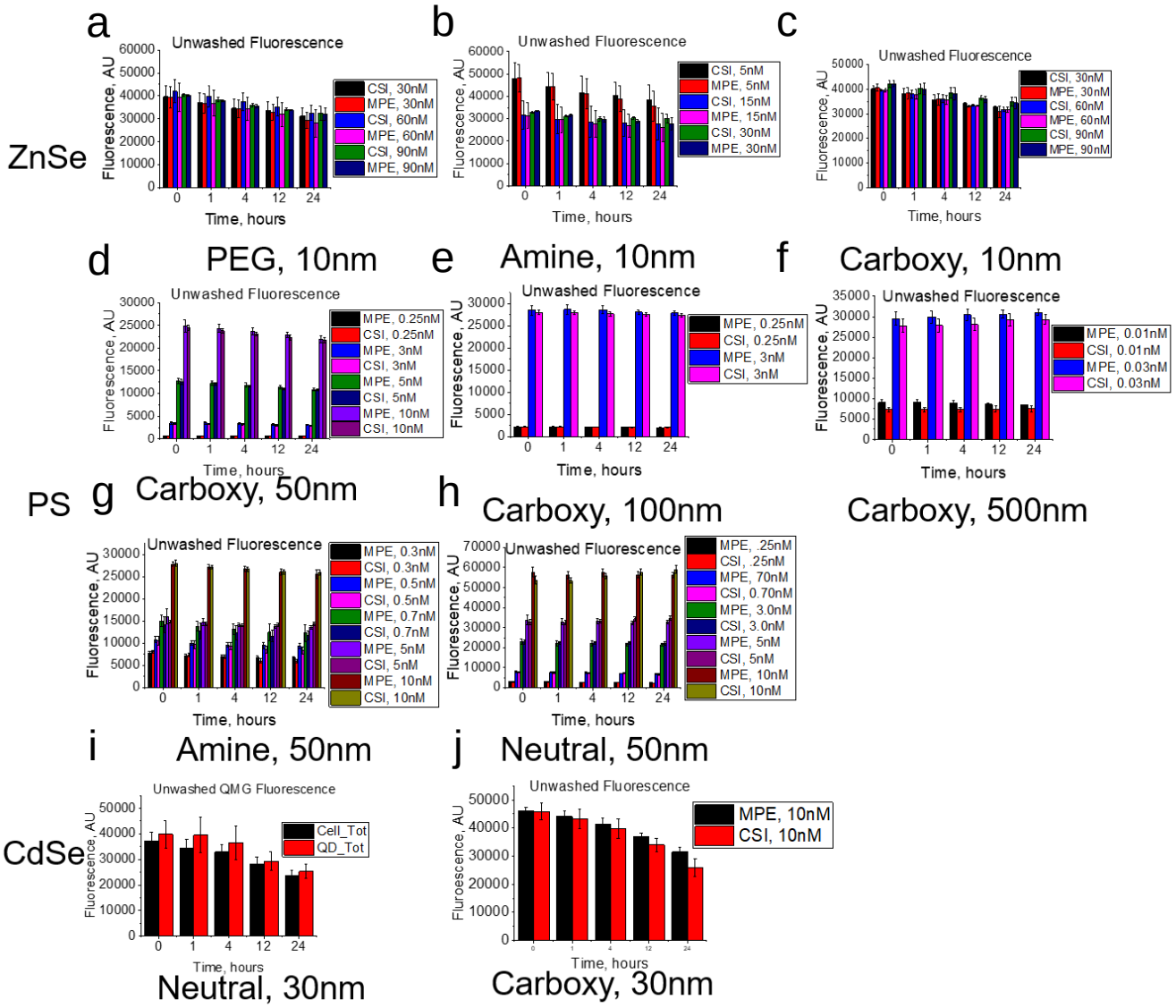

Figure 7. Total unwashed NP fluorescence after cell exposure. (a-c) show unwashed fluorescence for ZnSe QDs at different dosing scenarios (5-90nM). **(d-h)** give unwashed fluorescence intensities for PS of carboxy, amine, and neutrally coated types. **(i,j)** show unwashed fluorescence for CdSe 30nm QD of neutral (PEG2000) and Carboxy coating.

Overall, all PS particles exhibited no cell or media induced degradation for all types and concentrations (**Fig. 7d-h**, P>0.05). This is attributed to the intact structure of the polystyrene polymer and protection of the fluorescent dye in the core. CQDs had a differing profile for carboxy and neutral (PEG3000) functionalized NMs. As there was significant internalization (~8% of applied dose) for carboxy functionalized CQD after 24 hours, this NM exhibited both cell and media-induced degradation (**Fig. 7j**). Contrary to COOH functionalized CQD, PEG3000 neutrally functionalized CQD exhibited no cell-induced degradation primarily because of minimal internalization (**Fig. 7i**, ~0.2% of applied dose). This directly outlines the balance between internalization and cell-induced degradation; as internalization increases, we expect cell-induced degradation to increase for NMs that may be prone to degradative effects. ZQD did not exhibit any cell induced degradation for all NM types, but did exhibit media-induced degradation after 1 hour of exposure (**Fig. 7a-c**). This scenario outlines the direct effects of media-induced degradation for NMs that are not subject to cell-induced degradation.

Overall, these studies were critical in order to say that assumptions of first order kinetics were valid for NMs of similar charge and size. First, size can be an influential factor when understanding cell kinetics. For NMs <30nm in diameter, the uptake kinetics may be drastically different than those within the 30-500nm range. Likewise, for NMs larger than 500nm in diameter, optimization of rate kinetics may be essential for translation to animal studies. Finally, as dose studies suggested, regardless of applied dose, the majority of the NMs exhibited first order kinetics so we accept the first order description of the cell model. That is, similar fractions of dose were taken up, regardless of applied dose. Thus, they exhibited a very strong dose-dependent uptake values. This shows that future simulation studies are reasonable correct in assuming first order kinetics. However, we note that cells reach a maximum saturable uptake at approximately 24 hours and must be accounted for by inclusion of some boundary constraint for studies longer

than 24 hours. Cell and media-induced degradation can be influential factors, dependent on the material type being studied. Particles between 30-500nm in diameter can be assumed to behave according to similar rate kinetics as long as the charge is within reasonable range. Differences in charge (such as positive and negative) will drastically affect uptake kinetics, so extraction of rate kinetics for negatively charged particles will be used for negatively charged particle datasets in live animal validation.

CHAPTER IV. ANIMAL SIMULATION CONSTRUCTION AND FUNCTIONS

Simulation architecture, particle transport, and tissue content overview

The overall architecture of the animal simulation can be seen in **Figure 8,** where each tissue compartment contains 4 sub-compartments (epithelial, endothelial, interstitial, and macrophage).

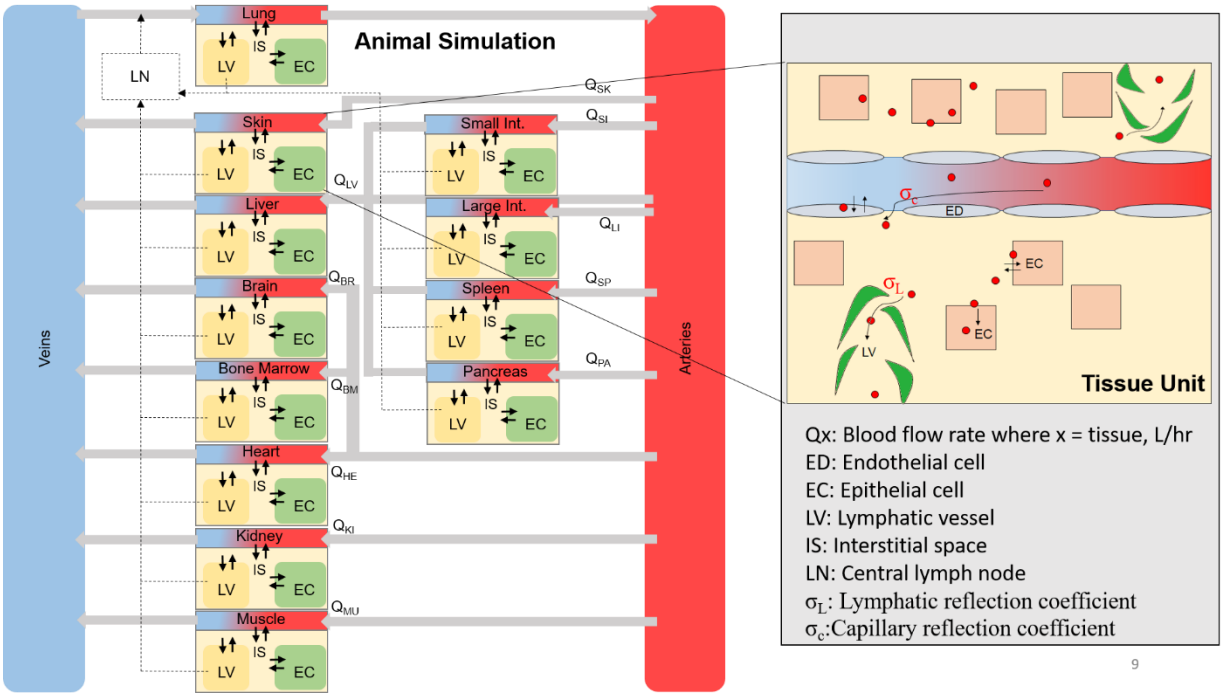

Figure 8. An overall schematic of the animal NM simulation. Scheme of the overall tissue and blood compartments that make up the full animal. Each tissue compartment is interconnected through blood flow rates and contains sub-compartments (zoomed in area) where a NM will distribute upon internalization through endothelial fenestrae.

Overall, we assume a NM to be 100% bioavailable, meaning it is injected immediately into the blood supply (arterial blood) of the pre-clinical species. Upon entering the blood supply, the NM is assumed to be delivered to each tissue type given its tissue specific blood flow rate (Q, **Fig. 8**). Each tissue for every pre-clinical species contains a total tissue volume and blood flow rate,

measured empirically and obtained from literature *(80)*. Tissue volumes and blood flow rates were kept as constants throughout the simulation. Tissue cell compositions (epithelial, endothelial, interstitial, and macrophage) and vascular fenestrations were obtained from literature, as stated below in this chapter. Maximum capacities of uptake from our in-vitro studies were extrapolated to whole tissues based on cellular content. All volumes, flow rates, and tissue cell compositions were taken relative to the species-specific tissue mass used in the study and extrapolated across species as necessary. Cell densities obtained from literature were assumed, for purposes of this study, to be similar across species (cells/g tissue). We understand that tissue cell compositions and densities may vary slightly across species, but for demonstration purposes of this pilot study, we assume densities to be consistent.

Particle transport from the blood supply to the tissue interstitia involves calculation of a new variable that captures reflection from pore walls, known as a reflection coefficient, explained below. In order for a NM to transport to the interstitia of a certain tissue, we assumed it travels through the fenestrations unique to the capillaries of that particular tissue (**Fig. 9**, inset), each with variable sizes found in literature, as explained further below. These fenestrations were represented by reflection coefficients (σ_v) computed herein to include the effects of particle drag and frictional hindrance*(81)* (**Fig. 9a**) akin to that of a sphere through an artificial porous membrane*(82)*.

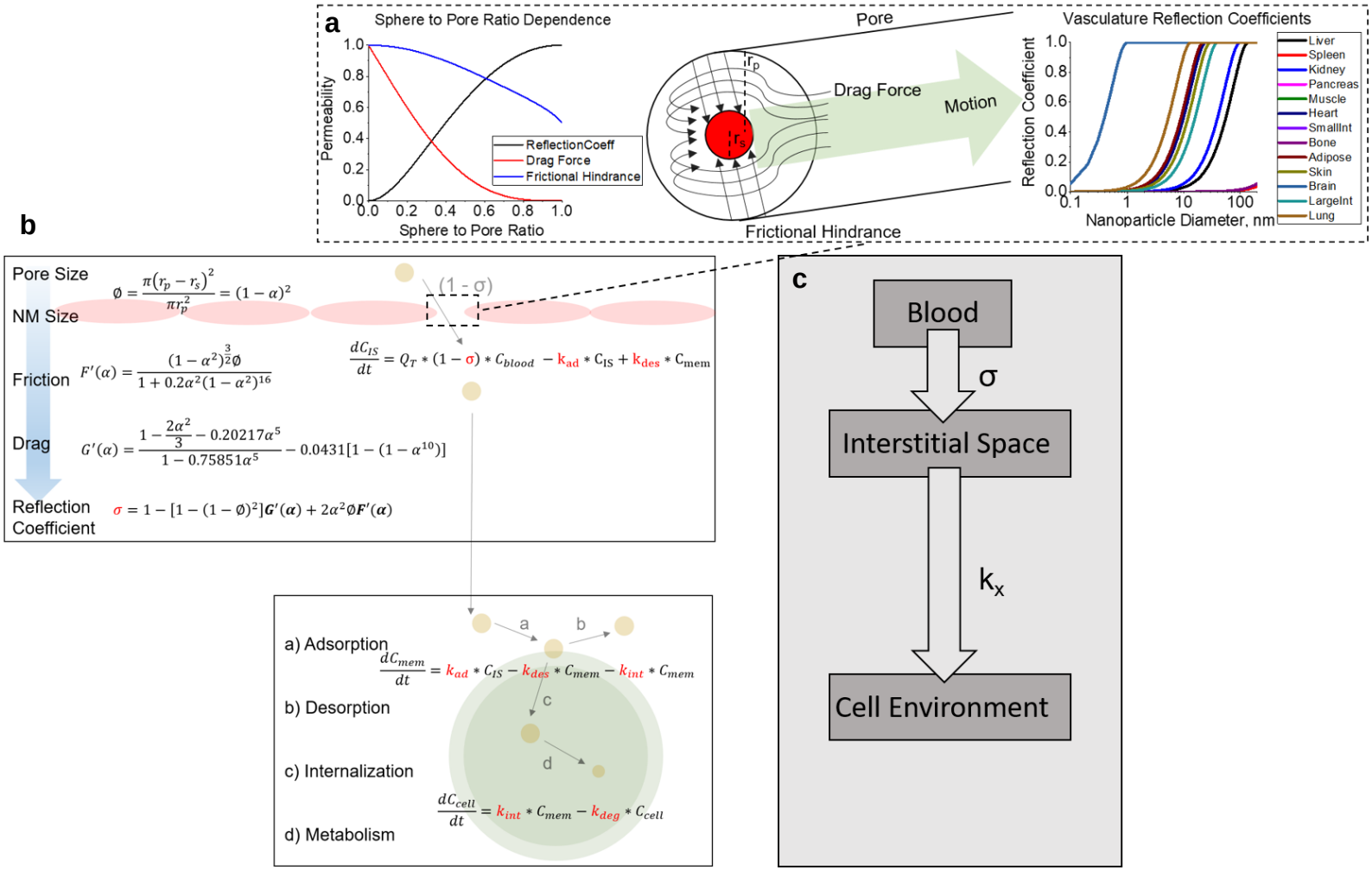

Figure 9. NM transport from blood supply to cell environment overview. a, Paracellular transport of NM through the endothelial fenestrae. Frictional hindrance and drag force are considered when calculating for the reflection coefficient, which is performed for each tissue type. **b,** Schematic of the NM transport process through the endothelial lining into the interstitial space from where it will interact with tissue cells through rate constants. **c,** Diagram of NM transport from blood to interstitia through the reflection coefficient and from interstitia to the cell environment through rate constants determined from RCF in-vitro where k_x represents the rate constant for a particular process for x = ad, des, int, or deg.

A NM located within tissues can accumulate inside the interstitia, vasculature, or within variable cell types. To account for accumulation within variable cell types in this complex architecture, in-vitro cellular kinetics (rate constants) were translated to our in-silico animal simulation and used as constants when quantifying averaged individual tissue cell interactions. To determine the quality of the rate constants and simulation resolution, we conducted two pilot studies in the next chapter, where we 1) assessed trends in whole-tissue uptake as a function of size and 2) quantified NM uptake at the single cell level. The calculated vascular reflection coefficient was then held as a constant in a series of ordinary differential equations representing mass transfer kinetics from the blood supply to interstitial space where the NM will react with tissue cells (**Fig. 9b,** rate constants in red) through first rate constants optimized to our in-vitro data. The overall transport processes involved in a tissue unit are captured in **Figure 9c**.

NM transport from blood to interstitia with fluid dynamic model

The transport of a nanoparticle from the blood supply to the tissue cells is simulated through fluid dynamic theory, primarily obtained from a hydrodynamic simulation of solutes through pores captured by modeling a reflection coefficient, σ, originally derived by Curry in 1974*(81)*. The published and validated fluid dynamic approach is folded in the animal simulation to provide predictive, mechanistic method of transport of any NM from the blood supply through pores located within an impenetrable membrane to the tissues. Any nanoparticle with a particular size can be predicted to enter all tissues of the body based on transport through capillary pores of these tissues. In theory, a nanoparticle must travel through a pore to enter the interstitial space of a particular tissue. Upon encountering a pore, a nanoparticle cannot occupy positions smaller than 1 NM radius from the pore's edge in blood vessel fenestrae. Thus, NM entry

through pores become sterically restricted as the NM approaches the size of the pore*(83)*. This effect is described by the solute partition coefficient (∅) below:

$$\emptyset = \frac{\pi(r_p - r_s)^2}{\pi r_p^2} \quad (5)$$

where r_p is the radius of the pore, r_s is the radius of the sphere or NM. These variables are reduced to obtain the relation

$$\emptyset = (1 - \alpha)^2 \quad (6)$$

where

$$\alpha = \frac{r_s}{r_p} \quad (7)$$

Thus, α is the ratio of solute radius to pore radius. The partition coefficient above is the ratio of the area available to the solute to the total pore surface area, accounting for the steric hindrance the particle has upon entering the pores of the fenestrae in blood vessels. However, the particle experiences a frictional hindrance from the pore walls upon entering. The frictional hindrance factor F(α) is a factor that defines this phenomena, capturing reduction in diffusion due to hindrance that the wall exerts on the particle through the viscosity of the fluid and is captured through equation below:

$$F'(\alpha) = \frac{(1-\alpha^2)^{\frac{3}{2}}\emptyset}{1+0.2\alpha^2(1-\alpha^2)^{16}} \quad (8)$$

Additionally, the difference between the solute velocity and water velocity (drag force) is captured through the hydrodynamic function G(α) according to equation below.

$$G'(\alpha) = \frac{1-\frac{2\alpha^2}{3}-0.20217\alpha^5}{1-0.75851\alpha^5} - 0.0431[1-(1-\alpha^{10})] \quad (9)$$

The reflection coefficient accounts for the hydrodynamics of convection and diffusion of hard spheres within a right cylindrical pore. The reflection coefficient is independent of the number of channels. When the reflection coefficient approaches 0, the nanoparticle enters the pathways in the membrane. When it is approaching 1, the pore excludes the nanoparticle and it remains outside the pores. The equation for the reflection coefficient accounts for both the frictional force and drag, equation below:

$$\sigma = 1 - [1 - (1 - \emptyset)^2]G'(\alpha) + 2\alpha^2\emptyset F'(\alpha) \quad (10)$$

The above equation for the reflection coefficient builds on previous studies including Bungay and Brenner, Lightfoot et al., and of Lewellen where they accounted for full hydrodynamics including steric exclusion, hindrances to diffusion, drag, and pressure drop across the sphere, torque and rotation produced by viscous interactions with the wall. These studies all validated the assumptions to measured data for permeability across animal tissue. This formula assumes no interactions between solute particles.

First order mass transfer kinetics guides particle transport from vasculature and interstitia to cells

NM transport to cells of a particular tissue is captured through the whole-body NM PBPK simulation described herein. In order for a NM to reach target tissue cells, it must first bypass the endothelial cell lining primarily through paracellular transport. Intracellular transport within the endothelial cell population is also captured through rate constants obtained from in-vitro RCF rate kinetics. However, any NM localized within the endothelial cells is either 1) degraded or 2) sequestered within the cellular environment. Intercellular gaps between the cells in-vivo are represented by a reflection coefficient, σ_v. The reflection coefficient builds on previous studies by Bungay and Brenner, Lightfoot et al., and Lewellen where hydrodynamic transport is captured, which includes steric exclusion (ϕ), hindrances to diffusion, drag, and pressure drop

across the sphere (G'(α)), and frictional interactions with the wall (F'(α)) described above. Using this coefficient, we can describe the transport of the NM from the blood vasculature (C_v) to the interstitial space (C_{IS}) through equation

$$\frac{dC_v}{dt} = \frac{Q_t \cdot C_{LU_V}}{V_v} - \frac{(Q_t - Q_L) \cdot C_V}{V_V} - (1 - \sigma_V) \cdot \frac{Q_L \cdot C_V}{V_V} - k_{ad_{endo}} \cdot C_V + \frac{(k_{des_{endo}} \cdot A_{mem})}{V_V} \quad (11)$$

Where the tissue blood flow (Q_t) and lung NM concentration C_{LUV} serve as inputs to this compartment, given that the lung is the primary organ that oxygenates the blood supply for all the organs of the animal. The NM will interact with the endothelial cell membrane (A_{mem}) of that tissue's compartment via the adsorption (k_{adendo}) and desorption ($k_{desendo}$) rate constants determined from in-vitro data. The vasculature reflection coefficient (σ_V) serves as guidance for the NM to enter the interstitial space given by

$$\frac{dC_{IS}}{dt} = (1 - \sigma_V) \cdot \frac{Q_L \cdot C_V}{V_{IS}} - k_{ad} \cdot C_{IS} + k_{des} \cdot C_{mem} \quad (12)$$

Where the individual tissue cells (epithelial and macrophages) will interact with the NM through the pre-determined in-vitro rate constants k_{ad} and k_{des} for their cell membranes (C_{mem}). The flow rate into the interstitial space is set to the lymphatic flow rate and vasculature interstitial volumes (V_{IS}) guide the concentration for this compartment. Once the NM enters the tissue cell membrane compartment,

$$\frac{dC_{mem}}{dt} = k_{ad} \cdot C_{IS} - k_{int} \cdot C_{mem} - k_{des} \cdot C_{mem} \quad (13)$$

it will desorb via the desorption rate constant (k_{des}) or be internalized into the cell space via the internalization rate constant (k_{int}). Once inside the cell space, the NM can be thus degraded or sequestered within the cellular environment (C_{cell}).

$$\frac{dC_{cell}}{dt} = k_{int} \cdot C_{mem} - k_{deg} \cdot C_{cell} \quad (14)$$

All tissue compartments herein are described as a series of differential equations designed to solve for concentrations utilizing the MATLAB ODE solver.

Cellular content of the liver

The liver epithelial cellular composition (cellularity) was taken from Karin and Sternbeck*(84)* wherein they determined the number of hepatocytes per gram of liver for humans, dogs, rats, rabbits, and mice using protein content analysis. The liver macrophage content were understood as Kupffer cells, and obtained by Armbrust and Ramadori through rat liver immunofluorescent staining of antibodies EDI and ED2 and checked for phagocytosis*(85)*. Liver endothelial cell content were also obtained through staining and centrifugation analysis of immune-phenotyping*(86)*. All cell content from each study were scaled to either rat, mouse, or NHP through scaling of cells/g using volume and densities of liver from measured physiological data*(80)*. Fenestrated blood capillaries of the liver can reach diameters as wide as 280nm for rodents and 180nm for humans. Here, there is a minimal glycocalyx matrix and absence of basement membrane, so transport into the liver epithelial tissue is minimally hindered.*(87)*

Cellular content of the bone

Bone marrow epithelial content was obtained from Posel et al. wherein they obtained bone marrow from 12-week old male rats. Femurs and tibiae were harvested, purified, and analyzed for bone marrow mononuclear cells (BMNCs) using Ficoll-Paque density gradient centrifugation and subsequent flow cytometry. Epithelial cells here are considered B-cells, $CD45^{+}$, and polymorphonuclear (PMN) cells*(88)*. Macrophages are considered $CD14^{+}$, and $CD45^{+}$. Endothelial cells were taken from Nombela-Arrieta et al. 2017, wherein they used immunostaining of mouse bone marrow cells that exhibited $CD54^{-}$, $Ter119^{-}$, and $CD31^{+}$ phenotype frequency (%) an compared it to total harvested BMNCs*(89)*. Bone marrow

endothelial capillaries of can be sinusoidal, which is an open-pore capillary that is fairly discontinuous. This type of capillary can have a diameter of 30-40um.*(90)*

Cellular content of the lungs

Nine species of animal were studied, with different portions of the alveolar regions of each species analyzed. Cell nuclei were observed from each class of parenchymal lung cell, and densities were calculated using electron microscopy. Number of cells per lung were then obtained. Type I and II epithelial tissue cells were then obtained*(91)*. This was also applied for endothelial and macrophage content in the lung. Endothelial cells lining the luminal area of the alveolar regions of the lung are generally connected via tight junctions. Inter-endothelial junctions sometimes contain gap junctions, which have been captured through immune-gold or immunofluorescence labeling. About 27nm gaps appear between plasma membranes of endothelial cells have been observed*(92)* and used in this study.

Cellular content of the kidneys

Stereological analysis of total numbers of glomeruli and individual glomerular cell types in rats was performed for seven adult rats*(93)*. Kidneys were perfused and digested and total glomerular number was estimated using optical instrumentation and TEM to count cell types. Here, we obtained cell types per rat and mouse. We scaled total number of cells per glomerulus using the total number of glomeruli per kidney. Specifically, we scaled mesangial and epithelial podocytes as epithelial and endothelial separately. Macrophage composition was taken by Kirkman through rat kidney sectioning and microscopy analysis of multiple kidney cross sections, including the cortex, intermedia, and basalis*(94)*. Endothelial pores of the rat kidney tissue vary drastically in diameter, from 30 up to 200nm in diameter, as has been

measured through scanning electron microscopy imaging*(95)*. For purposes of our simulation, we utilized the upper limits of pore sizes.

Cellular content of the brain

Brain epithelial tissue cells (neuronal, and non-neuronal, excluding macrophages and endothelial cells) were harvested into a homogenous suspicion of cell nuclei and identified immune-cytochemically for rat brain cortex, cerebellum, olfactory bulb, and all remaining areas*(96)*. Brain-specific macrophages (microglia) were analyzed through immunofluorescence and flow cytometry in mice, specifically CD11b and CD45*(97)*. Brain endothelial content was taken online through the online mouse atlas obtained from www.mbl.org funded by the National Institute of Mental Health, National Institute on Drug Abuse, and the National Science Foundation. The brain contains a non-sinusoidal non-fenestrated blood capillary, with an inter-endothelial cell junction opening delineating the physiological upper limit of the endothelial pore size, which can be up to 1nm in diameter*(87)*.

Cellular content of the heart

Heart endothelial and epithelial cell content were obtained from Pinto et al.*(98)*, specifically, epithelial content included cardiomyocytes, fibroblasts, B-cells, T-cells, and other non-phagocytic or endothelial cell types. Endothelial cell compositions were obtained here as vascular and lymphatic endothelial cells. Cardiac macrophages were obtained through immunostaining and flow cytometry on resident macrophages *(99)*. The capillaries in the atrioventricular node and atrioventricular bundles of various mammals (rats, monkeys, mice, cats, and rabbits) were observed by tissue sectioning, where they discovered fenestrations of approximately 50nm in diameter, all bridged by a diaphragm. The non-specialized myocardium, however, contains continuous capillaries, so fenestrated capillaries were only found in the

conduction system of the heart.*(100)*. For purposes of our work, we assumed the heart to contain fenestrae of approximately 50nm in diameter.

Cellular content of the small and large intestines

Total numbers of epithelial cell content for the small and large intestines were taken as the sum of total number of epithelial cells in both the crypts and villi of the intestines for rats through microscope analysis*(101, 102)*. Macrophages of the small and large intestines were obtained through Lee and colleagues as monocytes per mg of tissue through immunoassay procedures*(103)*. Total capillary volumes were obtained for the small and large intestines and the average volume of mammalian cells were used to calculate the number of endothelial cells per gram of small and large intestines*(104)*. Visceral capillaries of the small intestine jejunum mucosa contain rounded openings with diameters from 50-80nm in diameter using freeze-dried tissue sections of adult rats*(105)*. The large intestine can contain diaphragmed fenestrae, which range between 60-80nm in the intestinal mucosa*(87)*.

Cellular content of the spleen

Total splenic epithelial content (splenocytes) were analyzed through immunostaining for a mouse and divided by the mass of the average spleen to obtain epithelial cellularity *(106)*. Macrophage content were obtained through Lee and colleagues as monocytes per mg of tissue through immunoassay procedures*(103)*. Splenic endothelial content were obtained through immunostaining and flow cytometric analysis for total endothelial cells per spleen for mice *(107)*. The capillaries of the spleen are sinusoidal, with a deficiency in the basement membrane. The inter-endothelial cell junctions are made up of cuboidal endothelial cells lining the splenic red pup located about 2-3um apart*(87)*.

Cellular content of the muscle

Epithelial and endothelial skeletal muscle cells were isolated from the forelimbs and hind-limbs of mice through enzymatic digestion and analyzed for immunocytochemistry*(108)*. Macrophage content were analyzed through mouse skeletal muscle immune-histochemical analysis and flow cytometry from digested whole muscle. Here, macrophages were treated as resident macrophages*(109)*. More than 60 cross-sectioned blood capillaries in adult rat skeletal muscles were located close to the muscle fibers, with diameters of 60-80nm, closed by a diaphragm at the center of the pore*(110)*.

Cellular content of the skin

Skin macrophage content were assumed to be Langerhan cells, which make up approximately 2-8% of epidermal cells in the skin.*(111)*. From Monteiro-Riviere study and skin cross sectional areas and depths, we can estimate the number of epithelial tissue cells per gram of skin*(112, 113)*. Skin endothelial cell content were taken from using an average fraction of endothelial content for the skin*(10)*, volume of the skin*(80)*, and volumes of a single cell*(114)*. Rat sub-epidermal layers of the foot were examined through scanning electron microscope and found to have fenestrae with a diameter of 50-60nm in diameter enclosed by a diaphragm*(115)*.

Animal simulation verification and validation

After model construction, the full in-vivo model was systematically verified against published datasets for primarily the intravenous exposure routes, as this is the first step in predicting biodistribution within animal tissue. *(13, 80, 116-125)*. Consistent with World Health Organization (WHO) recommendations*(126)*, our model was validated to ensure that:

1. All mathematical errors are fixed so that all equations and parameters are correct
2. Units are consistent and properly incorporated into all parameters and lines of code
3. Laws of mass balance are obeyed so that there is no inappropriate loss of compound
4. Model outputs are devoid of error and model successfully runs with desired outputs

We expected model outputs, if assumptions and simulations exhibited sufficient parsimony, to deviate only within a factor of 2, which is the level of adequacy frequently accepted among government agencies and pharmaceutical consortiums *(127)*. However, it is expected that some level of variation will be observed for tissues not used for specific rate kinetic determination or NMs with sizes below 10nm and above 500nm. Uncertainties in the model were also assessed through sensitivity analysis for differences in sizes for NMs predicted to enter the tissue interstitial space. In short, this analysis evaluated how the optimized parameters influenced the observed model output. We expected and showed that small changes in NM size leads to changes in predictions of the dose metric that are less than the variation of experimental measurements. All statistical validation was run by comparison of model outputs to in-vivo outputs through mean fold error analysis in equation 4 below,

$$MFE_t = 10^{\frac{1}{n}\sum \log\ (FE)} \quad (15)$$

where n is equal to the number of concentration values obtained from a single study for a particular time point and FE is equal to the fold error, which is the ratio of the model output and observed concentration at time, t. Overall model tissue output concentrations will be compared to observed through log-log analysis. Specifically, the log of the average of the model outputs will be compared to the log of the average of the observed outputs at various time points per tissue will be compared on a log-log plot. If the simulation exhibits very good predictive power,

we expect the simulation to exhibit a good positive correlation (R^2) between the predicted and observed NM concentrations*(27)*.

CHAPTER V. EXPOSURE OF QD TO CELL TYPES AND RATE CONSTANT OPTIMIZATION FOR PREDICTION OF ANIMAL BIODISTRIBUTION

As described in the previous chapter, once a NM has entered and circulated through the animal blood supply and entered the tissue environment, it will interact with tissue cells via adsorption, desorption, and internalization, all primarily active uptake processes *(128)*. This interaction with cells is critical and needs to be captured in order to assess how much NM has accumulated within the animal tissue cell environment.

Tissue cell rate constants must be obtained for relevant NM and tissue cell types

For proper extraction of in-vitro rate kinetics and translation to animal simulations, these kinetics must be obtained for a NM that exhibits similar physicochemistry to those analyzed in real animal studies. Given that we found no significant difference between uptake of NMs within the 30-500nm range and there exists no significant differences between NMs of like charge within that range, we identified the target physicochemistry as 30nm with a negative zeta potential as a reasonable prototype system. Furthermore, if degradative effects are present, e.g. through lysosomal degradation or phase I/II metabolism, we must be sure to understand and capture these effects. Thus, the already validated QSH QD used in chapter II of this work was chosen as the NM for rate extraction to animal studies.

Next, rate constants must be obtained for relevant tissues, i.e. those commonly encountered in-vivo. As exhibited in a variety of studies, the liver and kidneys seem to be tissue types with substantial NM sequestration, due to their fenestrae sizes within the blood vessels as well as their influence on metabolism and excretion of NMs*(129)* . Furthermore, the cells that make up the mononuclear phagocytic system (MPS) are heavily involved in removal of NMs from the blood

supply (monocytes) or tissues (resident macrophages)*(130)* and should be accounted for. We understand that tissue specific macrophages may be more aggressive e.g. Kupffer cells vs. monocytes, but for purposes of this pilot study, we wanted to capture differences between immune cells and epithelial/endothelial cells. Thus, monocytes were chosen as the model system. Finally, given that endothelial cells line the vasculature throughout all tissues and the entire body, we considered these cell types

Thus, to quantify this transport and accumulation within tissue cells and extract rate kinetics for animal simulations, we exposed the previously validated QSH QD to cells commonly encountered*(131)* by NMs upon intravenous injection: macrophages (J774a.1), endothelial (C166), and epithelial (liver and kidney, or AML12 and MES13 respectively) cells. Average tissue cell uptake was captured through the previously described cell kinetic assay (**Fig. 10A**, schematic).

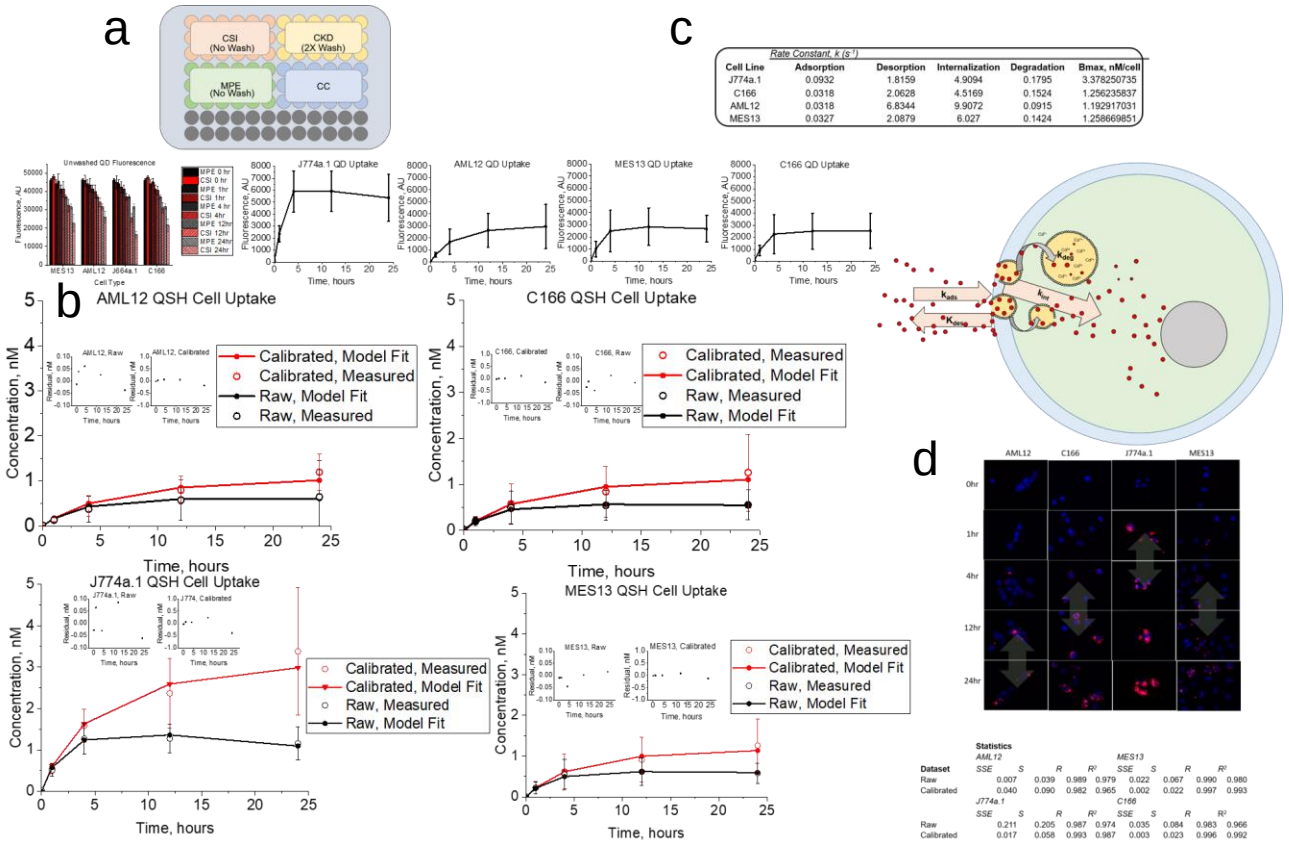

Figure 10. In-vitro application of assay using multiple cell types with simulation and rate extraction. a, Fluorescence data and assay setup representing unwashed QD fluorescence for unwashed wells that contain kidney(MES13), liver(AML12), endothelial(C166), and macrophage(J774a.1) cell types. **b** Washed raw (black) and calibrated (red) fluorescence uptake concentrations (circles, measured) compared to simulation fits (lines) for liver, endothelial, macrophage, and kidney cell types. **c,** Summary of rate constants optimized by the genetic algorithm for model fit to measured datasets. **d,** Time-dependent confocal microscopy images of QD uptake, showing saturation (double-sided arrows) for each cell type in the study. Cartoon is a visual representation of QD-cell interaction kinetics

Calibrated and raw concentrations for cell types were obtained and use as inputs for in-vitro simulation

Raw signals (I_{CKD}, **Fig. 10A**) were calibrated for degradative effects through ratiometric analysis using equation 1 above. For comparison, raw concentrations were obtained from I_{CKDt} relative to the unwashed CSI compartment at time 0 (I_{CSI0}). These results were entered into a cell kinetic simulation to obtain rate constants of averaged NM-cell interactions that are translatable to our whole-body (in-vivo) simulation, see below. All data were above the limits of detection (LOD) and quantitation (LOQ) with minimal trypsin interference (**Appendix A22**).

As **Figure 10b** indicates, $[Uptake]_{c,t}$ values are considerably higher in macrophages (J774a.1) than all other cell types ($P<0.05$), with macrophages taking up approximately 34% of dose, followed by kidney and endothelial (12.59% and 12.56%, respectively), and liver (11.93%) cells. This is interesting, as it is commonly observed that macrophages exhibit a more aggressive form of uptake, known as phagocytosis. Overall, the assay displayed enough precision to detect differences in uptake for tissue types expected to interact with NMs in-vivo. However, tissue types not involved in immune response (epithelial and endothelial) exhibited total uptake within similar orders of magnitude, so it is reasonable to extrapolate rate constants from these epithelial tissue cells to other epithelial tissue cells in mammalian species for now. Further studies can be performed to incorporate additional cell types in this assay to understand kinetics involved with more tissue-specific cell types.

Cell kinetics simulations were built to use the quantitative data obtained from the assay reported here to extract rate kinetics of NM-cell interactions. This cell kinetic model was guided by biologically relevant interactions that NMs undergo with cells of a tissue including NM adsorption, desorption, internalization, and degradation through fist-order rate constants k_{ads}, k_{des}, k_{int}, and

k_{deg}. Cells exhibited a saturable uptake profile, with saturation reached at approximately 12-24 hours. For extrapolation to animal studies that last longer than 24 hours, we needed to include this phenomena. Consequently, we constrained the adsorption to have a maximum rate of uptake when total uptake in cells ($[Uptake]_t$) is zero (0). As the NM gets taken up by the cells, the rate of uptake should decrease as $[Uptake]_t$ approaches the maximum capacity of NM uptake for the designed study, or B_{max}, included in equation 16 below,

$$k_{ads} = k_{a,max} * \left(1 - \frac{[Uptake]_t}{Bmax}\right) \quad (16)$$

As total uptake increases, we expect the rate of internalization (k_{int}) to also decrease as $[Uptake]_t$ approaches B_{max}, as shown by equation 17 below,

$$k_{int} = k_{imax} * \left(1 - \frac{[Uptake]_t}{Bmax}\right) \quad (17)$$

Eventually, both values (rate of adsorption and internalization) should reach zero as the total quantities of [Uptake]t approach B_{max}. These maximum rates of uptake were substituted for k_{ads} and k_{des} for later extrapolation to animal simulations.

All fluorescence based concentration data shown in **Figure 10b** were used to optimize cell kinetic model parameters k_{ads}, $k_{des,}$ k_{int}, (ratiometric calibrated datasets) and k_{deg} (raw datasets). At model convergence (<100 generations), the optimized parameters provided reasonable average correlation coefficients, coefficients of determination, and standard errors ($R > 0.983$, $R^2 > 0.965$, and $S < 0.205$nM), respectively, for all calibrated and raw datasets and cell lines with residuals randomly distributed around zero (**Fig. 10b**, insets). As shown in **Figure 10c**, the membrane adsorption rate constant was highest for macrophages and lowest for endothelial and liver cells. This is interesting, as macrophages are generally more aggressive, given their internalization type (phagocytosis). However, the internalization rate was highest for liver tissue cells and lowest for endothelial cells. Overall, each cell type had membrane adsorption as the rate-limiting step. We attribute this phenomena to the like charges exhibited by both the QD and cell membrane surface

(negative), so electrostatic repulsion is most likely the phenomena that hinders NM binding to the cell surface. After accumulation on the surface, the QD would then be internalized. Furthermore, all cells exhibited different total NM uptake capacities (B_{max}), as shown by their saturable profiles after 24 hours of exposure. Confocal imaging (**Fig. 10d**) visually supports this data, with rapid uptake and saturation by macrophages within 1 hour of exposure, and a more delayed uptake for the epithelial and endothelial tissue cells.

Animal simulations are validated at the cellular and tissue level

Due to the liver and spleen being common targets for NM sequestration, we used these tissues as case-studies to understand and capture the sensitivity and accuracy of the simulation's tissue and cellular outputs to changes in NM size*(131, 132)*. NM reflection coefficient calculation and inclusion in the transport mechanism involved within these tissues is briefly shown in **Figure 11a,b**.

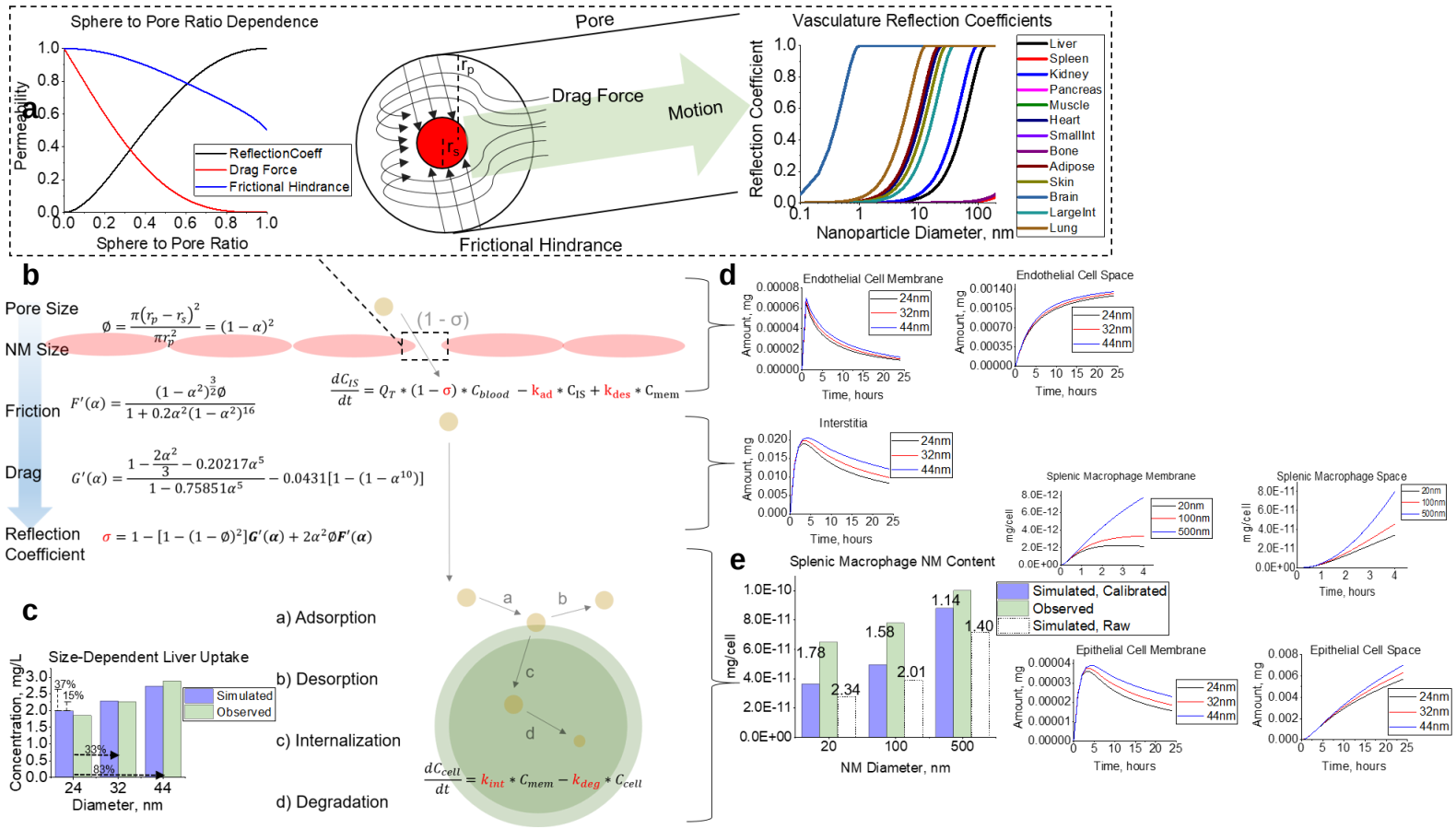

Figure 11. NM transport from blood supply to cell environment validation. a, Paracellular transport of NM through the endothelial fenestrae. Frictional hindrance and drag force are considered when calculating for the reflection coefficient, which is performed for each tissue type. **b,** Schematic of the NM transport process through the endothelial lining into the interstitial space from where it will interact with tissue cells through rate constants. **c,** Tissue level (liver) simulation predictions for variable-sized NMs compared to observed. **d,e,** Examples (**d**) of cellular level simulation outputs for variable-sized NMs (**e**) compared to observed splenic macrophage data for validation of rate constants and simulation output. Raw simulated data using rate constants with degradative effects (dashed) show increased error >2-fold for 20 and 100nm.

Figure 11c shows that a 33 and 83% increase in particle size will produce an increase of 15 and 37% uptake in total liver tissue. When compared to observed data, this lies within 2-fold error and follows the same observed positive correlative trends between size and uptake. This phenomenon can be explained through the fact that as NM size increases, such that it exceeds other tissue pore sizes, the NMs from those tissues should then funnel towards tissues with larger pores- in this case, liver. Variable (20-500nm) diameter biodistribution analysis using Chen 2015 datasets*(132)* (**Appendix A23**) support this principle. Upon reaching the target tissue, the NM will interact with cell populations through rate constants determined in-vitro. Here, we can see that liver endothelial cells (**Fig. 11d**) have direct exposure to the blood supply, and thus have immediate interaction with the NMs at the tissue site, with saturation at approximately 24 hours (Alalaiwe study). As the NM enters the interstitia of the tissue, it quickly interacts with epithelial (liver, Alalaiwe study) and macrophage (spleen, Chen study) tissue cells through our in-vitro rate constants. To validate overall model quantification at the single cell level, we used splenic macrophage uptake data from the Chen study*(132)*. When using the in-vitro rate constants calibrated for degradative effects, all simulations show accurate predictions (<2-fold error) for NMs ranging from 2-500nm in individual macrophages when compared to observed harvested splenic macrophages (**Fig. 11e**). If simulations used rate constants optimized to raw datasets, all simulation predictions would severely under-predict NM uptake in macrophages, leading to >2-fold error for most outputs (**Fig. 11e**). These results build confidence in the predictive power of the simulation and capability to predict variable-sized drug content at the single cell level for animals for the first time, strictly from in-vitro data.

Animal simulation validation across species and NM types

To build confidence in the simulation's predictive power and translational capabilities for different classes of NMs and species of animals, predictions were compared against measured tissue-level content for multiple NM types and species. Complete sets of physiological values (tissue volumes and blood flow rates) were obtained for three species including rats, mice, and NHP in order to scale cellular content (epithelial, endothelial, macrophage). The NM animal simulation was validated to 15 pre-clinical datasets, which included different dosing scenarios (0.029 - 64.3mg/kg BW), NM types (polymer, QD, metal, and antibody), and NM sizes (4-197nm diameter), all shown in **Figure 12a-e**.

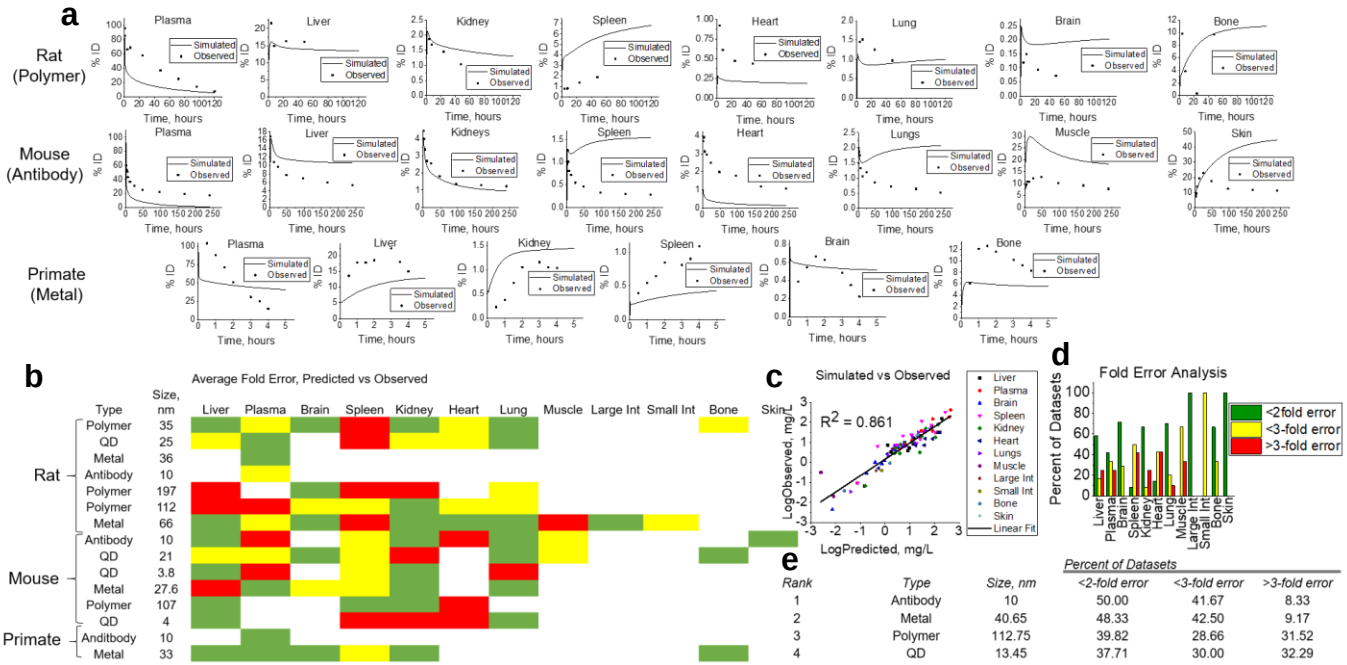

Figure 12. Simulation outputs for validation to various animal studies. a, Tissue-level predicted (line) vs observed (points) examples for all species types (rats, mice, and NHP) for visual evidence of model capabilities. **b,** Heat map of fold-error analysis calculated for all tissue, NM, and species types in simulation. Green, yellow, and red represent <2-fold, <3-fold, and >3-fold errors. Fold error was calculated according to equations given in methods section where simulated dataset averages were compared to observed. **c,** All data point averages specific to tissue types for simulations and observed were plotted against each other to yield a linear fit (R^2 = 0.861). **d,** Tissue-specific fold errors are shown to visualize model accuracy for each tissue in this study. **e,** NM simulated outputs were ranked (1-4) according to fold-error analysis.

As most laboratory biodistribution data only captures total uptake at the tissue level, validation of our simulation included total tissue (sum of macrophage, epithelial, endothelial, vascular, and interstitial) content. Evaluations of predictive performance were performed according to world health organization guidelines*(133)* as well as standards accepted by pharmaceutical and academic consortiums*(134)* involved in drug development and safety. Specifically, 49.78, 33.31, and 16.90% of datasets lied within <2-fold, <3-fold, and >3-fold error respectively, demonstrating reasonable model performance. Antibodies*(38, 135, 136)* exhibited the highest percentage of distributions lying within 2-fold error, followed by metal*(131, 137-139)*, polymer*(140-143)*, and QD-based*(144-147)* NMs (**Fig. 12e**).

Although assumptions of spherical morphology are not quintessential for antibodies, this assumption was practical enough for high model predictivity for this NM. Just like other materials in the nanometer range (~10nm), their distribution properties are also limited by biological membranes, so size, charge, and molecular weight will affect their biodistribution*(135)*. Although no metabolic clearance mechanism is included in the simulations yet, 50% of IgG plasma outputs lied within 2-fold, 42% within 3-fold and 8% greater than 3-fold error, suggesting good model predictivity. Plasma outputs generally under predicted uptake, most likely due to lack of IgG-endothelial FcRn receptor binding*(148)*, which future in-vitro assays could capture. Simulation outputs were slightly overestimated for tissues with high FcRn expression where IgG catabolism is prominent*(149)* (**Fig. 12a**., skin, muscle, and liver). IgG catabolism would be a necessary improvement in order to correct the simulation over estimation for these tissues (1.70, 2.30, and 1.42 fold-error over estimate).

Substantial analysis was performed in major reticuloendothelial system (RES) tissues (liver and spleen), each with differing uptake profiles and relative quantities, dependent on tissue macrophage content. Overall, simulations mostly fell within 2-fold error of observed values for

many of these studies, but generally under predict total tissue content primarily due to transcellular transport not being accounted for in our simulation. This effect is prominent for simulation outputs for the 25nm CdSe/ZnS QD (liver, **Appendix A24**) and 4nm CdTe-MPA*(147)* QD datasets for a variety of tissues (**Appendix A25**). The 25nm CdSe/ZnS-LM QDs showed accurate (<2-fold error) liver tissue predictions when compared to observed data from live animal studies*(144)*, with a larger proportion of uptake in macrophages relative to epithelial cells, as both simulation and literature electron microscopy evidence shows (**Appendix A24c**). In this case, observed data from these studies positively correlates NM accumulation within Kupffer cells to minimal biliary or fecal excretion, demonstrating the significance and balance between macrophage and epithelial cell interactions with NMs in living systems. The spleen, with approximately 10X more macrophage content than the liver (**Appendix A24d**), exhibited relatively higher percentage macrophage uptake than liver tissue for 28nm PEG5000-Au*(138)*(mice) 33nm PEG2000-SPIO*(139)* (NHP), 66nm PHEA-SPIO*(137)*, 35nm PEG2000-PAA [44] , and 106nm PS-PEO*(143)* NM types (**Appendix A24**).

Peripheral tissues like the brain and lungs experienced quick saturation within the first hour, with a slight clearance profile most likely due to NM accumulation within tissue vasculature and limited permeation through the blood-brain barrier (BBB) and capillary fenestrations (**Appendix A26**)*(138-140)*. Observed TEM evidence supports localization within tissue vasculature and simulation data predicts and substantiates this finding*(139)*.

For studies where metabolism was observed, our simulation either exhibited over estimations or did not fit the observed tissue profiles. Simulations overestimated polymer-based 66nm PHEA-SPION*(137)* where biliary and renal clearance were present and failed to match the correct liver profile for 112nm PGA*(142)* where substantial biliary clearance (65% ID) was an influential factor (**Appendix A27**). Although reasonably matched to observed data (<2-fold error), simulations

under predicted liver and kidney uptake of 21nm CdSeS-SiOH QD (**Appendix A28**). However, study results also show significant fecal/biliary (33%) and urinary (24%) elimination (localization within kidney cortex proximal tubules and liver lobules involved in elimination *(145)*). In this case, transcellular transport and biliary excretion would serve as additional model assistance. Contrary to the 21nm QD, 3.8nm MSA-QD exhibited minimal renal and biliary clearance (**Appendix A28c,d**) primarily due to considerable QD accumulation within interstitial space (30 min) and gradual accumulation within mesangial cells*(146)* after prolonged periods (**Appendix A28e**). Moreover, electrostatic repulsion from the proteoglycans in the basement membrane of the glomerulus fenestrae on the small QD are believed to influence minimal renal elimination, which can be addressed through additional computational approaches using surface potential of endothelial cell membranes*(150)* and subsequent*(151)* repulsion

Our simulation reasonably predicts biodistribution for PEG2000 and 5000-coated Au, with plasma concentrations lying within 1.45 and 1.52 AFE respectively (**Appendix A29**). However, our simulation does not account for blood half-life as a function of trends in PEG chain length (resistance to aggregation by providing minimal protein adsorption), so this effect is not expressed in simulation outputs*(152)* thus far. We expect, as transcellular transport is included as an additional tissue uptake mechanism, NM should escape plasma and enter the tissues thereby correcting the 66.67% simulated overestimations. Plasma profiles for NHP show zero-order elimination kinetics (attributed to the NHP glomerular filtration rate or GFR) which our simulation does not yet demonstrate and would need to account for in the future. PGA particles also experienced a rapid initial plasma elimination phase (about 50% of ID within 1 hour of exposure (**Appendix A29**), indicating immediate distribution to tissues with large fenestration such as the liver and spleen, which is consistent with literature values*(142)*.

Overall, NMs between 10 and 100nm diameter (n=65) exhibited the best predictive capabilities for our simulation (>50% below 2-fold error for all tissues), most likely due to the fact that 1) cellular rate constants obtained in-vitro translated well to the live animal simulation, 2) paracellular transport through endothelial fenestrations was the primary means of tissue transport, and 3) biliary and/or renal clearance of NM minimally affected biodistribution. Approximately 50% of tissues within datasets containing NMs with diameters <10nm (n=10) lied above 3-fold error and 40% lie below 2-fold error. For NMs >100nm in diameter (n=16), the simulation demonstrated similar errors within all error ranges (36.43, 25.71, and 37.86% <2, <3, and >3-fold error respectively). Here, we suspect NM size to exceed pore diameter, limiting tissue uptake, so transcellular transport would be necessary to fully capture tissue uptake. Simulated and observed datasets were compared through log-analysis of the averages of the datasets and plotted against each other, as shown in **Figure 12c**. Model predicted averages and observed averages were fairly linearly correlated, indicative of reasonable model predictivity across all species and NM types (R^2=0.861).

CHAPTER VI. INNOVATION

The EPA, FDA, NIH, and NRC have all recognized the need for new tools to assess toxicology of nanomaterials. In particular, the involvement of in-vitro cell culture and assays have been called for, with in-vitro to in-vivo extrapolation of pharmacokinetic computer models towards hazard assessment*(62)*. The combination of in-vitro and in-silico methodologies delivers a solution to calculate true effective doses at sites of interest and derive potential dose-response relationships that lead to calculated predictive developmental and reproductive toxicity, human safe exposure levels, and hazard rankings, all from inputs that translate between in-vitro and in-vivo *systems* and between species for different exposure routes. The innovation in this approach stems from the ability to predict cross-species in-vivo target cellular dose from in-vitro data alone, with no animal data necessary as inputs. Moreover, the mechanistic nature of this affords the capability to execute potential hazard assessment for any NM type, originating from its consideration of the NMs physicochemistry and effects on mechanistic biological processes that determine cellular dose at tissues. Results are obtained in minutes through optimization of software architecture on desktop hardware. Key outcomes are rapid screening of nanomaterials and their dose-dependent effects toxicity, with benefits for protection of human health starting from a predictive understanding of dosimetry at the cellular level in the body.

Advantages and limitations of the overall method

Our method makes use of the combined in-vitro assay-simulation approach in a way that is simple to apply in the lab. Labs that have cell culture capability and access to a plate reader and computer can use the reported method. The major disadvantage of our method is that NMs have to be fluorescent. NMs can be made fluorescent with dye coating but it could lead to questions about changing the nature of the NM surface, and would require developing proof, if possible, that there

is no difference. Materials that degrade fully (or full loss of fluorescence) on the time scale of the assay would not work.

Importance of the method

NM kinetic data representing interaction with cells is required for accurate predictive modeling of NM in-vivo, but has been challenging to deliver to the pharmacokinetic modeling field. With our method, these data can be obtained quantitatively. Rate constants optimized to cell uptake data, obtained from our method, are valuable in that they may couple directly to in-vivo biodistribution modeling. This enables predictive power for NM animal simulations while obtaining biodistribution data with cellular level resolution starting from in-vitro assay alone. Tissue level resolution can now be enhanced to the cellular level through rate constants determined from the in-vitro portion of the RCF method. In the future, this method can provide a streamlined approach to enable much quicker and cost-effective NM screening for nanomedicine, public safety, and answering broader regulatory questions.

Future Work and Improvements

The need for high-throughput screening and predictive analysis is unavoidable given the widespread distribution of NMs*(153)*. NMs in these products come with a variety of physicochemical properties that affect the manner in which they are exposed to humans. Exposure can happen in a variety of ways including inhalation, oral, dermal, and intravenous injection, all affecting biodistribution and subsequent target tissue/cellular dose. In the case of inhalation and oral exposure (most common), NMs need to absorb into the blood supply through the gastrointestinal (GI) or respiratory tracts, all dependent on their physical properties. This, in turn, affects the systemic distribution of that particular NM, which affects the dose delivered to tissue cells. Moreover, all tissue cells can interact with a particular NM differently, also affecting

the exposure dose. Consequently, this variance in absorption and systematic distribution causes huge deviations in toxic response, which complicates the issue of human safety. This complex road map of NM biodistribution must be included in future versions of this work, to account for NM sequestration within the respiratory/gastro-intestinal tracts and potential skin lining. The current version of the simulation only accounts for 3 specific cell types- epithelial, endothelial, and monocytic, which can be expanded in future versions of this work given the body contains substantially more cell types with variations in expression at any given time. These additional cell types can be incorporated in the RCF assay as co-cultures if necessary. The in-vitro assay currently was run for immortalized cell lines, which can be expanded to primary cells if there is concern for relevance to live animal physiology, e.g. receptor expression on the cell surface.. Furthermore, the increase in cell type expression can be included in the animal simulation as a changing state variable, given the dosing situation or presence of inflammation. NMs that exhibit targeted effects can be run through this assay, as cell lines overexpressing receptor sites of interest can be plated on the 96-well system. Here, rates of cellular kinetics will then represent these targeted effects and can be extrapolated to animal studies.

Discussion

A NM injected into the blood supply of a living mammal will not be the dose delivered to individual cells of a tissue. Modern medicine currently has substantial difficulty in assessing dose delivered to individual cells due to technological limitations. Furthermore, optimal NM drug development for a particular disease requires a quantitative and accurate understanding of where the drug will go, preferably during the early stages of development. We have advanced these technological capabilities through a unique bottom-up approach that predicts live animal biodistribution of variable NM types for a variety of species from in-vitro data alone, and with cellular resolution. This combination of in-vitro and in-silico methods is expected to help assist for future smart drug

design and can be a platform to help scientists make better informed decisions while reducing live animal testing.

Our reported work expands on extensive simulation work between drug design and biodistribution for conventional small molecule-based drugs to inform early and proper dosing scenarios for effective treatment. More recent NM simulations have begun to model biodistribution in animals, but often fit tissue and blood partition coefficients to animal data in order to describe equilibrium partitioning between the two phases. Substantial work has been done to improve on this*(40, 41)*, but limitations in tracking mechanistic transport from vasculature to cells and the subsequent cell interactions still remained. Our work makes significant advances through the implementation of a mechanistic fluid dynamic simulation coupled with in-vitro cell interaction kinetics to provide a much higher resolution of NM quantitation.

NMs sequestered in the interstitia of a tissue alone may not have a therapeutic or toxic effect on the cells, so it is critical to track cell uptake phenomena. As we can see from our simulation results, epithelial tissue cells require substantial time to internalize drug, sometimes up to 48 hours. In some cases, only 0.94% of the total tissue dose will be located within the epithelial cells, so for example, even though the liver would have taken up 14.0% of the injected intravenous dose only a small portion will have actually reached the tissue cells. In this case, perhaps the scientist may want to increase the injected dose, change the size of the NM, or completely alter the surface chemistry and run in-vitro simulations again to obtain higher rate constants. This is important as well in understanding unintended sequestration of NM in peripheral organs. For example, because the body is a working system, the other tissues, like the kidney, may also take up particles and lead to inadvertent build-up and possible toxic response. By virtue of the simulation outputs, a scientist can minimize this risk by being able to predict and address these issues.

Our implementation of variable reflection coefficients affords the capability to quantitatively track the differing NMs in variable tissue types from the blood supply. This gives valuable insight into how effective NM may be in going from blood to tissue. Additionally, diseased states as well as alterations in vasculature endothelial growth factors (VEGF) can alter fenestration development and expression, so this advances understanding in quantifying these phenomena. Although this flexibility is critical, we currently assume the NM as a perfect sphere traveling through a cylindrical pore. Biologics like antibodies may not follow this assumption completely, but the assumption is parsimonious enough to reasonably predict the distribution within tissues. Even with the overall small error we found in the model predictions, the simulations generally under-predicted the total tissue content. This can be addressed through future inclusion of transcellular transport of materials through the endothelial cell lining. When this effect is accounted for, we expect the simulations to increase predictions and match observed total tissue content.

Future work is necessary to truly consider all mechanistic processes within whole-body simulations. Processes like antibody catabolism, metabolic (phase I and II) breakdown and clearance of NMs, and transcellular transport of NMs through the vascular lining will need to be included in order to provide additional model flexibility and predictive power. Differences in physicochemistry like charge and lipophilicity will affect transport through the vasculature lining and may need to be accounted for, which can be captured through correlations between structure to biological activity (QSAR). Our study provides a substantial leap forward in predictively tracking and quantifying NM transport in live animal tissues starting from in-vitro data alone.

In summary, the in-vitro concentration data from our ratiometric assay coupled with our cell kinetics simulation delivers rate constants for cell-NM interaction that show excellent translatability to our mechanistic predictive in-silico whole-body animal simulation. We have also shown that the process works under conditions where the NM experience degradation by the biological

environment. Thus, we have demonstrated a viable platform for reduction, refinement, or replacement of animal testing for NM development.

CHATER VII. METHODS AND MATERIALS

Commercially available quantum dot QSH (negatively charged CdSe/ZnS core-shell), and functionalized polystyrene nanoparticles (PS) were purchased from Ocean NanoTech, LLC and Magsphere, Inc, respectively. All materials were used as-is, unless otherwise specified in main text.

In-vitro Statistical Analysis

Statistical analysis was performed on Microsoft Excel 2010. All calculated statistical evaluations were performed using the student's two-tailed t-test at the $P<0.05$, $P<0.01$, or $P<0.001$ level.

Processing and Reading In-vitro Assay in RCF Approach

All fluorescence measurements were taken with a top-read Tecan M200 Pro Plate Reader. Fluorescence for QSH was taken with excitation of 580nm and emission of 620nm. PS was excited at 525nm and emission was collected at 595nm. Zn-based quantum dots were excited at 300nm and fluorescence was obtained at 600nm wavelengths. All plate reader measurements were performed using four reads per well to obtain statistically relevant data. For compartments CSI, CKD, and controls, 100uL of a 347,000 cells/mL cell suspension (Hepa1-6, murine hepatoma, C166 murine endothelial, MES13 murine kidney mesangial, AML12 murine liver epithelial, and J774a.1 murine monocyte cell lines from ATCC) were applied and incubated for 48 hours in a black 96 well plate (96 well solid black flat bottom polystyrene TC-treated microplates, Corning) to allow for 80-90% confluence. At time of experiment, all compartments were washed 1X with complete growth media, aspirated, and 100uL aliquots the nanomolar-specified concentration for all NM types in DMEM (DMEM/Ham's F-12 50/50 Mix, Corning) supplemented with 10%FBS (Regular heat-inactivated, Corning) for all compartments (CSI,

MPE, and CKD) in plates designated for that particular NM type. For QSH validation studies, each well plate consisted of 18 replicates of each compartment, specifically CSI, MPE, CKD, and controls (CC) for 0, .5, 1, 2, 4, 6, 12, and 24 hours. For other NMs where validation was not necessary, one triplicate for MPE, CSI, and control was used, *but with 1 triplicate designated for each time point for CKD*. In both scenarios for NMs, at each time point, CKD wells were washed 2X with complete growth medium, 1X with PBS (Phosphate buffered saline, ThermoFisher Scientific), and trypsinized for 15 minutes (0.25% in EDTA, Invitrogen), mixed, and *fluorescent plate readings run on all well types (CSI, MPE, CKD, and control) with an excitation specified for each NM.* All fluorescence values were corrected for media and trypsin background signal. Specifically, I_{CSIt}, I_{MPEt}, I_{CKDt}, were all read at these time points. $I_{cdeg,t}$ and $I_{mdeg,t}$ were taken as the difference of I_{MPEt} and I_{CSIt} as well as $I_{MPE,0}$ and I_{MPEt}, respectively. Note: 0 hours consisted of an entire 96-well plate with aspiration immediately (<2 minutes) after application to all wells and subsequent washing and trypsinization of CKD. Fluorescent plate readings took approximately 2-5 minutes per plate.

RCF Parameter Outputs and Usage

Signals obtained from RCF assay include:

$I_{CSI,0}$

$I_{CSI,t}$

$I_{MPE,0}$

$I_{MPE,t}$

I_{CKDt}

I_{CC}

Overall, raw fluorescence descriptive of cell uptake ($I_{CKD,t}$) was taken relative to raw fluorescence of unwashed cells at time t ($I_{CSI,t}$) to obtain a calibrated fraction of uptake ($f_{cell,c}$):

$$f_{cell,c} = \frac{I_{CKD_t}}{I_{CSI_t}} \quad (18)$$

Raw fluorescence descriptive of cell uptake ($I_{CKD,t}$) was also taken relative to raw fluorescence of unwashed cells at time 0 ($I_{CSI,0}$) to obtain a raw fraction of uptake ($f_{cell,r}$):

$$f_{cell,r} = \frac{I_{CKD_t}}{I_{CSI_0}} \quad (19)$$

These two fractions were then used to obtain concentration of NM uptake using the general equation,

$$[Uptake]_{c,t} = f_{cell,x} * [Dose] \quad (20)$$

where $f_{cell,x}$ is the fraction of uptake for x = raw or corrected, $[Uptake]_t$ is the concentration of NM taken up by cells (nM), and *[Dose]* is the applied dose in nM. To determine if cell-induced degradation is present, a two-tailed t-test was performed between unwashed CSI and MPE compartments at time, *t*, (I_{CSI_t} and $I_{MPE_t}, respectively$). To determine if media-induced degradation is present, a two-tailed t-test was performed between unwashed MPE at time 0 and time *t*.

Cell-induced degradation (I_{cdeg_t}) was taken as the difference between unwashed without (I_{MPE_t}) and with (I_{CSI_t}) cell exposure,

$$I_{cdeg_t} = I_{MPE_t} - I_{CSI_t} \quad (21)$$

If media degradation was present, the intensity of this degradation type was taken as the difference between unwashed wells without cell exposure from time 0 to time t.

$$I_{mdeg_t} = I_{MPE_0} - I_{MPE_t} \quad (22)$$

Taken together, the sum of these values equals the total degradation that a NM can undergo for the RCF assay (I_{deg_t}):

$$I_{deg_t} = I_{cdeg_t} + I_{mdeg_t} \quad (23)$$

AAS Sample Preparation

For AAS validation of the above fluorescence RCF results, 50uL aliquots of aqua regia was added to every experimental well (both to unwashed/washed and cells/no cells) and left to digest for 10 minutes in incubator. In this case, every well received equal dilution for proper ratiometric quantitation. At time, homogenized solutions were collected and transferred to sealed glass vials for atomic absorption experiments. Care was made to ensure wells were kept at equal dilutions, 150uL of total solvent per well, *leading to a theoretical QSH concentration of 6.66nM for all unwashed wells.* Wells with unknown concentrations (washed cells) were diluted equally as wells with known concentrations of QSH. A Perkin Elmer Analyst 400 AAS spectrometer was used to analyze cadmium solutions. A cadmium hollow cathode lamp with wavelength of 288.65nm was used to obtain optimal cadmium absorption. Flow rate was adjusted to 4mL/min and samples were run in triplicate. A 6-point standard calibration curve was constructed with NIST grade $Cd(NO_3)_2$ in AR. Care was taken to ensure that sample readings were within the linear dynamic range of the calibration curve and limit of quantitation (LOQ) of the instrument.

AAS QSH Concentration Determination from Cd

AAS cadmium concentrations from CKD determined from the utilization of a standardization curve containing QSH concentrations of 0.25, 0.50, 1.00, 5.00, 10.00nM, and $Cd(NO_3)_2$ concentrations of 0.25, 0.50, 0.75, 1.00, 2.00, and 4.00mg/L. The slope of the $Cd(NO_3)_2$ curve was then used to build a new curve correlating QSH nM concentrations to Cd mg/L concentrations. These values were then used to compare AAS results to those in the RCF method.

Assessment of NM Toxicity

MTS (CellTiter 96 AQ Non-Radioactive Cell Proliferation, VWR) assay was run to determine toxicity of a variety of NMs at different doses (QSH and PS) for optimal NM exposure conditions. NMs were applied to cells for a period of 24 hours. Briefly, cells were seeded in triplicate onto wells of a clear flat bottom 96-well plates at a density of 34,700 cells/well and left 24 hours for attachment. At time, media was aspirated, and 100uL of all NM solutions were applied to wells, except controls, for a period of 24 hours in 37^{o}c CO_2 incubator. Negative controls were kept in media to retain complete viability and positive controls were kept in water for cell death. All NMs were diluted in DMEM supplemented with 10%FBS at various doses, ranging from 5nM to approximately 250nM. At time, cells were washed 2X with complete growth medium and re-applied with 100uL of DMEM with 10%FBS. 20uL aliquots of MTS was added and background absorbance was captured at 490nm. Plates were then incubated for 2 hours and absorbance checked again. Sample absorption values were normalized to that of cells exposed to complete growth medium.

Assessment of QD stability

To assess what dose of QSH would be optimal for the cell kinetic experiment media stability was determined. Time-dependent experimental data was taken for QSH at various concentrations. QSH solutions were made in DMEM supplemented with 10% FBS at concentrations 2.5, 50, 100, 200, 250, and 300nM. The solutions were applied in 100uL aliquots in triplicate to wells of a 96 well plate and left inside incubator for up to 60 hours. At each time point, fluorescence plate readings were taken with a constant z-optimized focal plane of 18181um, the maximum fluorescent signal-noise ratio. This value was kept constant throughout the time-dependent study to understand sedimentation effects.

Lysosomal Colocalization Studies

Cells were seeded onto 35mm diameter tissue coated petri dishes (35mm TC-treated culture dish, Corning) with 2mL of 347,000 cells/mL solution and left in incubator at 37ºC and 5%CO_2 for 24 hours. Cells were washed 1X with complete growth medium and 2mL of 10nM QSH solutions were added. After 24 hours, petri dishes were removed from incubator and washed 2X with complete growth media. Lysotracker Green (DND-26, ThermoFisher Scientific) was added at 1uM concentration and confocal images obtained. Lysosomal colocalization studies were performed using a spinning-disk confocal imaging system. Z-stacks were taken at 2um step sizes, with a total distance of 40um.

Cell Kinetic Confocal Microscopy

For each NM analyzed for uptake, we used confocal microscopy. At each time point in the RCF study, cells were washed 2X, trypsinized, and transferred to 35mm petri dishes containing 2mL of complete growth medium. After 24 hours, cells were washed 2X with complete growth

medium, and Hoechst33257 was applied. Cells were then imaged for NM uptake with 20 2um step sizes.

Simulated Lysosomal Buffer Studies

Cellular lysosomal environment was mimicked to determine stress induced on fluorescence through lysosomal material exposure. The citric acid (, >99.5%, ACS Reagent, Sigma-Aldrich) simulated lysosome chelator buffer at pH 2.5-5.0 was created and used as the solvent for QSH and PS. Controls contained pH 7.4 DPBS buffer solutions. More specifically, stock solutions of .25 and .19mM solutions of sodium citrate monobasic (Anhydrous, Sigma-Aldrich) and dibasic (Sesquihydrate, Sigma-Aldrich), respectively, were made. Stock solutions of 50mM and 20mM citric acid stock solution were made in separate vials as well. Then 6 solutions of equal concentrations of 10nM QSH and PS NM were made in either sodium citrate monobasic/dibasic with citric acid . To achieve desired pH of 2.5, 3.0 3.5, 4.5, or 5.0. pH was adjusted by combination of dibasic or monobasic sodium citrate stock solution with small aliquots of citric acid solutions. For size analysis, Zetasizer (Malvern) DLS measurements were obtained. Here, QSH and PS samples were diluted in-situ in solvents of desired pH and measurements obtained immediately after. Fluorescent plate readings were run in triplicates of 100uL of solutions applied to wells of a 96-well plate system. Fluorescence was taken with 580 or 525 excitation and 595 or 620nm emission, respectively for QSH or PS, using a Tecan M200 plate reader.

To check for Cd^{2+} core leakage, 10nM QSH and PS were analyzed for fluorescence in PBS, water, and simulated lysosomal buffer at pH 2.5, 4.5, and 5.0 at 0 hours and 24 hours exposure. For each time point, samples were collected and centrifuged at 15,000xg for 20 minutes through an Amicon Ultra 10kDa filter to separate possible cations from QSH. Filtrate was then analyzed for free cadmium content using a PerkinElmer atomic absorption spectrometer with a cadmium

hollow cathode lamp with wavelength of 288.65nm. Flow rate was adjusted to 4mL/min and samples were run in triplicate.

Prolonged Cell Exposure Study

Prolonged exposure to intracellular environment analysis was performed after washing at time, t. Here, QSH or PS washed samples at time, t, were left to incubate to an additional 12-x and 24-x hours, where x is the time of wash for each particular sample. At total experimental time of 12 and 24 hours, previously washed plates were mixed and measured for fluorescence changes from their original time, t. An example is shown below:

2 hours wash fluorescence → *10 hour post wash* (12-**2 hours**) fluorescence→ *22 hours post wash* (24-**2 hours**) fluorescence

Importantly, 12 hour washed sample only contained 24-x prolonged cell exposure data and 24 hour washed sample contains no prolonged exposure, given that cell exposure was only allowed for the duration of a total time of 24 hours.

Calculation of Fluorescent Plate Reader Limit of Detection and Quantitation

The limits of detection (LOD) and limits of quantitation (LOQ) were calculated from construction of an 8-point calibration curve with concentration ranging from 0.10-10 or 15nM for QSH or PS. The LOD and LOQ were calculated based on the standard deviation of the response signal of the blank and slope of the linear curve through zero, equations below:

$$LOD = \frac{3\sigma}{S} \quad (24)$$

$$LOQ = \frac{10\sigma}{S} \quad (25)$$

where σ is the standard deviation of the blank (NM suspension in trypsin) and S is the slope of the calibration curve. All readings were performed on a TecanM200 Pro.

Perkin-Elmer AAS Limit of Detection and Limit of Quantitation

The Perkin-Elmer AAS limits of detection (LOD) and limits of quantitation (LOQ) were calculated from construction of a 6-point calibration curve with concentration ranging from .25-4mg/L. Media signal in 33% v/v AR was used as blank for these values. The LOD and LOQ were calculated based on the standard deviation of the response signal of the blank and slope of the linear curve through zero, see equations 7-8.

Analysis of QSH Cadmium Core Leakage In Cell Supernatant

Cells were plated onto wells of a 96-well plate system at 34,700 cells/well and left to incubate for 48 hours. At time, media was aspirated and 100uL aliquots of 10nM QSH was applied. Cells were then placed in incubator for maximum experimental exposure time for 24 hours. After 24 hours, fluorescence measurements were taken for QSH with no cell exposure ($I_{MPE,t}$) and with cell exposure ($I_{CSI,t}$) to show difference in total fluorescence. All sample supernatant was collected separately and transferred to 2mL centrifuge tubes with Amicon Ultra 10K filters. Samples were centrifuged according to protocol at 14,000xg for 20 minutes to filter out solvent and possible free cadmium. Filtrate and concentrate were then collected analyzed on AAS for cadmium concentration.

Extraction, Collection, and Harvest Efficiencies

Extraction, collection, and harvest efficiencies were performed to ensure accurate and precise experimental protocol. For extraction efficiency, cell kinetic samples were washed 2X with complete growth media, trypsinized, digested in-situ and collected for AAS. In parallel, cells were washed 2X with complete growth media, not trypsinized, digested with AR in-situ, and collected for AAS. If full extraction of cadmium from cell interior is happening, both sample sets are expected to yield similar results, or close to 1 when normalized. Harvest efficiency was performed by collection of QSH from wells with no cells and wells with cells. In both cases, AR was applied in-situ and samples were collected for AAS. If full QSH cadmium harvest is apparent, then normalized data should yield values close to 1. Collection efficiency was performed by comparison of direct dilution of a separate vial of 10nM QSH to 6.66nM by AR application in parallel to QSH in wells with no cells and equal digestion in-situ with aqua regia. If all sample is collected from the wells, then the in-situ AAS values should yield similar results to the diluted vial and normalized close to 1.

In-Vitro Model Global Optimization Setup and Evaluation

All simulations were performed in MATLAB v2015b. Parameter optimization was implemented with the genetic algorithm (GA) optimization function from the Optimization Toolbox. Parameters for estimation included:

Initial Population: 300

Population Size: 50

Generations: 100

Mutation Rate: Mutation Gaussian

Crossover Rate: .80

Selection Function: Stochastic Uniform

The genetic algorithm was evaluated using the residual sum squares as the fitness function, equation below:

$$RSS = \sum_i^n (y_i - m_i)^2 \quad (26)$$

where RSS represents the residual sum of squares from model output (m_i) at time (i) to measured data (y_i) for n time points. Standard error was computed as

$$S = \sqrt{\frac{RSS}{n}} \quad (27)$$

where S is standard error, RSS residual sum of squares, and n is total time points.

Model output upper and lower bounds were evaluated at the 95% confidence interval through

$$CL\ (95\%) = Model\ Output \pm 2 * S \quad (28)$$

where CL(95%) represents 95% confidence limit.

The GA was run for 100 generations, enough to allow for convergence at a fitness value representative of measured data.

In-vitro quantitation of cellular uptake

To ensure repeatability, the fluorescence assay was completed approximately 2 months apart with a new batch of thawed cells for both NM types (n=2), with reproducible results. The fluorescence assay was built starting from the application of cells on a 96-well plate in 3 "compartments": the Cell System Interactions (CSI) compartment (*cells + NM (unwashed), accounts for cell-induced NM degradation*), the Cell Kinetic Data (CKD) compartment (*cells +*

NM (washed), measurement of NM uptake), and the Cell Control (CC) compartment (*cells in media + no NM (unwashed), control with untreated cells to subtract background signal*). The Media and Protein Effect (MPE) compartment (*no cells + NM in media (unwashed)*) accounts for media and protein induced degradative effects on the NM in the absence of exposure to cells. Note that the CSI and MPE compartments are never washed and therefore maintain the initial applied dose of NM (10 nM). The CKD compartment is washed at each time, *t,* to remove NMs that are not cell membrane bound or internalized by cells. Control experiments on blank wells showed minimal NM adhesion to the sides and surface of wells, indicating all fluorescence should strictly come from NM interacting with cells. For assay development and validation to AAS for QSH, we used 18 wells per compartment, which resulted in one 96-well plate per time point. For the application of this assay to cell types for rate extraction we used in animal simulations, we applied QSH at a dose of 10nM to each compartment in triplicate. At time of application, we allowed cells to reach 90% confluence and establish membrane integrity*(72)* (48 hours). At time zero, the CSI, CKD, and MPE compartments were dosed with 10nM QSH or PS (10% FBS DMEM suspension), with one NM type per plate. Comparing (by t-test) the fluorescence signal for wells in the CSI compartment at time *t* with the fluorescence signal from wells in the MPE compartment at time *t* gives insight into cell-induced degradation. If they are statistically different we conclude cell induced NM degradation is present and the quantity of fluorescence signal loss due to this effect is determined from the difference of CSI and MPE at time *t.* Similarly, comparing the fluorescence signal (by t-test) from wells in the MPE compartment at time *t* with respect to MPE at time zero gives a description of media-induced degradation. These critical steps guide NM uptake calculations, especially if degradation is present.

NMs analyzed in animal studies for simulation

The metal-based particles comprised of PEG2000 (32nm)*(131)* or 5000-coated Au (28nm)*(138)* and PEG2000 (33nm)*(139)* or PHEA (66nm)*(137)* coated SPIO NMs. Polymer based NMs consisted of PAA-PEG2000 (35nm)*(140)*, PLGA (197nm)*(141)*, PGA (112nm)*(142)*, and PS-PEO (107nm)*(143)*. QD studies varied substantially, as we analyzed hydroxide (CdSeS-SiOH, 21nm*(145)*), mercaptoundecanoic acid (CdSe/ZnS-LM, 25nm)*(144)*, mercaptosuccinic acid (CdTe/CdS-MSA, 3.8nm*(146)*), and mercaptoproprionic acid (CdTe-MPA, 4nm*(147)*) coated NMs.

APPENDIX A. SUPPLEMENTARY FIGURES

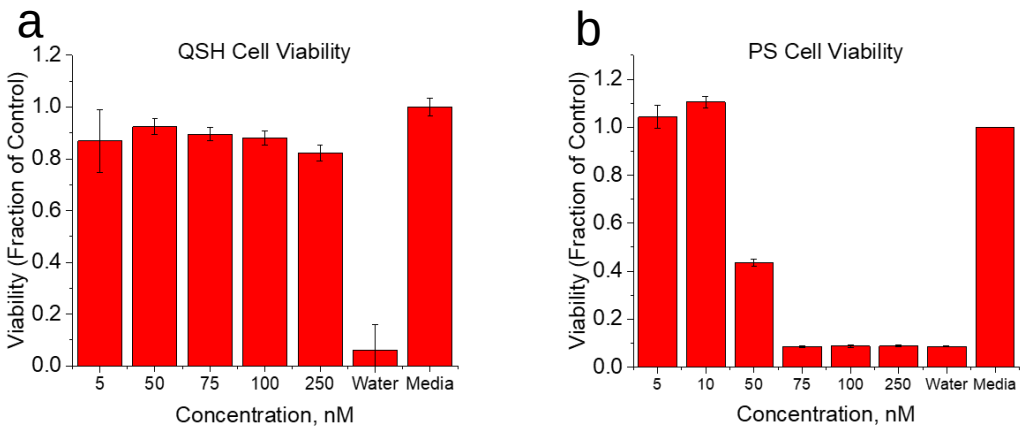

Appendix A1. MTS assay data for all NMs included in cell kinetic analysis. (**a**) QSH (negatively charged) and (**b**) PS. Negatively charged QSH experienced minimal toxicity for all doses, and PS exhibited minimal toxicity at 10nM or below. Positive control contained cells exposed to water and negative control contained cells exposed to complete growth media.

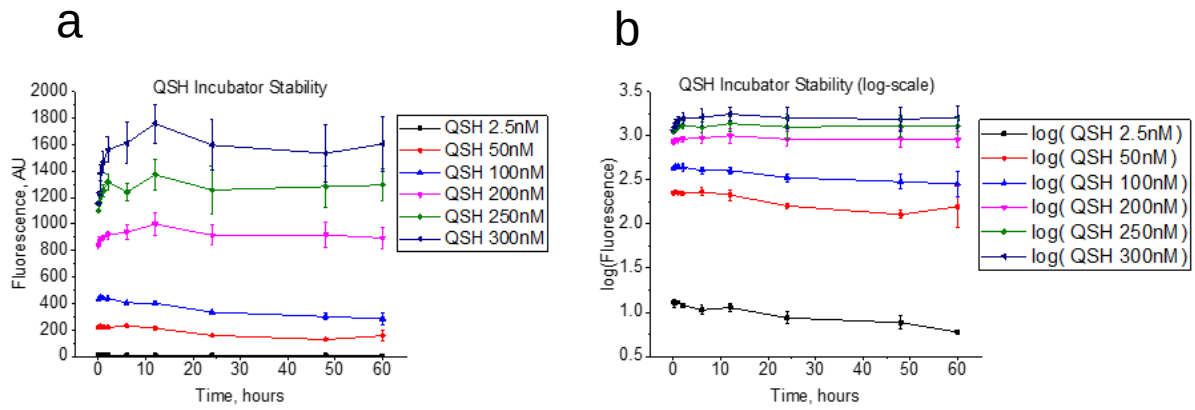

Appendix A2. QSH stability studies inside incubator at 37ºc and 5%CO_2. Fluorescent results for (**a**) and (**b**) indicate the relative stability of QSH at a 10nM concentration, reasonable enough to select for further cell kinetic analysis. Optimized detector Z-plane was kept constant on plate reader, as QD presence in the optimized focal plane decreased from sedimentation, fluorescence drops.

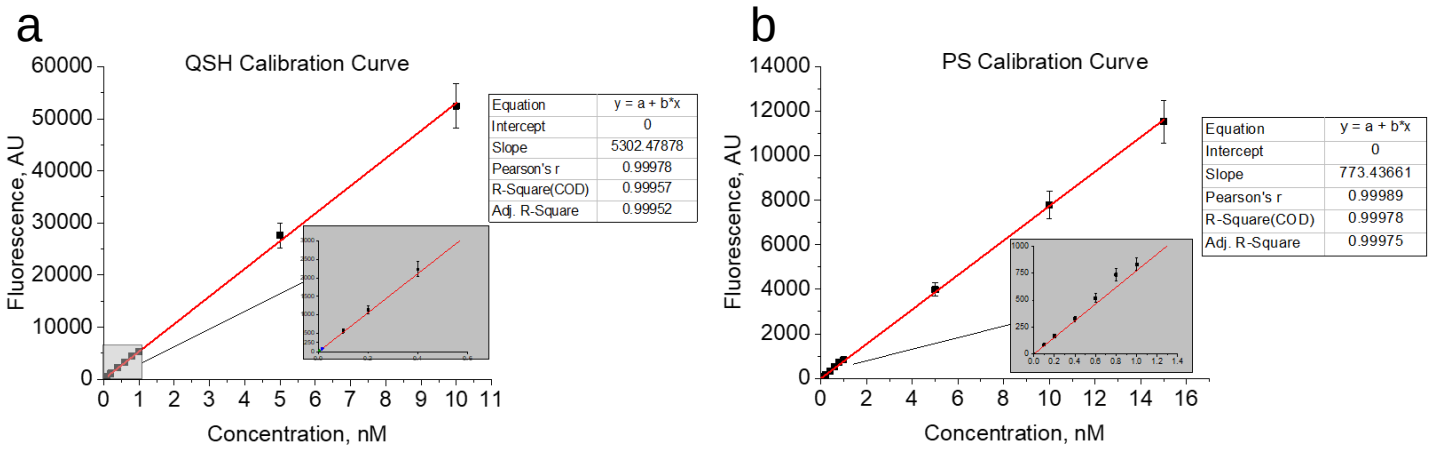

Appendix A3. QSH and PS calibration curves. An 8 point calibration curve was constructed with concentrations of .10, .20, .40, .60, .80, 1, 5, 10, and/or 15nM in complete growth media. The linear dynamic range (LDR, linearity) was noted for concentrations as low as .10nM and as high as 10 or 15nM for QSH and PS. These calibration curves were used to calculate limits of detection and quantitation for both NM types.

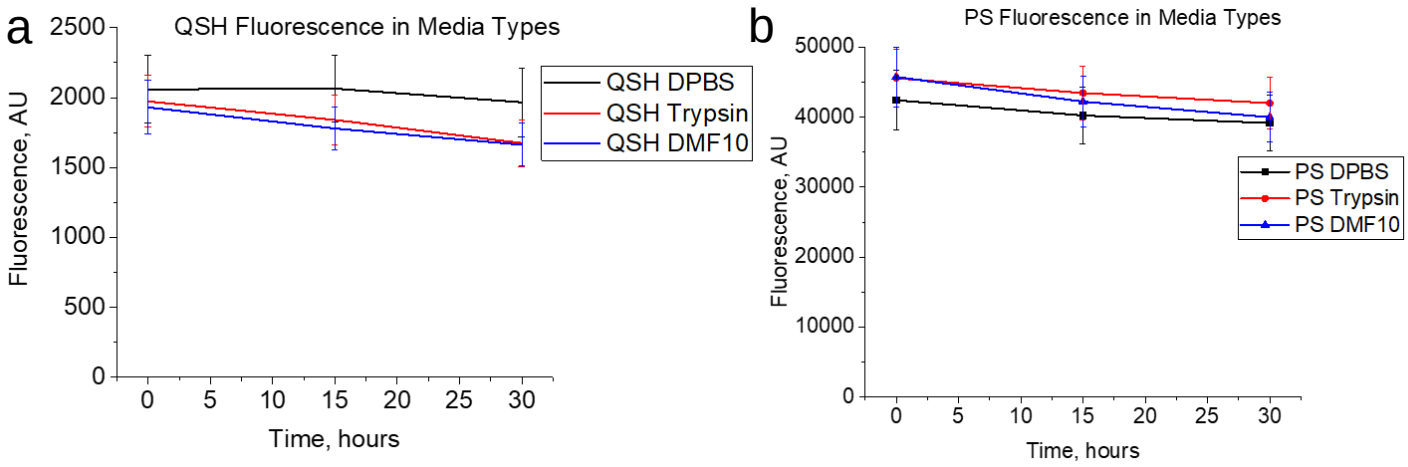

Appendix A4. Media Interference Study. (**a**) Indicates no significant difference between QSH in growth media (red) and trypsin (blue). Slight difference occurs for QSH in DPBS (black) to that in other media types. PS (**b**) showed no significant difference between all media types, and substantial stability in DPBS (black), trypsin (red), and growth media (blue).

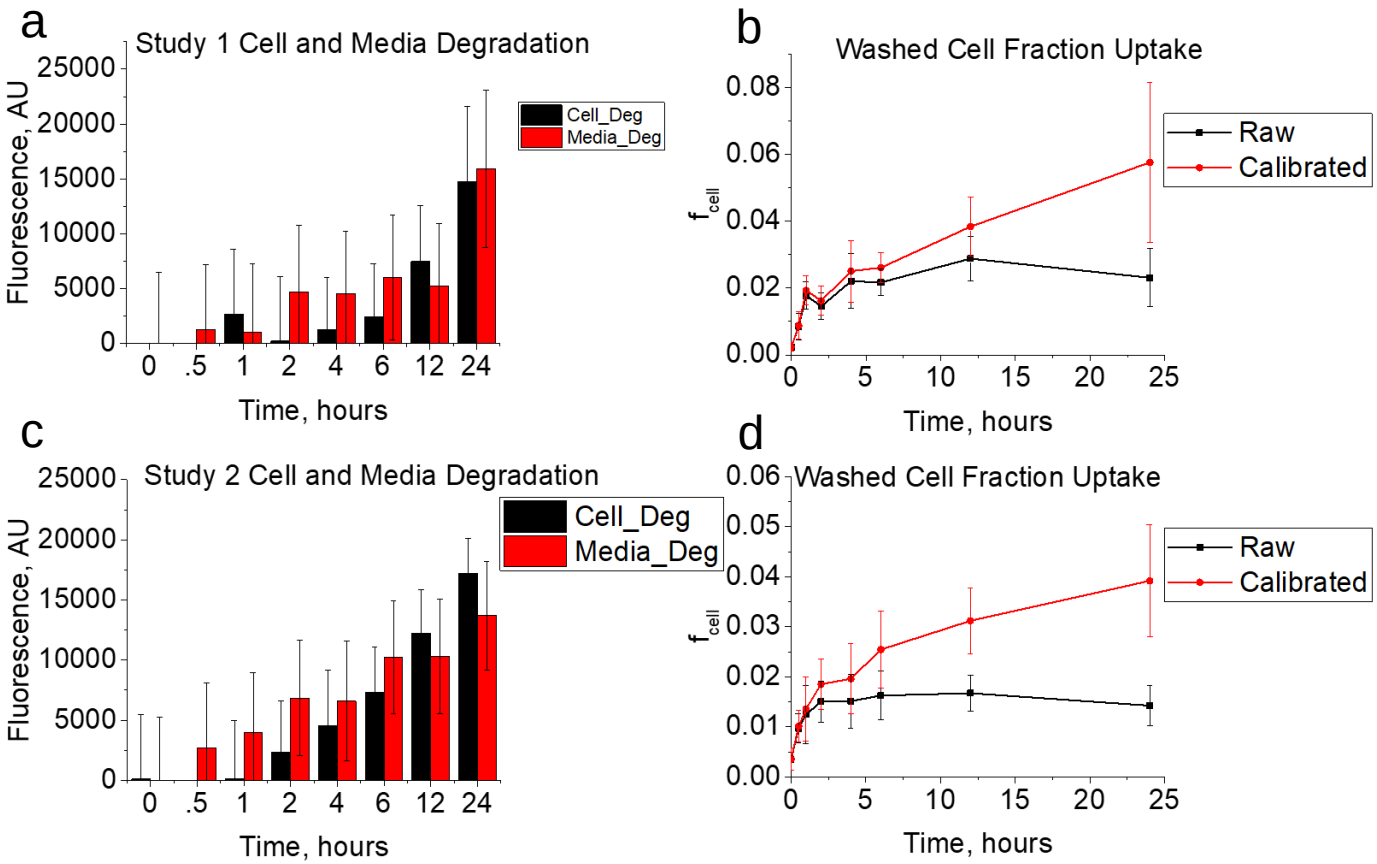

Appendix A5. Study 1 and 2 QSH RCF degradation and fraction of dose experimental data**.** Study 1(**a-b**) and 2 (**c-d**) datasets were formed from results given in Figure 2. (**a,c**) Shows raw fluorescent signatures for degradation for both studies. These values represent differences in fluorescence for CSI_t with MPE_t and MPE_0 with MPE_t for cell and media induce degradation, respectively. (**b,d**) Contain f_{cell} values, obtained from taking the intensities of CKD compartments relative to that of either CSI at time 0 or time t, depending on inclusion of degradation effect. This value was then taken to obtain [Uptake] (nM) QSH concentratios in cells according to equation 1 in main text of paper.

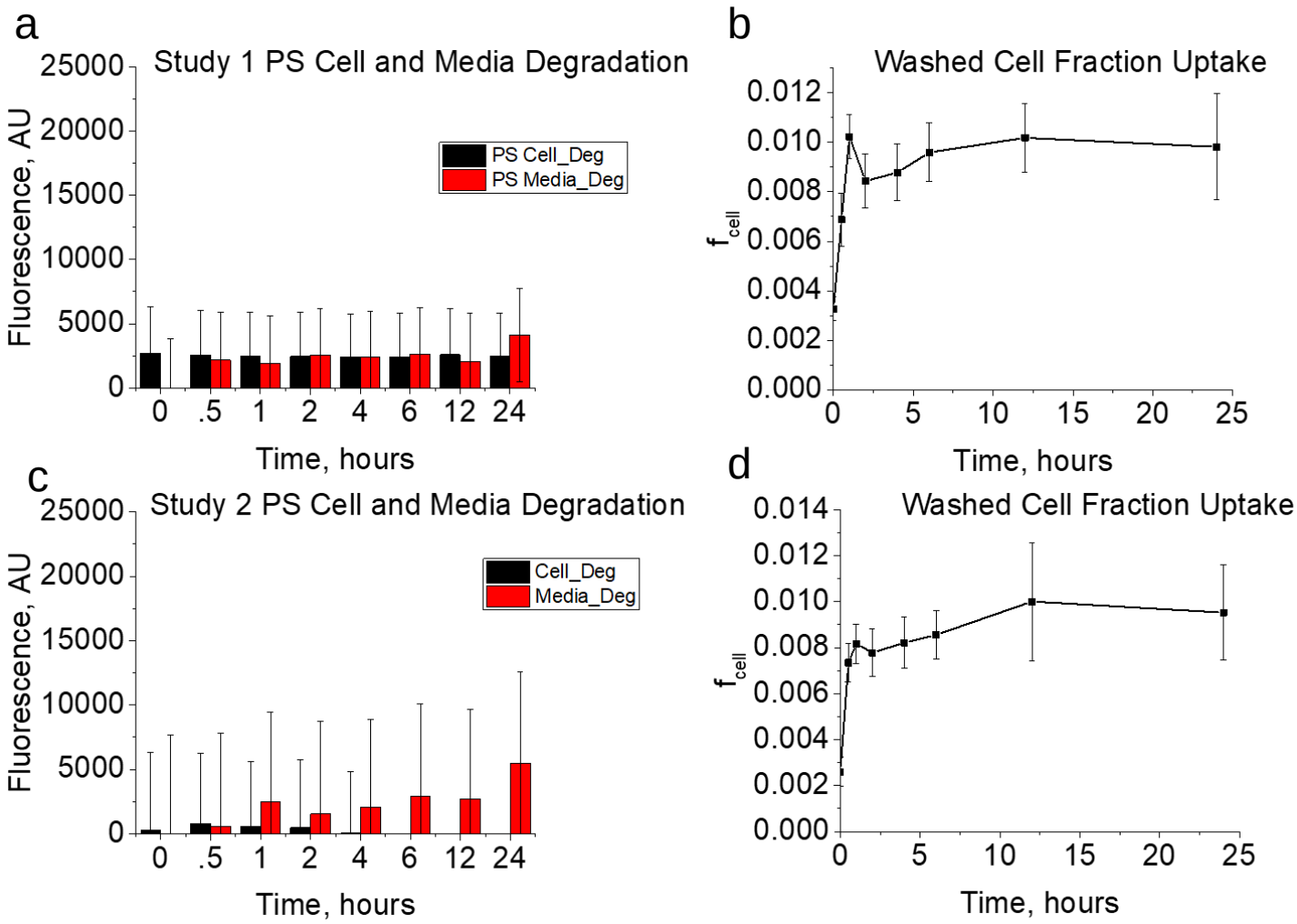

Appendix A6. Study 1 and 2 PS RCF degradation and fraction of dose experimental data**.** Study 1(**a-b**) and 2 (**c-d**) datasets were formed from results given in Figure 2. (**a,c**) Shows raw fluorescent signatures for degradation for both studies. These values represent differences in fluorescence for CSI_t with MPE_t and MPE_0 with MPE_t for cell and media induce degradation,

respectively. (**b,d**) Contain f_{cell} values, obtained from taking the intensities of CKD compartments relative to that of either CSI at time 0 or time t, depending on inclusion of degradation effect. This value was then taken to obtain [Uptake] (nM) PS concentratios in cells according to equation 1 in main text of paper.

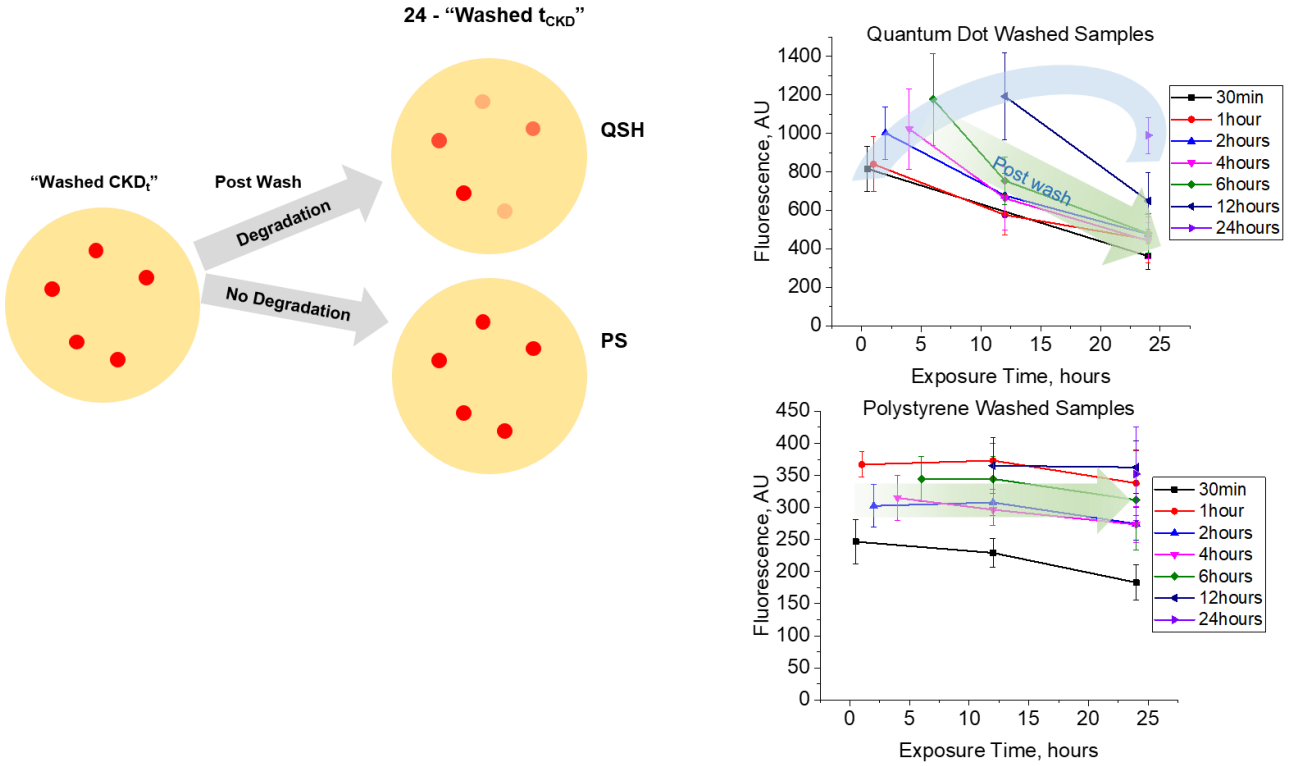

Appendix A7. Prolonged incubation of QSH and PS post-wash at time t. Here (**left**), a sample was washed at t hours and left inside incubator to determine if prolonged exposure to cellular conditions would degrade fluorescent signal over time. Quantum dot QSH, **top right**, shows significant loss in fluorescence signal after prolonged exposure to cellular environment. Polystyrene PS, **bottom right**, shows a steady maintenance of signal upon exposure to cellular environment hinting at limited to no fluorescence sensitivity to intracellular environment.

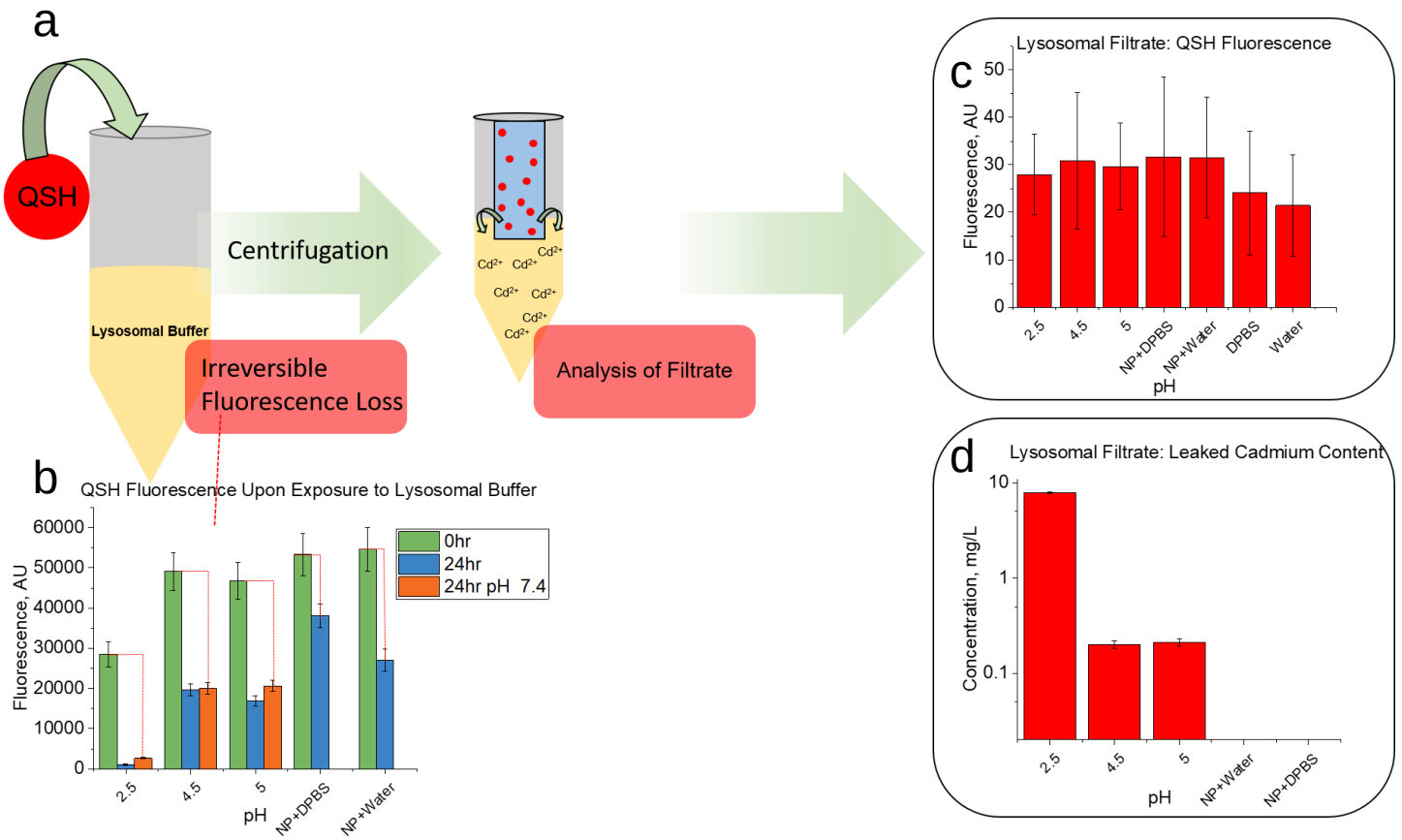

Appendix A8. Simulated lysosomal buffer QSH degradation experiment. (**a**) Schematic of process of exposure of 10nM QSH to lysosomal buffer and further purification and analysis. (**b**) Complete analysis of fluorescence signal after 0 and 24 hours of exposure. For QSH in low pH there was instant decrease in fluorescence with substantial fluorescence loss after 24 hours for all pH environments. All solutions were increased back to physiological pH of 7.4 with limited to no increase in fluorescence, which infers irreversible loss of fluorescence signal. (**c**) Filtrate analysis of all solutions show no significant QSH fluorescence

in filtrate after centrifugation, indicative of limited to no intact QSH in filtrate. (**d**) However, significant cadmium content appears in lysosomal buffers, of pH 2.5, 4.5, and 5.0. No detectable free cadmium was analyzed in filtrate with QSH exposure to DPBS and/or water.

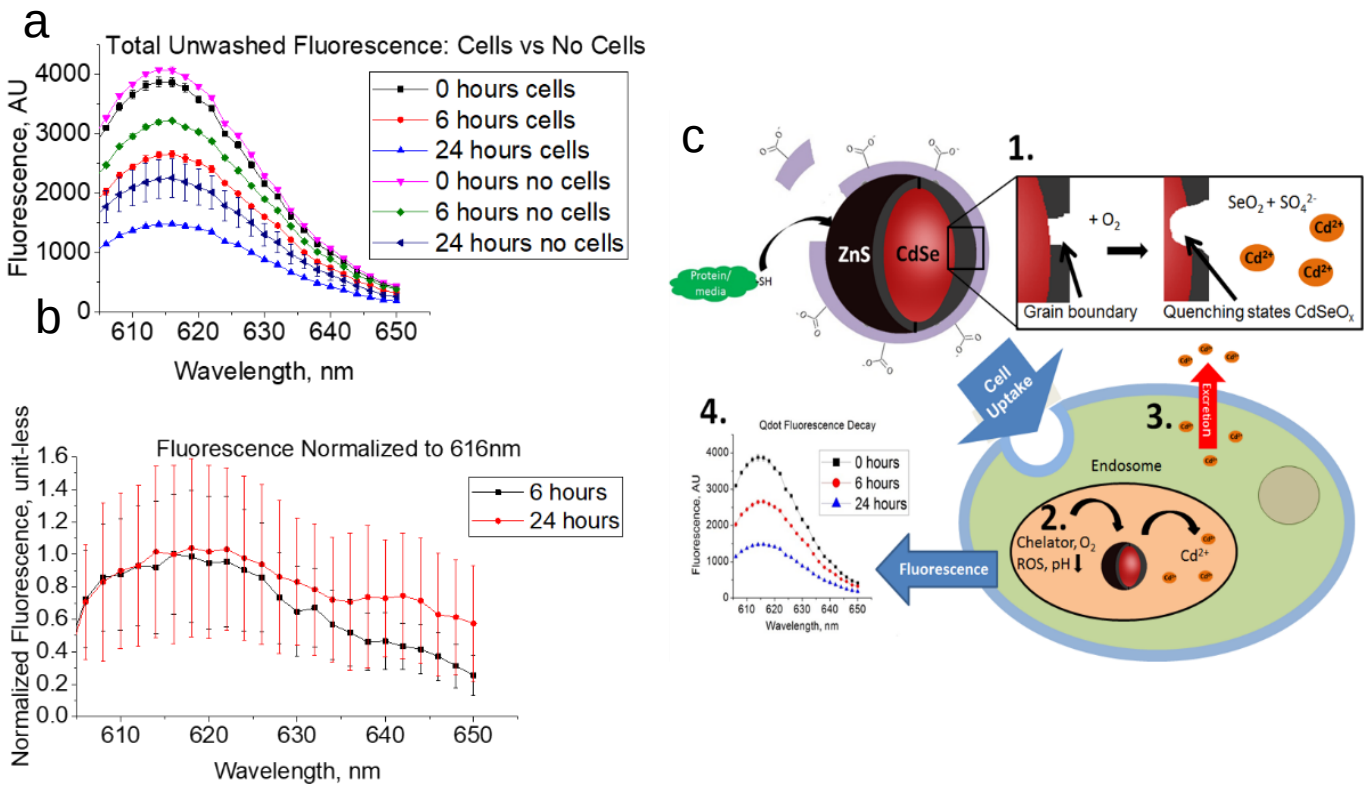

Appendix A9. Analysis of cell-induced fluorescence degradation upon exposure to cellular environment. (**a**) Full spectral analysis of unwashed wells with and without cell exposure for QSH. Washed cell fluorescence (**b**) normalized for 6 and 24 hours shows spectral broadening due to cell-induced degradation. Here, broadening shows an increase from 6 to 24 hours. (**c**) Diagram of potential mechanisms of cell-induced degradation through lysosomal sequestration with **1** surface degradation,

2 lysosomal sequestration, **3** possible cadmium leakage, and **4** fluorescence loss due to decreased pH and chelator exposure.

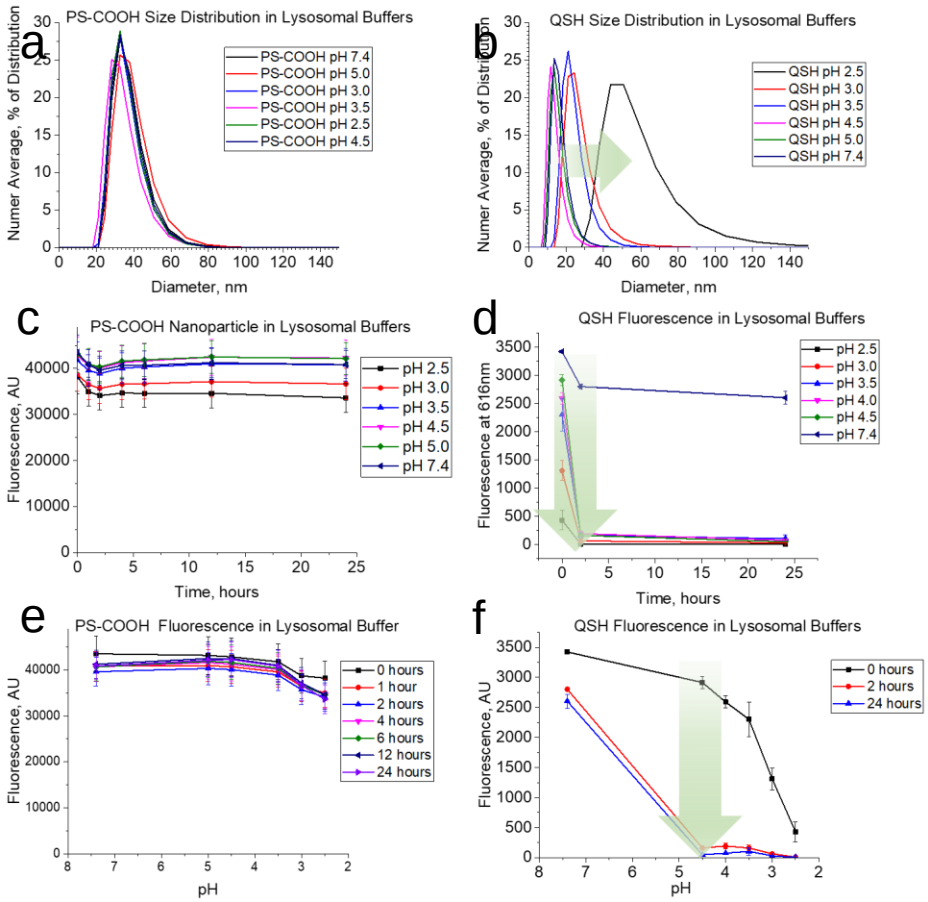

Appendix A10. Physicochemical characterization after exposure to lysosomal conditions. Complete DLS size analysis for (**a**) QSH and (**b**) PS indicate agglomeration for lower pH values for QSH and stability for PS. (**c**) Shows significant stability for PS fluorescence at 595nm emission for all time points and pHs. (**d**) Shows instability for QSH signal at 620nm emission at all time points for all pHs except physiological 7.4. (**e**) Shows pH-dependent stability for PS and (**f**) shows QSH pH-dependent instability for all pHs and time-points.

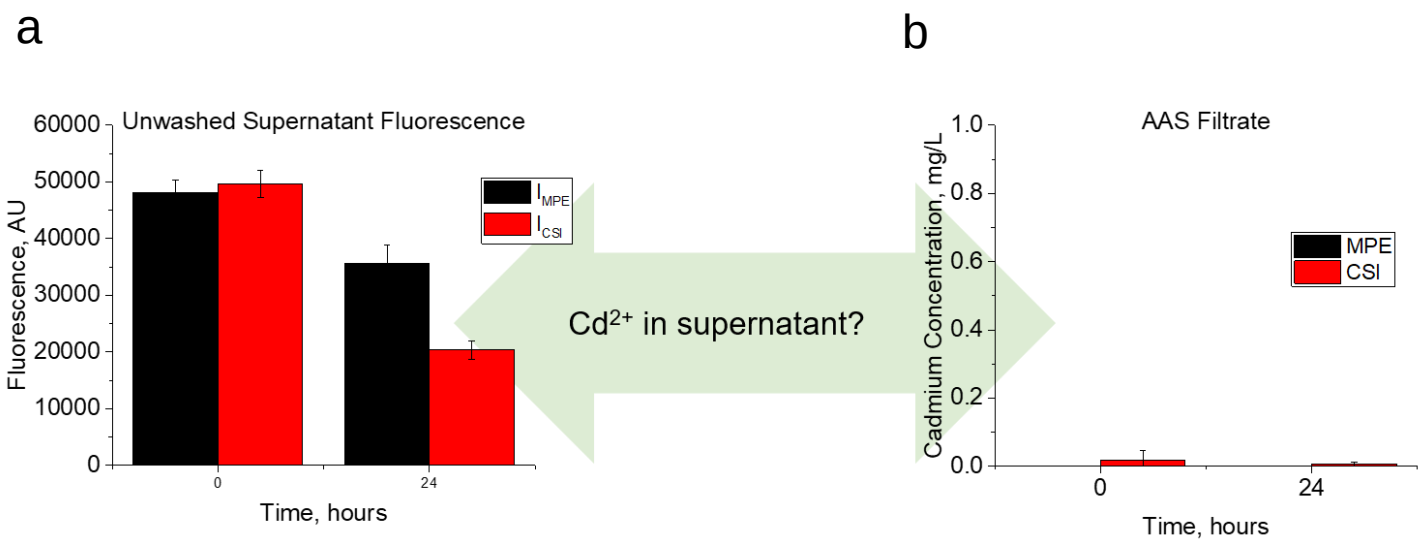

Appendix A11. Supernatant filtrate analysis for free cadmium detection from cell-induced degradation of QSH. (**a**) Indicates minimal cell-induced degradation at 0 hours and significant ($P<0.05$) cell-induced degradation for 24 hours. To determine if free cadmium is present outside the cells, samples (supernatant) were centrifuged and filtrate was analyzed for cadmium content in (**b**). Here, no significant cadmium content was detected.

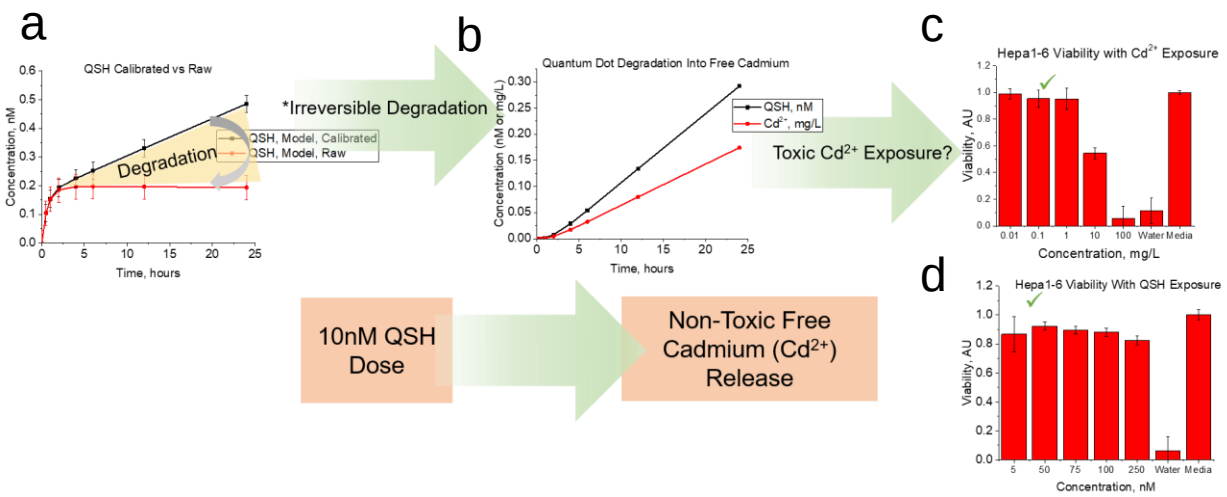

Appendix A12. Model output with QSH degraded alongside Cd^{2+} formation. (**a**) Shows model fit to calibrated datasets (black) and raw datasets (red). The difference in concentrations between datasets is described via degradation rate constant, k_{deg}, and provides additional information on concentration of degraded QSH (**b**, black) and subsequent free cadmium (Cd^{2+}) (**b**, red). The concentration of Cd^{2+} from the degraded QSH core are not high enough to induce toxicity, as shown in (**c**) for $Cd(NO_3)_2$ exposure studies on Hepa1-6 cell line for concentrations ranging from .01-100mg/L Cd^{2+} for 24 hours. No significant toxicity is apparent for doses less than 10mg/L. As for QSH, no toxicity is also noted for doses used in this study (**d**).

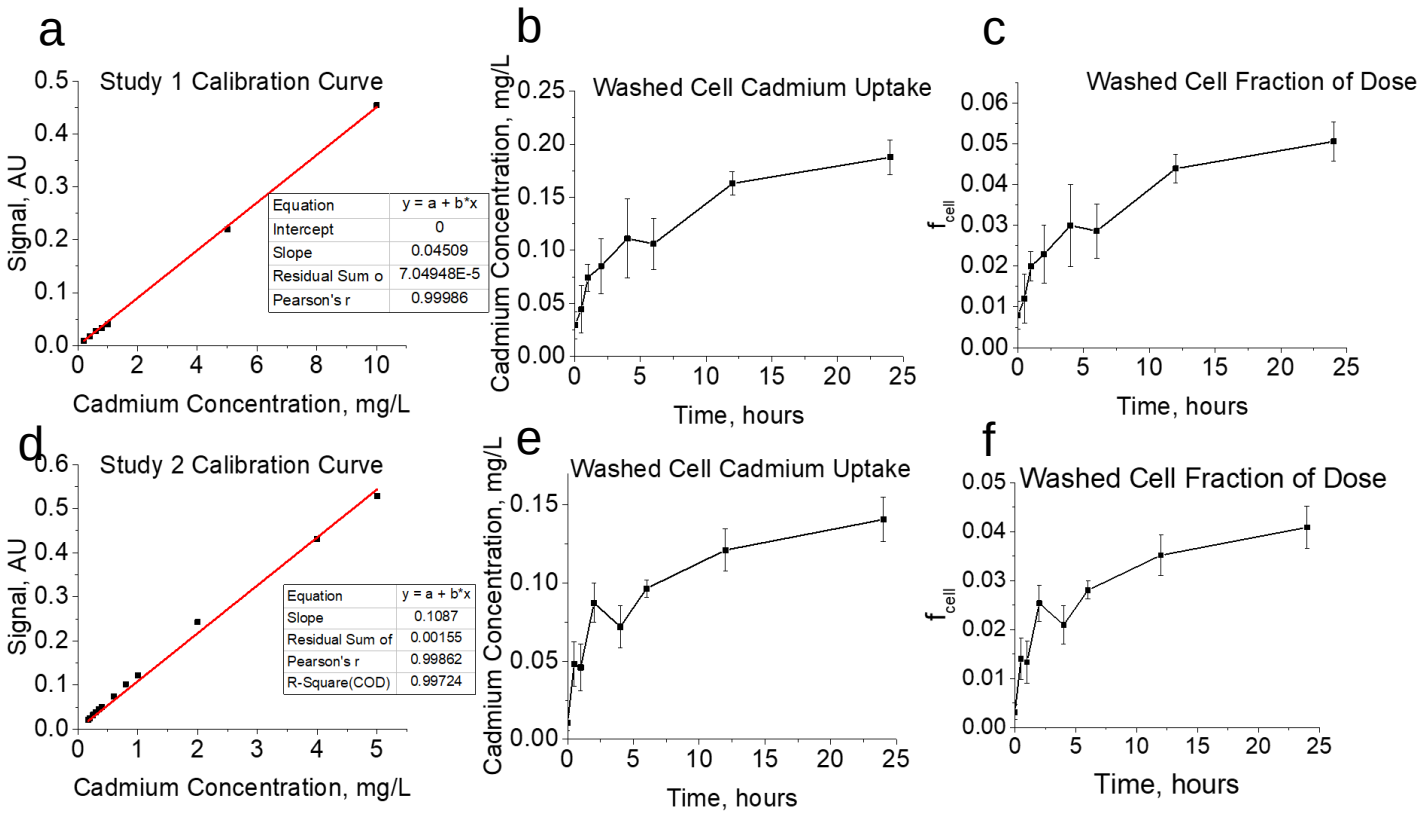

Appendix A13. Merged Study 1 and 2 AAS Results. Study 1(**a-c**) and Study 2 (**d-f**) were run separetly approximately one (1) month apart. (**a,d**) Contain calibration curves used to interpolate cadmium concentration for washed cell samples taken from the CKD compartment.(**b,e**) Show washed cell cadmium content obtained from CKD compartments, in mg/L over the time of their respective studies. These values were then divided by the total CSI to (**c,f**) to obtain a fractional uptake in cells.

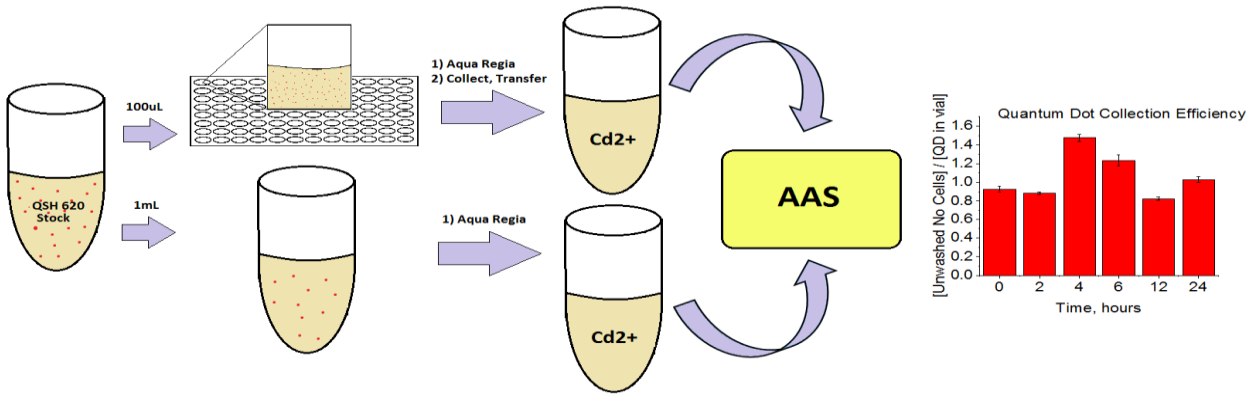

Appendix A14. Collection efficiency experiment was performed to ensure full extraction of dissolved cadmium in wells. In one case, a triplicate of wells exposed to 10nM QD from the MPE compartment was dissolved in 1/3% v/v aqua regia, while in the other, 10nM QSH was dissolved a vial with 1/3% v/v aqua regia. Both scenarios were then transferred to vials for AAS analysis.and measured for cadmium content. The ratio of MPE_t to vials were taken, as the plots indicate [Unwashed No Cells] / [QD in vial].. No significant trends in data were noted, and values ratios remained approximately equal to 1, which indicates diluted vials and collected wells were similar in cadmium content.

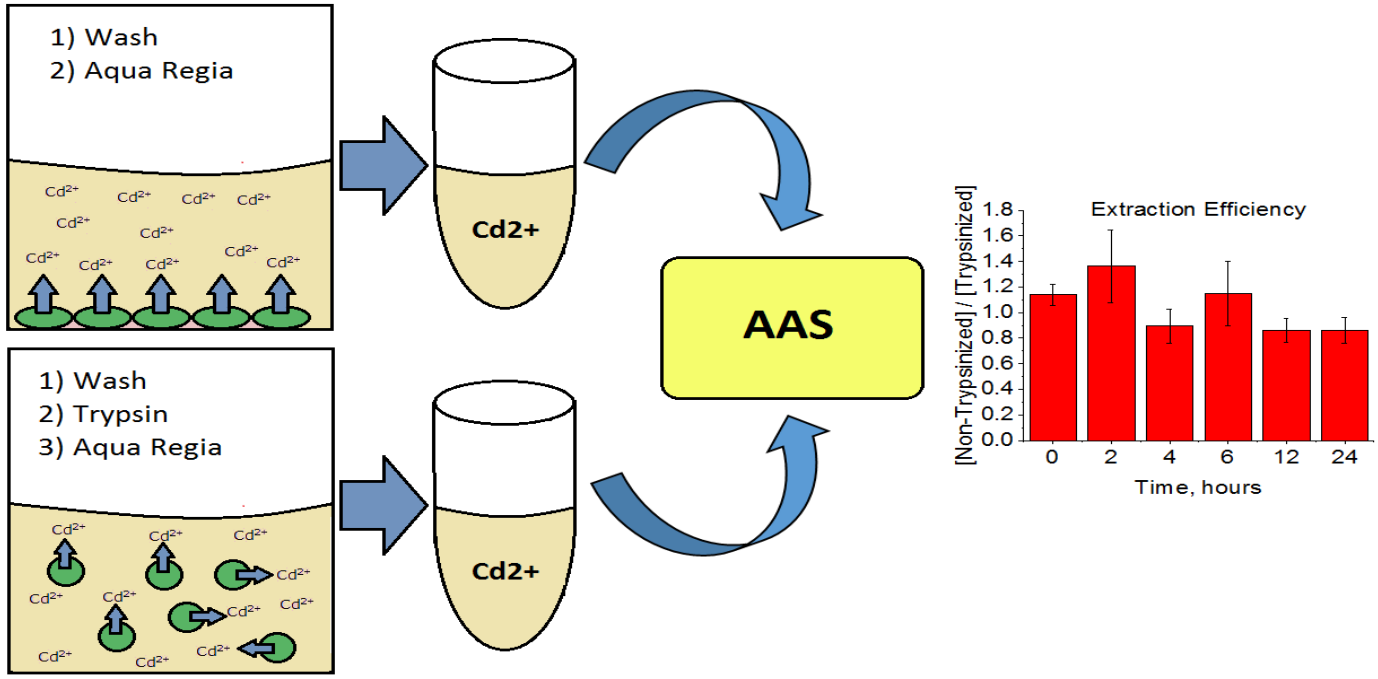

Appendix A15. Extraction efficiency for washed well cadmium content. 2X washed cells from CKD_t exposed to trypsin or no trypsin with the 10nM QSH dose were all exposed to 1/3 v/v% aqua regia for 10 minutes and transferred to vials for AAS analysis. The ratio of CKD Cd content of non-trypsinized to trypsinized was close to 1, indicative of full cadmium extraction from cell interior.

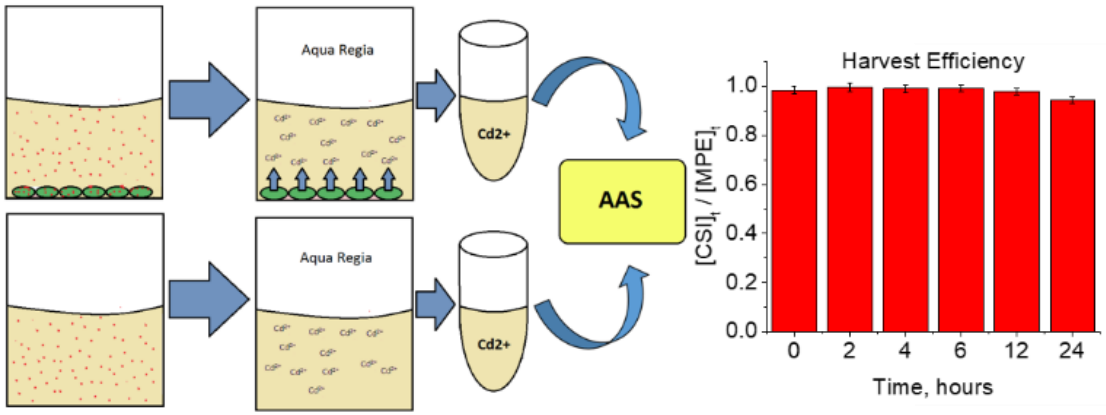

Appendix A16. Harvest efficiency above describes the potential to harvest QSH from the total well when there are cells present. Wells exposed to equal doses of QSH with and without cells (unwashed) were given equal doses of 1/3 v/v% aqua regia for 10 minutes. AAS was performed and the ratio of unwashed cells to no cells is approximately 1, indicative of full cadmium extraction, as well as minimal cellular matrix interference on the AAS instrument.

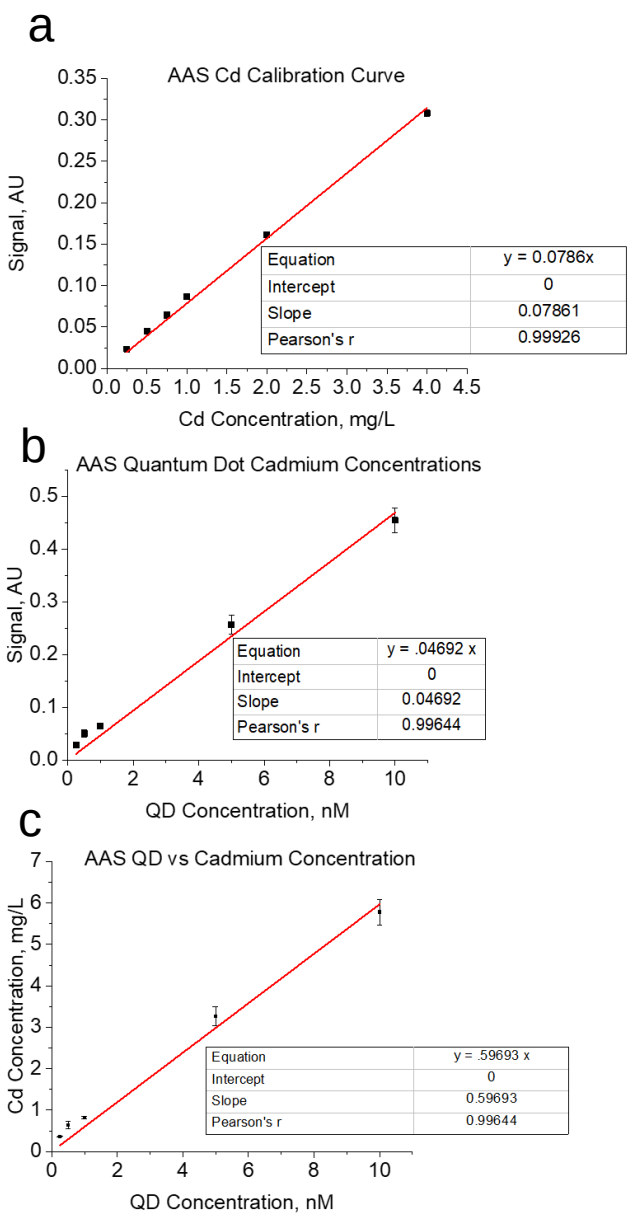

Appendix A17. AAS Calibration curve for LOD and LOQ quantitation and QD Correlation. **(a)** Cadmium concentrations showing linearity from .25 to 4.0mg/L cadmium. (**b**) Digested QSH ranging from .25 to 10nM QSH concentrations with respective signal show linearity for all concentrations shown. Slopes from (**a**) and (**b**) were used to determine correlations between QSH and cadmium concentrations (**c**) for further comparison to RCF datasets.

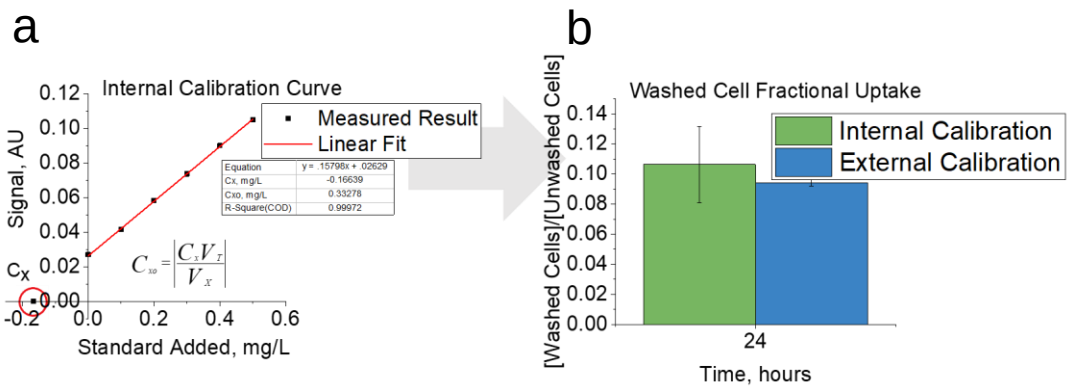

Appendix A18. Standard additions technique compared to conventional external calibration method. Comprehensive check on cell matrix interference on AAS signal was performed using an internal calibration curve (**a**) where a 24 hour sample was spiked with increasing concentrations of $Cd(NO_3)_2$ stock. The output (internal calibration) from (**a**) was compared to conventional 6-point external calibration curve data in (**b**) No significant difference exists between the two techniques, indicating limited to no cell matrix interference

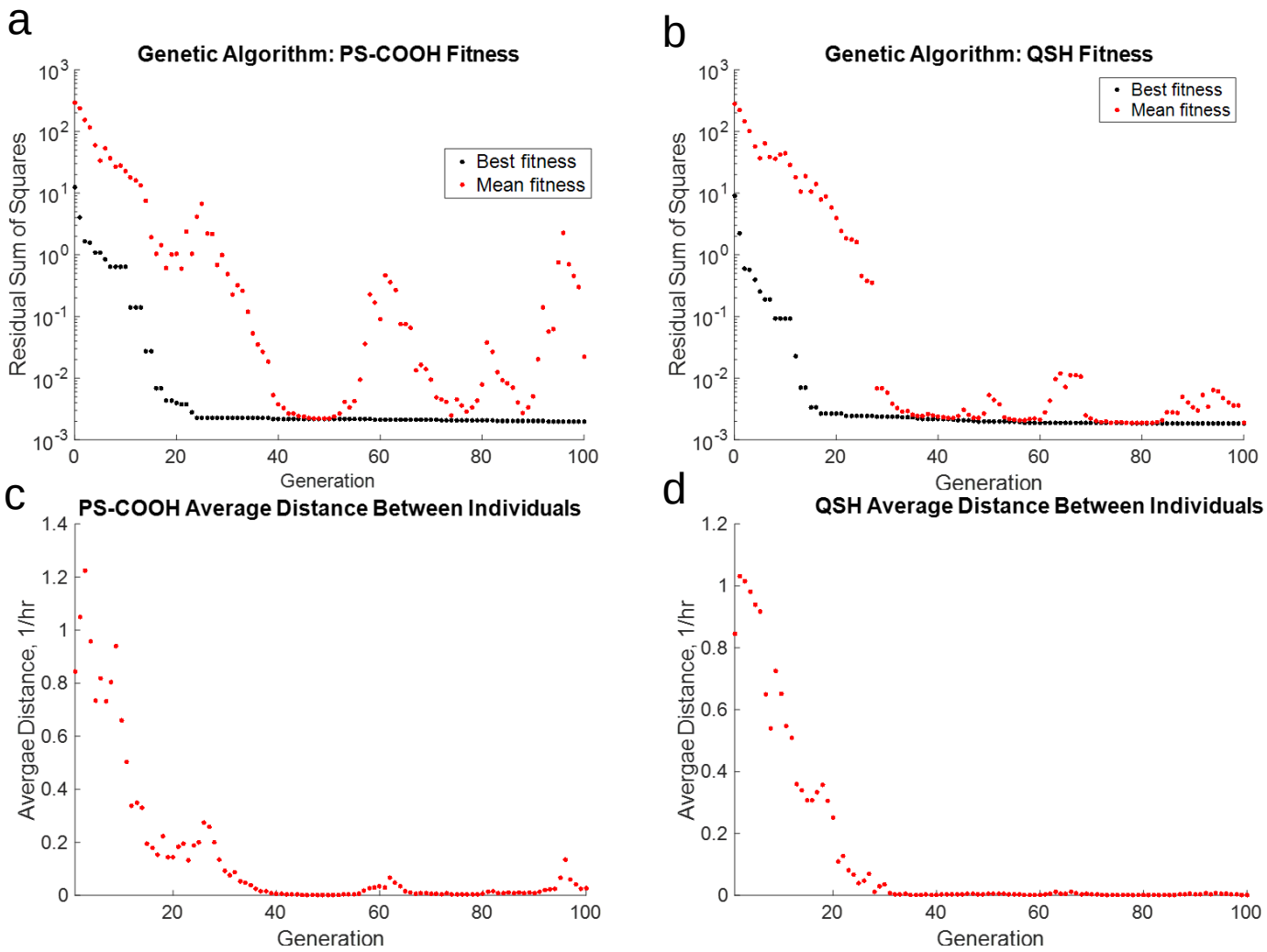

Appendix A19. Genetic algorithm output for each generation of optimization process. (**a, b**) show the fitness function (residual sum of squares) at each generation for (**a**) PS and (**b**) QSH. (**a**) shows model convergence to optimal solution of k values at approximately 25 generations (best fitness). (**b**) shows model convergence to optimal solution of k values at approximately 20 generations for QSH. Model search for additional best fit is represented by fluctuations in mean fitness

(**a,b**) of population for a given generation (red, peaks). (**c, d**) show average distance between vectors of a population of 50 individuals at a given generation. As the simulation converges, the distance between vectors decreases.

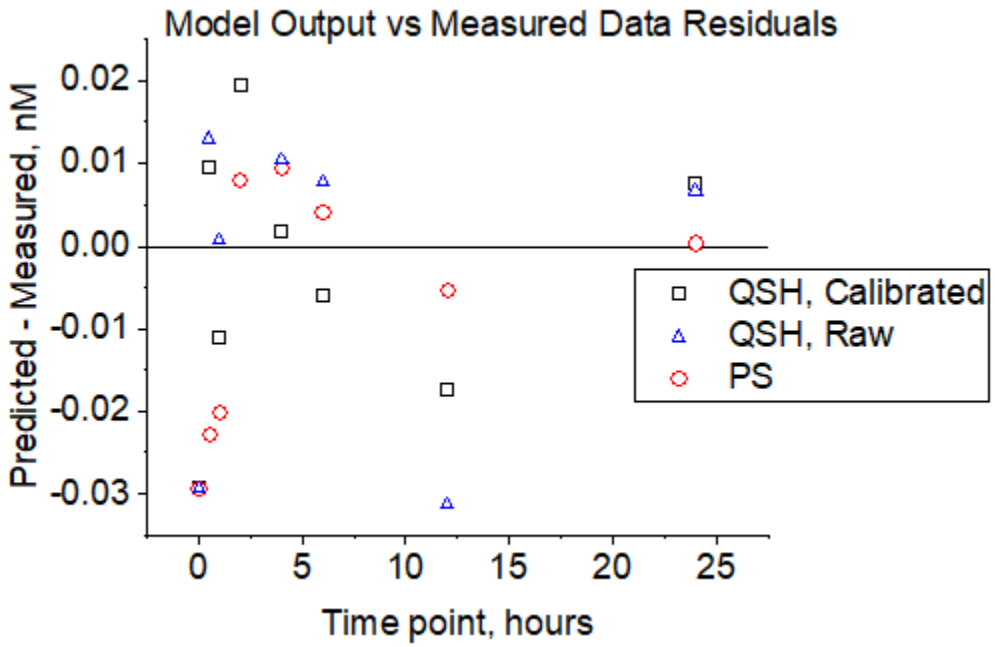

Appendix A20. Model output residuals for QSH raw and calibrated as well as PS data. Detailed residual analysis is shown for each model output difference to a particular measured concentration at time t. The apparent randomly distributed residuals around 0, indicate decent model fit to measured data.

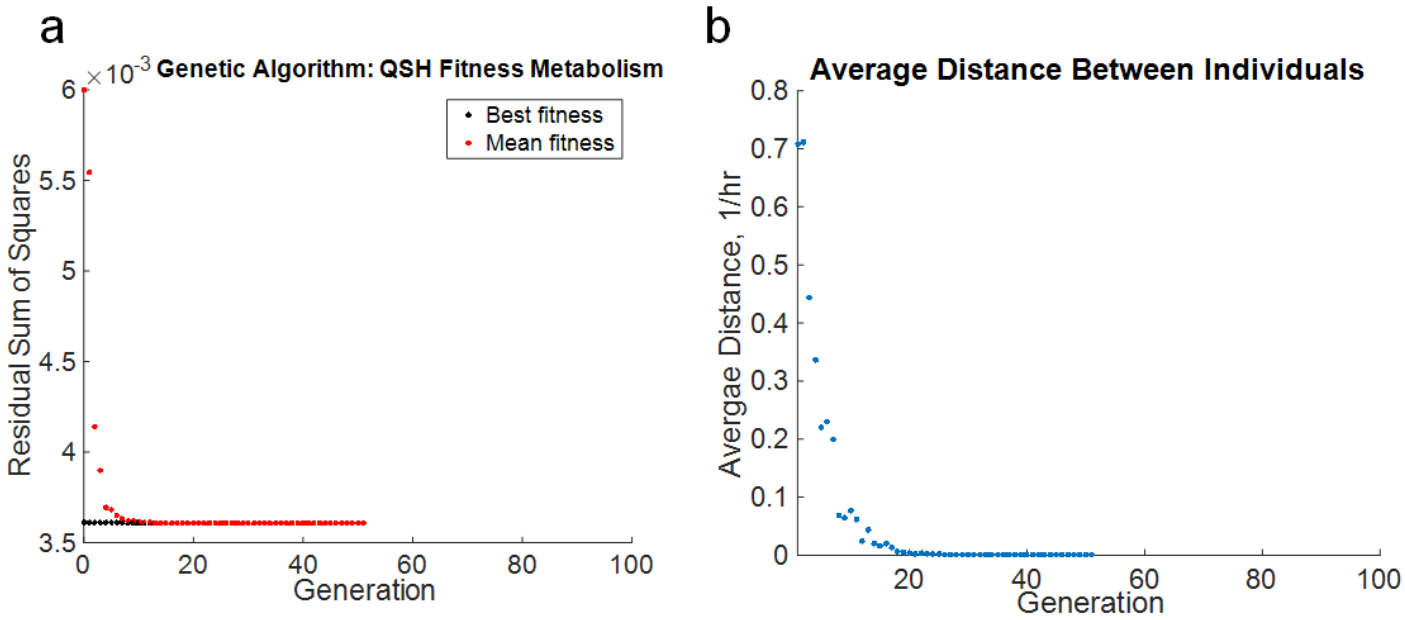

Appendix A21. Genetic algorithm output for each generation. (**a**) Shows the fitness function (residual sum of squares) at each generation for model fit to raw QSH data. (**a**) Shows model convergence to optimal solution of k values at approximately 10 generations (best fitness). (**b**) Shows average distance between vectors of a population of 50 individuals at a given generation. As the simulation converges, the distance between vectors decreases.

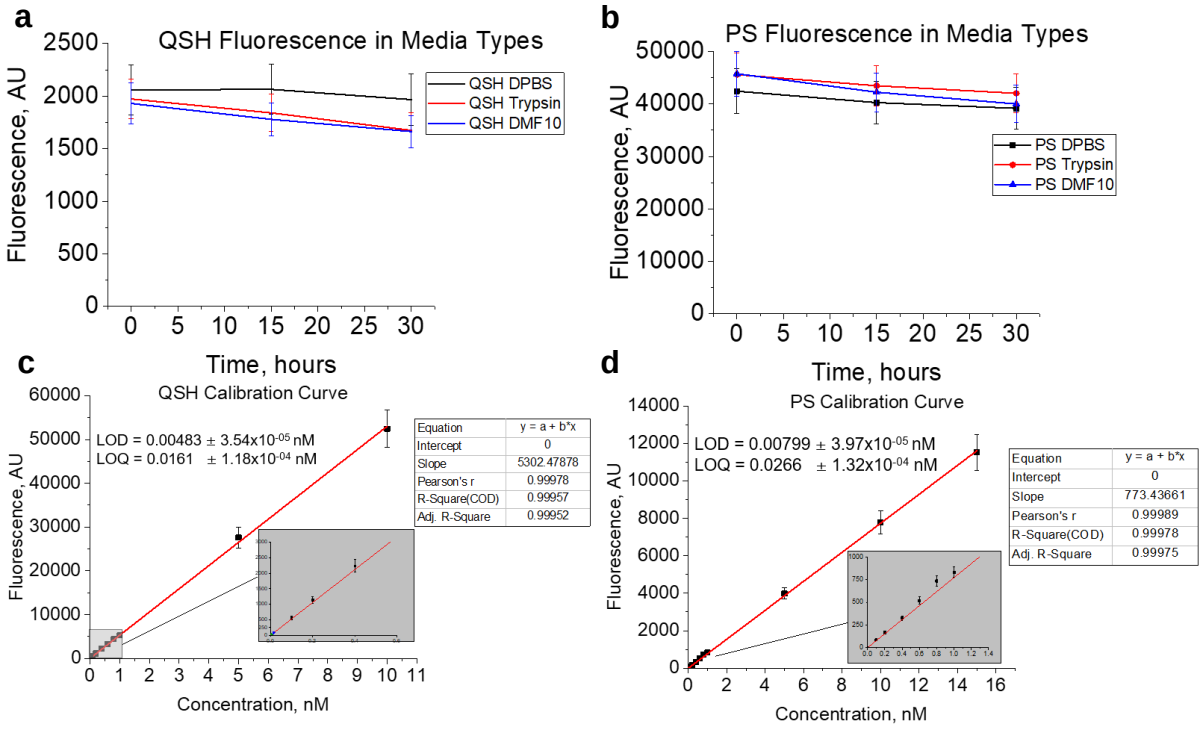

Appendix A22. Quality assurance on fluorescence signal obtained from NMs in biological solutions. a,b, Fluorescence signal for prolonged periods of time under exposure to complete growth media (DMF10), DPBS, and trypsin for (**a**) QSH and (**b**) PS. **c,d,** Calibration curves used to determine the limits of detection (LOD) and quantiation (LOQ) for (**c**) QSH and (**d**) PS.

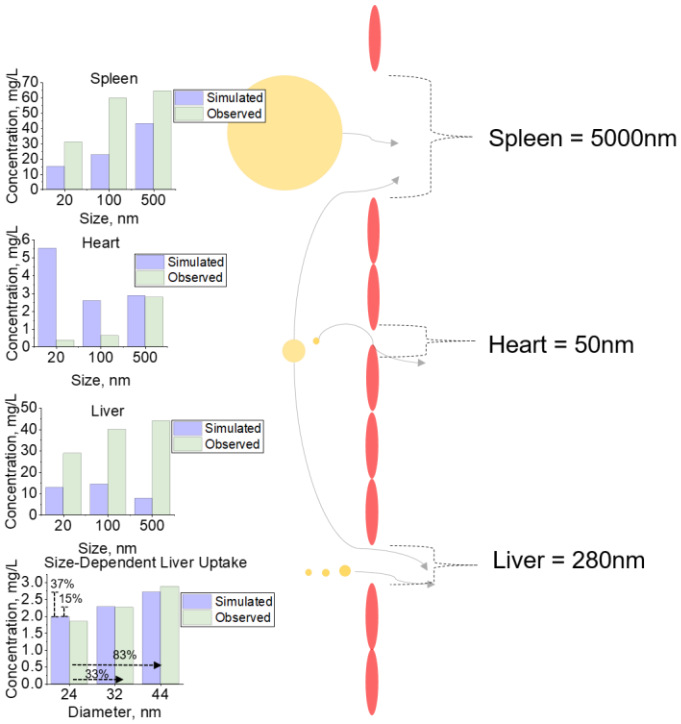

Appendix A23. Cellular analysis of NM uptake in varying tissues for NM with different diameters. a-c, Cellular uptake of NMs with diameters of 20, 100, and 500nm for spleen, heart, and liver with fenestrae diameters of 5000, 50, and 280nm respectively. Sensitivity analysis of incremental changes in NM diameter (24, 32, and 44nm) with subsequent liver cell uptake were performed. All simulated (predicted) outputs are compared to observed data from literature cellular datasets.

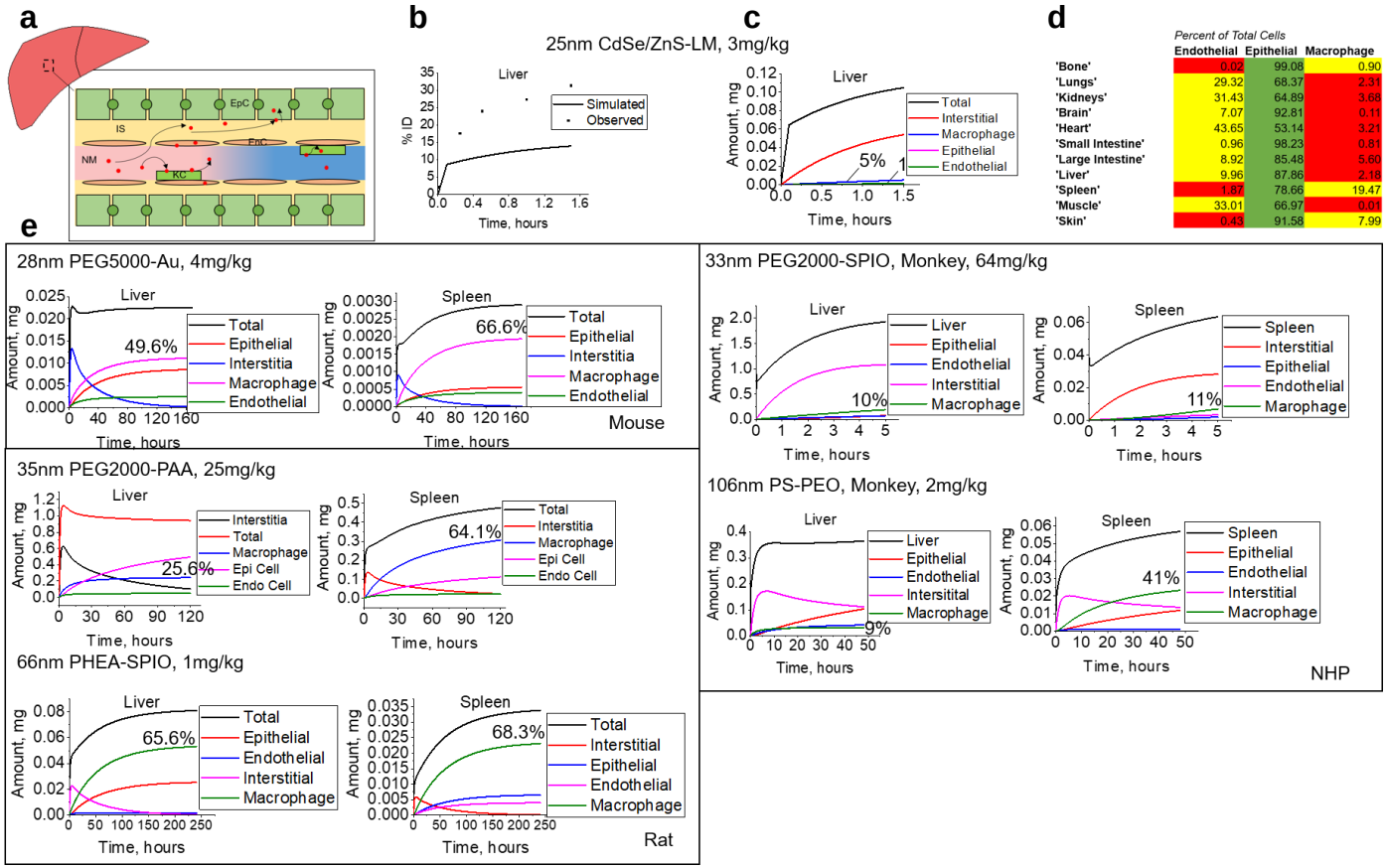

Appendix A24. Liver and spleen total and cellular uptake of NM for multiple species and NM types. a, Schematic of liver cellular composition which consists of endothelial (EnC), epithelial (EpC), and macrophage (KC) cellular content. The NM from the vasculature must travel through the EnC fenestrae to reach the interstitial space (IS). **b, c,** Total liver uptake (**b**) and cellular content (**c**) in rat liver tissue. **d,** All tissue cellular content for tissues used in this study. **e** NM uptake in spleen and liver epithelial and endothelial cells, macrophages, and interstitia for Mouse, NHP, and Rats.

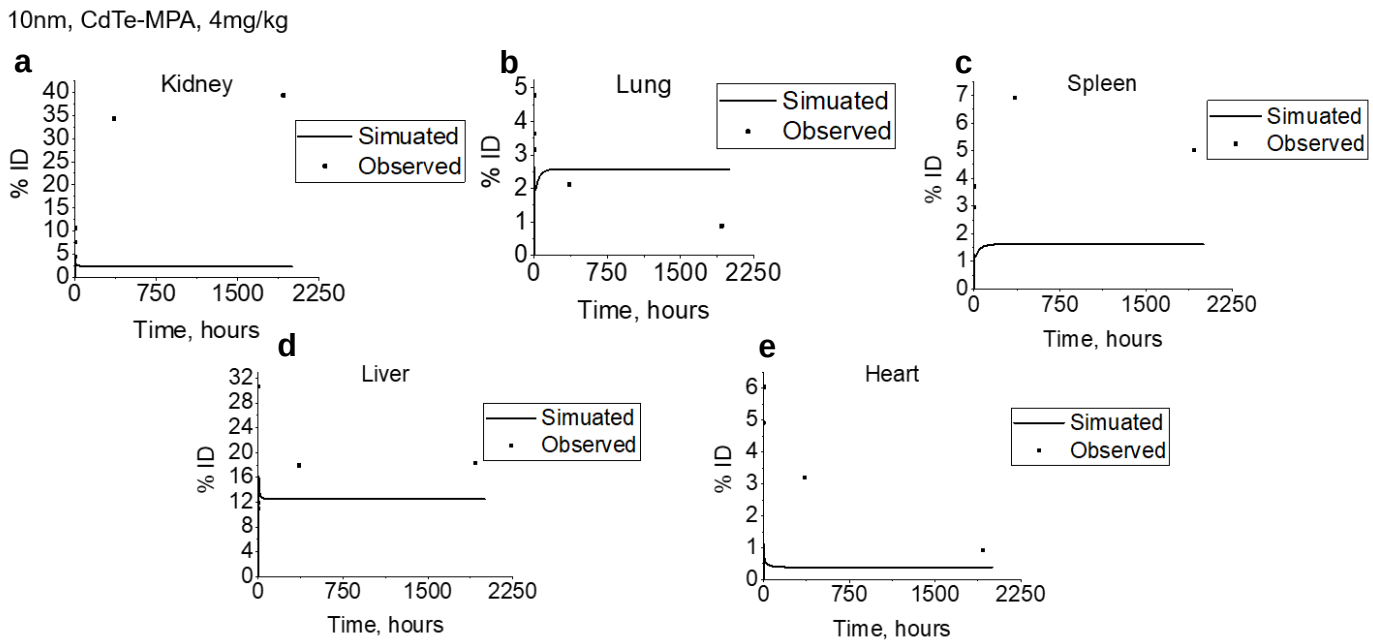

Appendix A25. Total tissue content for mouse intravenous dosing studies. a-e, Total percent of intravenous dose predicted by our group and reported in published live animal studies for (**a**) Kidney, (**b**), Lungs, (**c**) Spleen, (**d**) Liver, and (**e**) Heart tissue.

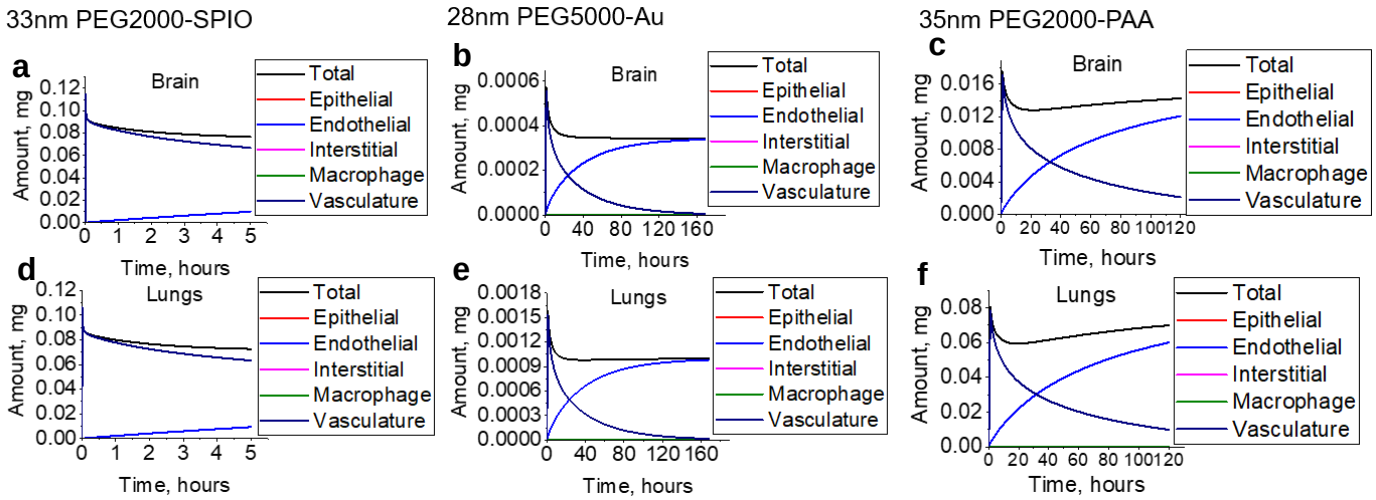

Appendix A26. Brain and lung NM sub-tissue content. a-c, Brain sub-tissue content for (**a**) 33nm PEG2000-SPIO, (**b**) 28nm PEG5000-Au, and (**c**) 35nm PEG2000-PAA. **d-f,** Lung sub-tissue content for (**d**) 33nm PEG200-SPIO, (**e**) 28nm PEG5000-Au, and (**f**) 35nm PEG2000-PAA.

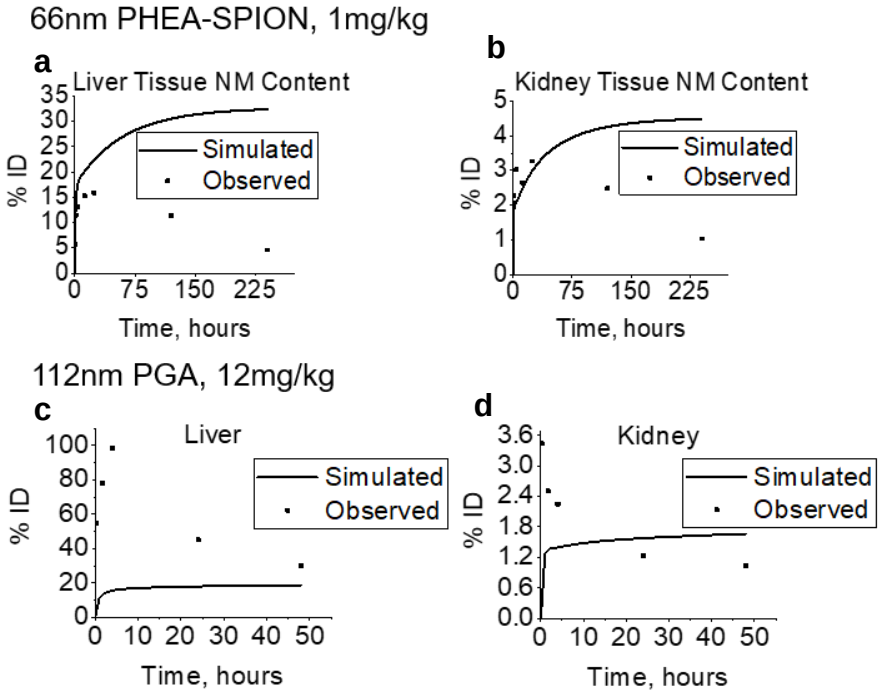

Appendix A27. Analysis of tissues involved in NM metabolism. a-d, Liver and Kidney tissue uptake for (**a,b**) Heavily metabolized 66nm PHEA-SPION and (**c,d**) Minimally metabolized112nm PGA NM.

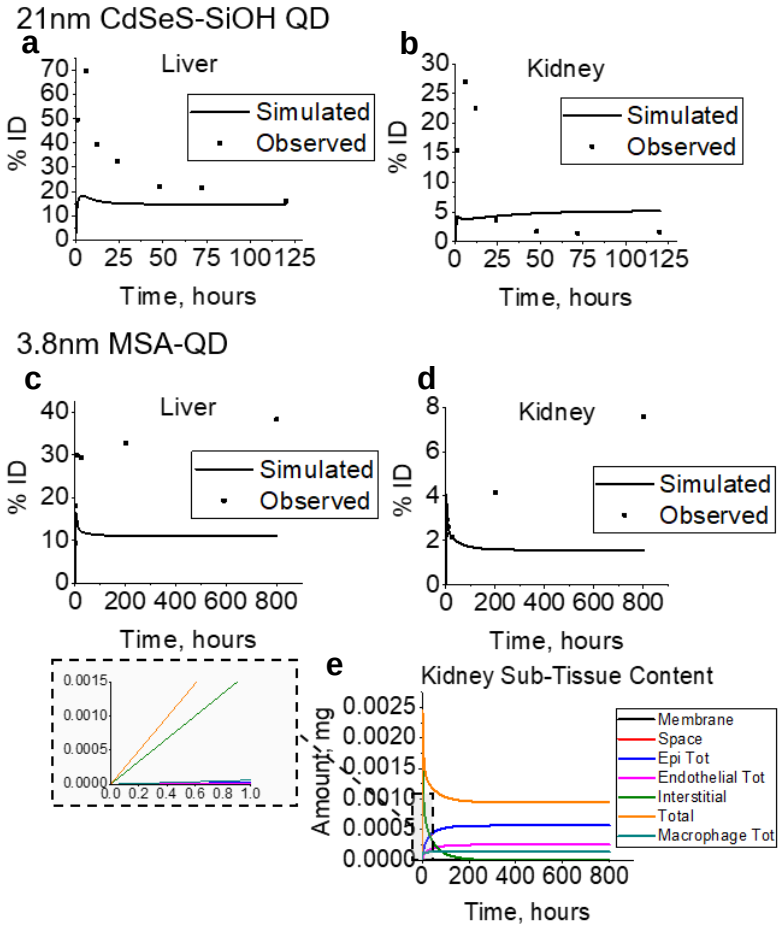

Appendix A28. Liver and kidney total NM content for 21 and 3.8nm-sized QDs. a-d, Total tissue level NM content for liver and kidney for (**a,b**) 21nm CdSeS-SiOH QD and (**c,d**) 3.8nm MSA-QD. **e,** Cellular and interstitial analysis of the smaller, 3.8nm-sized QD inside kidney tissue.

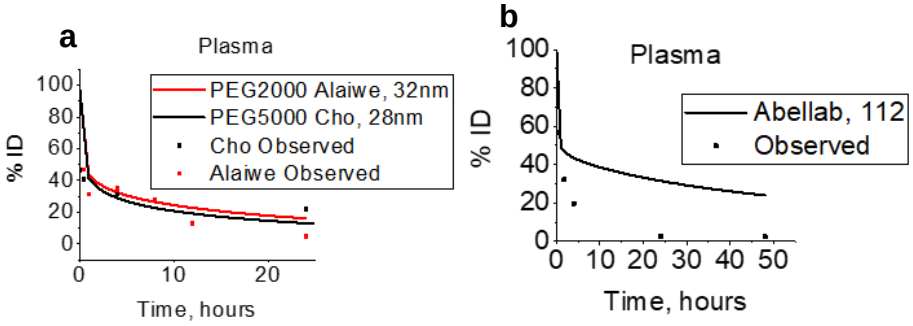

Appendix A29. Plasma NM content and correlation PEG chain length as well as liver and spleen. a, Plasma uptake data for NMs of varying PEG chain lengths. **b,** Plasma uptake data for NM exhibiting substantial excretion profile.

APPENDIX B: SUPPLEMENTARY TABLES

Table B1. Quantum Dot and Polystyrene Limits of Detection and Quantitation

Sample ID	LOD, nM	StDev	LOQ, nM	StDev
QSH	0.004833968	3.54583E-05	0.016113226	0.000118194
PS	0.007989205	3.97261E-05	0.026630684	0.00013242

Table B2. LOD and LOQ Values for PerkinElmer Flame AAS

Cadmium LOD and LOQ Values ± Standard Deviation	
LOD (mg/L)	0.0207 ± 0.000284
LOQ (mg/L)	0.0691 ± 0.000950

Table B3. Model Output Statistics to Measured Datasets

Simulation Type	R	P-value	R Square	Std. Error, nM	Residual Sum of Squares, nM
QSH Model Ratiometric Calibrated	0.9944	0.0000	0.9889	0.0152	0.0019
PS Model	0.9380	0.0006	0.8798	0.0158	0.0020
QSH Model Raw	0.9471	0.0004	0.8969	0.0212	0.0036

REFERENCES

1. Ventola, C. L., Progress in Nanomedicine: Approved and Investigational Nanodrugs. *P & T : a peer-reviewed journal for formulary management* **2017,** *42* (12), 742-755.

2. Rudramurthy, G. R.; Swamy, M. K., Potential applications of engineered nanoparticles in medicine and biology: an update. *Journal of biological inorganic chemistry : JBIC : a publication of the Society of Biological Inorganic Chemistry* **2018**.

3. Business Wire Inc. Maturing Nanotechnology Market Report 2017: Focusing on Applications, Products, Growth Drivers, Restraints & Opportunities - Research and Markets

[Online], 2017. bwh.

4. Eifler, A. C.; Thaxton, C. S., Nanoparticle therapeutics: FDA approval, clinical trials, regulatory pathways, and case study. *Methods in molecular biology* **2011,** *726*, 325-38.

5. Frohlich, E.; Roblegg, E., Oral uptake of nanoparticles: human relevance and the role of in vitro systems. *Archives of toxicology* **2016,** *90* (10), 2297-314.

6. Bobo, D.; Robinson, K. J.; Islam, J.; Thurecht, K. J.; Corrie, S. R., Nanoparticle-Based Medicines: A Review of FDA-Approved Materials and Clinical Trials to Date. *Pharm Res* **2016,** *33* (10), 2373-87.

7. Nabeshi, H.; Yoshikawa, T.; Matsuyama, K.; Nakazato, Y.; Matsuo, K.; Arimori, A.; Isobe, M.; Tochigi, S.; Kondoh, S.; Hirai, T.; Akase, T.; Yamashita, T.; Yamashita, K.; Yoshida, T.; Nagano, K.; Abe, Y.; Yoshioka, Y.; Kamada, H.; Imazawa, T.; Itoh, N.; Nakagawa, S.; Mayumi, T.; Tsunoda, S.; Tsutsumi, Y., Systemic distribution, nuclear entry and cytotoxicity of amorphous nanosilica following topical application. *Biomaterials* **2011,** *32* (11), 2713-24.

8. Burden, N.; Aschberger, K.; Chaudhry, Q.; Clift, M. J. D.; Fowler, P.; Johnston, H.; Landsiedel, R.; Rowland, J.; Stone, V.; Doak, S. H., Aligning nanotoxicology with the 3Rs: What is needed to realise the

short, medium and long-term opportunities? *Regulatory toxicology and pharmacology : RTP* **2017,** *91*, 257-266.

9. Upton, R. N.; Foster, D. J.; Abuhelwa, A. Y., An introduction to physiologically-based pharmacokinetic models. *Paediatric anaesthesia* **2016,** *26* (11), 1036-1046.

10. Sender, R.; Fuchs, S.; Milo, R., Revised Estimates for the Number of Human and Bacteria Cells in the Body. *PLoS biology* **2016,** *14* (8), e1002533.

11. Rambanapasi, C.; Barnard, N.; Grobler, A.; Buntting, H.; Sonopo, M.; Jansen, D.; Jordaan, A.; Steyn, H.; Zeevaart, J. R., Dual radiolabeling as a technique to track nanocarriers: the case of gold nanoparticles. *Molecules* **2015,** *20* (7), 12863-79.

12. Vanhecke, D.; Rodriguez-Lorenzo, L.; Clift, M. J.; Blank, F.; Petri-Fink, A.; Rothen-Rutishauser, B., Quantification of nanoparticles at the single-cell level: an overview about state-of-the-art techniques and their limitations. *Nanomedicine (Lond)* **2014,** *9* (12), 1885-900.

13. Tang, Y.; Han, S.; Liu, H.; Chen, X.; Huang, L.; Li, X.; Zhang, J., The role of surface chemistry in determining in vivo biodistribution and toxicity of CdSe/ZnS core-shell quantum dots. *Biomaterials* **2013,** *34* (34), 8741-55.

14. Liao, W. Y.; Li, H. J.; Chang, M. Y.; Tang, A. C.; Hoffman, A. S.; Hsieh, P. C., Comprehensive characterizations of nanoparticle biodistribution following systemic injection in mice. *Nanoscale* **2013,** *5* (22), 11079-86.

15. Mahmoudi, M.; Saeedi-Eslami, S. N.; Shokrgozar, M. A.; Azadmanesh, K.; Hassanlou, M.; Kalhor, H. R.; Burtea, C.; Rothen-Rutishauser, B.; Laurent, S.; Sheibani, S.; Vali, H., Cell "vision": complementary factor of protein corona in nanotoxicology. *Nanoscale* **2012,** *4* (17), 5461-8.

16. National Science and Technology Council Committee on Technology; Nanoscale Science, E., and Technology (NSET) Subcommittee,. National Nanotechnology Initiative Strategic Plan. **2016**.

17. National Science and Technology Council Committee on Technology, Environmental, health, and safety research strategy. **2011**.

18. 2018, U., Strategic Plan to Promote the Development and Implementation of Alternative Test Methods Within the TSCA Program. Interior, U. S. D. o. t., Ed. Office of Chemical Safety and Pollution Prevention: Washington, DC, 2018.

19. Services, U. S. D. o. H. a. H., Drug Products, Including Biological Products, that Contain Nanomaterials. *Guidance for Industry* **2017**.

20. van der Laan, J. W.; Chapin, R. E.; Haenen, B.; Jacobs, A. C.; Piersma, A., Testing strategies for embryo-fetal toxicity of human pharmaceuticals. Animal models vs. in vitro approaches: a workshop report. *Regulatory toxicology and pharmacology : RTP* **2012,** *63* (1), 115-23.

21. Brown, R. P.; Delp, M. D.; Lindstedt, S. L.; Rhomberg, L. R.; Beliles, R. P., Physiological Parameter Values for Physiologically Based Pharmacokinetic Models. *Toxicology and Industrial Health* **1997,** *13* (4), 407-482.

22. Wagner, C.; Zhao, P.; Pan, Y.; Hsu, V.; Grillo, J.; Huang, S. M.; Sinha, V., Application of Physiologically Based Pharmacokinetic (PBPK) Modeling to Support Dose Selection: Report of an FDA Public Workshop on PBPK. *CPT: pharmacometrics & systems pharmacology* **2015,** *4* (4), 226-30.

23. Malmborg, J.; Ploeger, B. A., Predicting human exposure of active drug after oral prodrug administration, using a joined in vitro/in silico-in vivo extrapolation and physiologically-based pharmacokinetic modeling approach. *Journal of pharmacological and toxicological methods* **2013,** *67* (3), 203-13.

24. Peyret, T.; Poulin, P.; Krishnan, K., A unified algorithm for predicting partition coefficients for PBPK modeling of drugs and environmental chemicals. *Toxicology and applied pharmacology* **2010,** *249* (3), 197-207.

25. Bannan, C. C.; Calabro, G.; Kyu, D. Y.; Mobley, D. L., Calculating Partition Coefficients of Small Molecules in Octanol/Water and Cyclohexane/Water. *Journal of chemical theory and computation* **2016,** *12* (8), 4015-24.

26. McSweeney, M. D.; Wessler, T.; Price, L. S. L.; Ciociola, E. C.; Herity, L. B.; Piscitelli, J. A.; Zamboni, W. C.; Forest, M. G.; Cao, Y.; Lai, S. K., A minimal physiologically based pharmacokinetic model that predicts anti-PEG IgG-mediated clearance of PEGylated drugs in human and mouse. *Journal of controlled release : official journal of the Controlled Release Society* **2018,** *284*, 171-178.

27. Carlander, U.; Li, D.; Jolliet, O.; Emond, C.; Johanson, G., Toward a general physiologically-based pharmacokinetic model for intravenously injected nanoparticles. *International journal of nanomedicine* **2016,** *11*, 625-40.

28. Li, D.; Johanson, G.; Emond, C.; Carlander, U.; Philbert, M.; Jolliet, O., Physiologically based pharmacokinetic modeling of polyethylene glycol-coated polyacrylamide nanoparticles in rats. *Nanotoxicology* **2014,** *8 Suppl 1*, 128-37.

29. Lin, Z.; Monteiro-Riviere, N. A.; Riviere, J. E., A physiologically based pharmacokinetic model for polyethylene glycol-coated gold nanoparticles of different sizes in adult mice. *Nanotoxicology* **2015**.

30. Lin, Z.; Monteiro-Riviere, N. A.; Kannan, R.; Riviere, J. E., A computational framework for interspecies pharmacokinetics, exposure and toxicity assessment of gold nanoparticles. *Nanomedicine* **2016,** *11* (2), 107-119.

31. Praetorius, A.; Tufenkji, N.; Goss, K.-U.; Scheringer, M.; von der Kammer, F.; Elimelech, M., The road to nowhere: equilibrium partition coefficients for nanoparticles. *Environ. Sci.: Nano* **2014,** *1* (4), 317-323.

32. Beddoes, C. M.; Case, C. P.; Briscoe, W. H., Understanding nanoparticle cellular entry: A physicochemical perspective. *Advances in colloid and interface science* **2015,** *218*, 48-68.

33. Ahn, S.; Seo, E.; Kim, K.; Lee, S. J., Controlled cellular uptake and drug efficacy of nanotherapeutics. *Scientific reports* **2013,** *3*, 1997.

34. Treuel, L.; Jiang, X.; Nienhaus, G. U., New views on cellular uptake and trafficking of manufactured nanoparticles. *Journal of the Royal Society, Interface / the Royal Society* **2013,** *10* (82), 20120939.

35. Li, M.; Zou, P.; Tyner, K.; Lee, S., Physiologically Based Pharmacokinetic (PBPK) Modeling of Pharmaceutical Nanoparticles. *The AAPS journal* **2017,** *19* (1), 26-42.

36. Baxter, L. T.; Zhu, H.; Mackensen, D. G.; Jain, R. k., Physiologically Based Pharmacokinetic Model for Specific and Nonspecific Monoclonal Antibodies and Fragments in Normal Tissues and Human Tumor Xenografts in Nude Mice. *Cancer Research* **1994,** *54*, 1517-1528.

37. Covell, D. G.; Barbet, J.; Holton, O. D.; Black, C. D. V.; Parker, R. J.; Weinstein, J. N., Pharmacokinetics of Monoclonal Immunoglobulin d, F(ab')2, and Fab' in Mice. *Cancer Research* **1986,** *46*, 3969-3978.

38. Garg, A.; Balthasar, J. P., Physiologically-based pharmacokinetic (PBPK) model to predict IgG tissue kinetics in wild-type and FcRn-knockout mice. *J Pharmacokinet Pharmacodyn* **2007,** *34* (5), 687-709.

39. Shen, T.; Guan, S.; Gan, Z.; Zhang, G.; Yu, Q., Polymeric Micelles with Uniform Surface Properties and Tunable Size and Charge: Positive Charges Improve Tumor Accumulation. *Biomacromolecules* **2016,** *17* (5), 1801-10.

40. Bachler, G.; Losert, S.; Umehara, Y.; von Goetz, N.; Rodriguez-Lorenzo, L.; Petri-Fink, A.; Rothen-Rutishauser, B.; Hungerbuehler, K., Translocation of gold nanoparticles across the lung epithelial tissue barrier: Combining in vitro and in silico methods to substitute in vivo experiments. *Part Fibre Toxicol* **2015,** *12*, 18.

41. Henrique Silva, A.; Lima Jr, E.; Vasquez Mansilla, M.; Zysler, R. D.; Mojica Pisciotti, M. L.; Locatelli, C.; Kumar Reddy Rajoli, R.; Owen, A.; Creczynski-Pasa, T. B.; Siccardi, M., A physiologically based pharmacokinetic model to predict the superparamagnetic iron oxide nanoparticles (SPIONs) accumulation in vivo. *European Journal of Nanomedicine* **2017,** *9* (2).

42. Lai, D. Y., Limited Usefulness of In Vitro Toxicity Data in Hazard Identification of Nanomaterials. *Open Access Journal of Toxicology* **2017,** *1* (2).

43. Jing, X.; Park, J. H.; Peters, T. M.; Thorne, P. S., Toxicity of copper oxide nanoparticles in lung epithelial cells exposed at the air-liquid interface compared with in vivo assessment. *Toxicology in vitro : an international journal published in association with BIBRA* **2015,** *29* (3), 502-11.

44. Vanhecke, D.; Rodriguez-Lorenzo, L.; Clift, M. J. D.; Blank, F.; Petri-Fink, A.; Rothen-Rutishauser, B., Quantification of nanoparticles at the single-cell level: an overview about state-of-the-art techniques and their limitations. *Nanomedicine* **2014,** *9* (12), 1885-1900.

45. Monteiro-Riviere, N. A.; Inman, A. O.; Zhang, L. W., Limitations and relative utility of screening assays to assess engineered nanoparticle toxicity in a human cell line. *Toxicology and applied pharmacology* **2009,** *234* (2), 222-35.

46. Collins, A. R.; Annangi, B.; Rubio, L.; Marcos, R.; Dorn, M.; Merker, C.; Estrela-Lopis, I.; Cimpan, M. R.; Ibrahim, M.; Cimpan, E.; Ostermann, M.; Sauter, A.; Yamani, N. E.; Shaposhnikov, S.; Chevillard, S.; Paget, V.; Grall, R.; Delic, J.; de-Cerio, F. G.; Suarez-Merino, B.; Fessard, V.; Hogeveen, K. N.; Fjellsbo, L. M.; Pran, E. R.; Brzicova, T.; Topinka, J.; Silva, M. J.; Leite, P. E.; Ribeiro, A. R.; Granjeiro, J. M.; Grafstrom, R.; Prina-Mello, A.; Dusinska, M., High throughput toxicity screening and intracellular detection of nanomaterials. *Wiley interdisciplinary reviews. Nanomedicine and nanobiotechnology* **2016**.

47. Gutierrez, L.; Romero, S.; da Silva, G. B.; Costo, R.; Vargas, M. D.; Ronconi, C. M.; Serna, C. J.; Veintemillas-Verdaguer, S.; Del Puerto Morales, M., Degradation of magnetic nanoparticles mimicking

lysosomal conditions followed by AC susceptibility. *Biomedizinische Technik. Biomedical engineering* **2015,** *60* (5), 417-25.

48. Chapman, K. L.; Holzgrefe, H.; Black, L. E.; Brown, M.; Chellman, G.; Copeman, C.; Couch, J.; Creton, S.; Gehen, S.; Hoberman, A.; Kinter, L. B.; Madden, S.; Mattis, C.; Stemple, H. A.; Wilson, S., Pharmaceutical toxicology: designing studies to reduce animal use, while maximizing human translation. *Regulatory toxicology and pharmacology : RTP* **2013,** *66* (1), 88-103.

49. Teeguarden, J. G.; Mikheev, V. B.; Minard, K. R.; Forsythe, W. C.; Wang, W.; Sharma, G.; Karin, N.; Tilton, S. C.; Waters, K. M.; Asgharian, B.; Price, O. R.; Pounds, J. G.; Thrall, a. B. D., Comparative iron oxide nanoparticle cellular dosimetry and response in mice by the inhalation and liquid cell culture exposure routes. *Part Fibre Toxicol* **2014,** *11*, 46.

50. Mercer, R. R.; Scabilloni, J. F.; Wang, L.; Battelli, L. A.; Antonini, J. M.; Roberts, J. R.; Qian, Y.; Sisler, J. D.; Castranova, V.; Porter, D. W.; Hubbs, A. F., The Fate of Inhaled Nanoparticles: Detection and Measurement by Enhanced Dark-field Microscopy. *Toxicologic pathology* **2018,** *46* (1), 28-46.

51. Kang, G. S.; Gillespie, P. A.; Chen, L. C., Inhalation exposure to nickel hydroxide nanoparticles induces systemic acute phase response in mice. *Toxicological research* **2011,** *27* (1), 19-23.

52. Monse, C.; Hagemeyer, O.; Raulf, M.; Jettkant, B.; van Kampen, V.; Kendzia, B.; Gering, V.; Kappert, G.; Weiss, T.; Ulrich, N.; Marek, E. M.; Bunger, J.; Bruning, T.; Merget, R., Concentration-dependent systemic response after inhalation of nano-sized zinc oxide particles in human volunteers. *Part Fibre Toxicol* **2018,** *15* (1), 8.

53. Roberts, J. R.; Mercer, R. R.; Stefaniak, A. B.; Seehra, M. S.; Geddam, U. K.; Chaudhuri, I. S.; Kyrlidis, A.; Kodali, V. K.; Sager, T.; Kenyon, A.; Bilgesu, S. A.; Eye, T.; Scabilloni, J. F.; Leonard, S. S.; Fix, N. R.; Schwegler-Berry, D.; Farris, B. Y.; Wolfarth, M. G.; Porter, D. W.; Castranova, V.; Erdely, A., Evaluation

of pulmonary and systemic toxicity following lung exposure to graphite nanoplates: a member of the graphene-based nanomaterial family. *Part Fibre Toxicol* **2016,** *13* (1), 34.

54. Gosens, I.; Kermanizadeh, A.; Jacobsen, N. R.; Lenz, A. G.; Bokkers, B.; de Jong, W. H.; Krystek, P.; Tran, L.; Stone, V.; Wallin, H.; Stoeger, T.; Cassee, F. R., Comparative hazard identification by a single dose lung exposure of zinc oxide and silver nanomaterials in mice. *PloS one* **2015,** *10* (5), e0126934.

55. Phillips, J. I.; Green, F. Y.; Davies, J. C.; Murray, J., Pulmonary and systemic toxicity following exposure to nickel nanoparticles. *American journal of industrial medicine* **2010,** *53* (8), 763-7.

56. Henrique Silva, A.; Lima Jr, E.; Vasquez Mansilla, M.; Zysler, R. D.; Mojica Pisciotti, M. L.; Locatelli, C.; Kumar Reddy Rajoli, R.; Owen, A.; Creczynski-Pasa, T. B.; Siccardi, M., A physiologically based pharmacokinetic model to predict the superparamagnetic iron oxide nanoparticles (SPIONs) accumulation in vivo. *European Journal of Nanomedicine* **2017,** *9* (2), 79-90.

57. Hinderliter, P. M.; Minard, K. R.; Orr, G.; Chrisler, W. B.; Thrall, B. D.; Pounds, J. G.; Teeguarden, J. G., ISDD: A computational model of particle sedimentation, diffusion and target cell dosimetry for in vitro toxicity studies. *Part Fibre Toxicol* **2010,** *7* (1), 36.

58. Holland, J. H., *Adaptation in Natural and Artificial Systems*. University of Michigan Press: Ann Arbor, MI, USA, 1975.

59. TA, K.; VK, S.; J, S.; EJ, K.; EM, G.; AV, Z., Non-specific cellular uptake of surface-functionalized quantum dots. *Nanotechnology* **2010,** *21* (28).

60. SJ, S.; S, A.; BB, M.; T, A.; Z, H.; SC, D. S.; K, B., The Effect of Intracellular Degradation on Cytotoxicity and Cell Labeling Efficacy of Inorganic Ligand-Stabilized Colloidal CdSe/CdS Quantum Dots. *Journal of Biomedical Nanotechnology* **2015,** *11* (4), 631-643.

61. Wang, Z. G.; Liu, S. L.; Hu, Y. J.; Tian, Z. Q.; Hu, B.; Zhang, Z. L.; Pang, D. W., Dissecting the Factors Affecting the Fluorescence Stability of Quantum Dots in Live Cells. *ACS applied materials & interfaces* **2016,** *8* (13), 8401-8.

62. Council, N. R., *Toxicity Testing in the 21st Century: A Vision and a Strategy*. The National Academies Press: Washington, DC, 2007; p 216.

63. Soenen, S. J.; Abe, S.; Manshian, B. B.; Aubert, T.; Hens, Z.; Smedt, S. C. D.; Braeckmans, K., The Effect of Intracellular Degradation on Cytotoxicity and Cell Labeling Efficacy of Inorganic Ligand-Stabilized Colloidal CdSe/CdS Quantum Dots. *Journal of Biomedical Nanotechnology* **2015,** *11* (4), 631-643.

64. Groothuis, F. A.; Heringa, M. B.; Nicol, B.; Hermens, J. L.; Blaauboer, B. J.; Kramer, N. I., Dose metric considerations in in vitro assays to improve quantitative in vitro-in vivo dose extrapolations. *Toxicology* **2015,** *332*, 30-40.

65. Lai, D. Y., Limited Usefulness of In Vitro Toxicity Data in Hazard Identification of Nanomaterials. *Open Access Journal of Toxicology* **2017,** *1* (2), 555559.

66. Gutiérrez, L.; Romero, S.; da Silva Gustavo, B.; Costo, R.; Vargas Maria, D.; Ronconi Célia, M.; Serna Carlos, J.; Veintemillas-Verdaguer, S.; del Puerto Morales, M., Degradation of magnetic nanoparticles mimicking lysosomal conditions followed by AC susceptibility. In *Biomedical Engineering / Biomedizinische Technik*, 2015; Vol. 60, p 417.

67. Collins, A. R.; Annangi, B.; Rubio, L.; Marcos, R.; Dorn, M.; Merker, C.; Estrela-Lopis, I.; Cimpan, M. R.; Ibrahim, M.; Cimpan, E.; Ostermann, M.; Sauter, A.; Yamani, N. E.; Shaposhnikov, S.; Chevillard, S.; Paget, V.; Grall, R.; Delic, J.; de-Cerio, F. G.; Suarez-Merino, B.; Fessard, V.; Hogeveen, K. N.; Fjellsbo, L. M.; Pran, E. R.; Brzicova, T.; Topinka, J.; Silva, M. J.; Leite, P. E.; Ribeiro, A. R.; Granjeiro, J. M.; Grafstrom,

R.; Prina-Mello, A.; Dusinska, M., High throughput toxicity screening and intracellular detection of nanomaterials. *Wiley Interdiscip Rev Nanomed Nanobiotechnol* **2017,** *9* (1), e1413.

68. Weldon, B. A.; Griffith, W. C.; Workman, T.; Scoville, D. K.; Kavanagh, T. J.; Faustman, E. M., In vitro to in vivo benchmark dose comparisons to inform risk assessment of quantum dot nanomaterials. *Wiley Interdiscip Rev Nanomed Nanobiotechnol* **2018**, e1507.

69. Kelf, T. A.; Sreenivasan, V. K. A.; J Sun1, E. J. K.; Goldys, E. M.; Zvyagin, A. V., Non-specific cellular uptake of surface-functionalized quantum dots. *PACS* **2010,** *42* (62).

70. Doiron, A. L.; Clark, B.; Rinker, K. D., Endothelial nanoparticle binding kinetics are matrix and size dependent. *Biotechnology and bioengineering* **2011,** *108* (12), 2988-98.

71. Walczak, A. P.; Kramer, E.; Hendriksen, P. J.; Helsdingen, R.; van der Zande, M.; Rietjens, I. M.; Bouwmeester, H., In vitro gastrointestinal digestion increases the translocation of polystyrene nanoparticles in an in vitro intestinal co-culture model. *Nanotoxicology* **2015,** *9* (7), 886-94.

72. Serdiuk, T.; Alekseev, S.; Lysenko, V.; Skryshevsky, V.; Geloen, A., Trypsinization-dependent cell labeling with fluorescent nanoparticles. *Nanoscale research letters* **2014,** *9* (1), 568.

73. Zhu, Z.-J.; Yeh, Y.-C.; Tang, R.; Yan, B.; Tamayo, J.; Vachet, R. W.; Rotello, V. M., Stability of quantum dots in live cells. *Nature Chemistry* **2011,** *3*, 963-968.

74. Derfus, A. M.; Chan, W. C. W.; Bhatia, S. N., Probing the Cytotoxicity of Semiconductor Quantum Dots. *Nano Letters* **2004,** *4* (1), 11-18.

75. NAFTA, (Quantitative) Structure Activity Relationship [(Q)SAR] Guidance Document **2012**.

76. DAI, W.; SHAN, X.-Y.; HE, G.-Y.; CHENa, H.-Q., PREDICTION FOR CELLULAR UPTAKE OF MANUFACTURED NANOPARTICLES TO PANCREATIC CANCER CELLS. *Academia Romana* **2015,** *60* (4), 367-370.

77. Papa, E.; Doucetb, J. P.; Doucet-Panayeb, A., Computational approaches for the prediction of the selective uptake of magnetofluorescent nanoparticles into human cells. *RSC Advances* **2016,** *6*, 68806-68818.

78. Basant, N.; Gupta, S., Modeling uptake of nanoparticles in multiple human cells using structure-activity relationships and intercellular uptake correlations. *Nanotoxicology* **2017,** *11* (1), 20-30.

79. Epa, V. C.; Burden, F. R.; Tassa, C.; Weissleder, R.; Shaw, S.; Winkler, D. A., Modeling biological activities of nanoparticles. *Nano letters* **2012,** *12* (11), 5808-12.

80. Shah, D. K.; Betts, A. M., Towards a platform PBPK model to characterize the plasma and tissue disposition of monoclonal antibodies in preclinical species and human. *Journal of pharmacokinetics and pharmacodynamics* **2012,** *39* (1), 67-86.

81. Curry, F. E., A Hydrodynamic Description of the Osmotic Reflection Coefficient with Application to the Pore Theory of Transcapillary Exchange. *Microvascular Research* **1974,** *8*, 236-252.

82. Pappenheimer, J. R.; Renkin, E. M.; Borrero, L. M., Filtration, Diffusion and Molecular Sieving Through Peripheral Capillary Membranes. *Capillary Permeability* **1951,** *167*.

83. Bassingthwaighte, J. B., A practical extension of hydrodynamic theory of porous transport for hydrophilic solutes. *Microcirculation* **2006,** *13* (2), 111-8.

84. Sohlenius-Sternbeck, A. K., Determination of the hepatocellularity number for human, dog, rabbit, rat and mouse livers from protein concentration measurements. *Toxicology in vitro : an international journal published in association with BIBRA* **2006,** *20* (8), 1582-6.

85. Armbrust, T.; Ramadori, G., Functional characterization of two different Kupffer cell populations of normal rat liver. *Journal of Hepatology* **1996,** *25*, 518-528.

86. Heuff, G.; Meyer, S.; Beelen, R. H. J., Isolation of rat and human Kupffer cells by a modified enzymatic assay. *Journal of Immunological Methods* **1994,** *174*, 61-65.

87. Sarin, H., Physiologic upper limits of pore size of different blood capillary types and another perspective on the dual pore theory of microvascular permeability. *Journal of Angiogenesis Research* **2010,** *2* (1), 14.

88. Posel, C.; Moller, K.; Frohlich, W.; Schulz, I.; Boltze, J.; Wagner, D. C., Density gradient centrifugation compromises bone marrow mononuclear cell yield. *PloS one* **2012,** *7* (12), e50293.

89. Nombela-Arrieta, C.; Manz, M. G., Quantification and three-dimensional microanatomical organization of the bone marrow. *The American Society of Hematology* **2017,** *1* (6), 407-416.

90. Okada, H.; Takemura, G.; Suzuki, K.; Oda, K.; Takada, C.; Hotta, Y.; Miyazaki, N.; Tsujimoto, A.; Muraki, I.; Ando, Y.; Zaikokuji, R.; Matsumoto, A.; Kitagaki, H.; Tamaoki, Y.; Usui, T.; Doi, T.; Yoshida, T.; Yoshida, S.; Ushikoshi, H.; Toyoda, I.; Ogura, S., Three-dimensional ultrastructure of capillary endothelial glycocalyx under normal and experimental endotoxemic conditions. *Critical care* **2017,** *21* (1), 261.

91. Stone, K. C.; Mercer, R. R.; Gehr, P.; Stockstill, B.; Crapo, J. D., Allometric relationships of cell numbers and size in the mammalian lung. *American journal of respiratory cell and molecular biology* **1992,** *6* (2), 235-43.

92. Townsley, M. I., Structure and composition of pulmonary arteries, capillaries, and veins. *Comprehensive Physiology* **2012,** *2* (1), 675-709.

93. Bertram, J. F.; Soosaipillai, M. C.; Ricardo, S. D.; Ryan, G. B., Total numbers of glomeruli and individual glomerular cell types in the normal rat kidney. *Cell & Tissue Research* **1992,** *270*, 37-45.

94. Kirkman, H., THE NUMBER AND DISTRIBUTION OF MACROPHAGES AND FIBROBLASTS IN KIDNEYS OF ALBINO RATS WITH EMPHASIS ON TWENTY-FIVE DAY MALES. *KIDNEY MACROPHAGES AND FIBROBLASTS* **1943**, 455-481.

95. Fujita, T.; Tokunaga, J.; Edanaga, M., Scanning Electron Microscopy of the Glomerular Filtration Membrane in the Rat Kidney. *Cell and Tissue Research* **1976,** *166*, 299-314.

96. Herculano-Houzel, S.; Lent, R., Isotropic fractionator: a simple, rapid method for the quantification of total cell and neuron numbers in the brain. *The Journal of neuroscience : the official journal of the Society for Neuroscience* **2005,** *25* (10), 2518-21.

97. Gabrusiewicz, K.; Ellert-Miklaszewska, A.; Lipko, M.; Sielska, M.; Frankowska, M.; Kaminska, B., Characteristics of the alternative phenotype of microglia/macrophages and its modulation in experimental gliomas. *PloS one* **2011,** *6* (8), e23902.

98. Pinto, A. R.; Ilinykh, A.; Ivey, M. J.; Kuwabara, J. T.; D'Antoni, M. L.; Debuque, R.; Chandran, A.; Wang, L.; Arora, K.; Rosenthal, N. A.; Tallquist, M. D., Revisiting Cardiac Cellular Composition. *Circulation research* **2016,** *118* (3), 400-9.

99. Epelman, S.; Lavine, K. J.; Beaudin, A. E.; Sojka, D. K.; Carrero, J. A.; Calderon, B.; Brija, T.; Gautier, E. L.; Ivanov, S.; Satpathy, A. T.; Schilling, J. D.; Schwendener, R.; Sergin, I.; Razani, B.; Forsberg, E. C.; Yokoyama, W. M.; Unanue, E. R.; Colonna, M.; Randolph, G. J.; Mann, D. L., Embryonic and adult-derived resident cardiac macrophages are maintained through distinct mechanisms at steady state and during inflammation. *Immunity* **2014,** *40* (1), 91-104.

100. Weihe, E.; Kalmbach, P., Ultrastructure of Capillaries in the Conduction System of the Heart in Various Mammals. *Cell and Tissue Research* **1978,** *192*, 77-87.

101. Zoubi, S. A.; Williams, M. D.; Mayhew, T. M.; Sparrow, R. A., Number and ultrastructure of epithelial cells in crypts and villi along the streptozotocin-diabetic small intestine: a quantitative study on the effects of insulin and aldose reductase inhibition. *Virchows Arch* **1995,** *427*, 187-193.

102. Gutschmidt, S.; Sandforth, F.; Riecken, E. O., Segmental variations in the surface architecture of the normal rat colonic mucosa. *Cell Pathol* **1983,** *43*, 349-354.

103. LEE, S.-H.; STARKEY, P. M.; GORDON, S., QUANTITATIVE ANALYSIS OF TOTAL MACROPHAGE CONTENT IN ADULT MOUSE TISSUES. *J. Exp. Med.* **1985,** *161*, 475-489.

104. SKINNER, S. A.; O'BRIEN, P. E., The Microvascular Structure of the Normal Colon in Rats and Humans. *Journal of Surgical Research* **1996,** *61*, 482-490.

105. SIMIONESCU, M.; SIMIONESCU, N.; PALADE, G. E., MORPHOMETRIC DATA ON THE ENDOTHELIUM OF BLOOD CAPILLARIES. *The Journal of Cell Biology* **1974,** *60*, 128-152.

106. Newman, T. N.; Liverani, E.; Ivanova, E.; Russo, G. L.; Carpino, N.; Ganea, D.; Safadi, F.; Kunapuli, S. P.; Tsygankov, A. Y., Members of the novel UBASH3/STS/TULA family of cellular regulators suppress T-cell-driven inflammatory responses in vivo. *Immunology and cell biology* **2014,** *92* (10), 837-50.

107. Inra, C. N.; Zhou, B. O.; Acar, M.; Murphy, M. M.; Richardson, J.; Zhao, Z.; Morrison, S. J., A perisinusoidal niche for extramedullary haematopoiesis in the spleen. *Nature* **2015,** *527* (7579), 466-471.

108. Neef, K.; Treskes, P.; Xu, G.; Drey, F.; Srinivasan, S. P.; Saric, T.; Nembo, E.; Semmler, J.; Nguemo, F.; Stamm, C.; Cowan, D. B.; Deppe, A.-C.; Scherner, M.; ThorstenWittwer; Hescheler, J.; ThorstenWahlers; Choi, Y.-H., Dynamic Support Culture of Murine Skeletal Muscle-Derived Stem Cells Improves Their Cardiogenic Potential In Vitro. *Stem Cells International* **2015,** *2015*.

109. Brigitte, M.; Schilte, C.; Plonquet, A.; Baba-Amer, Y.; Henri, A.; Charlier, C.; Tajbakhsh, S.; Albert, M.; Gherardi, R. K.; Chretien, F., Muscle resident macrophages control the immune cell reaction in a mouse model of notexin-induced myoinjury. *Arthritis and rheumatism* **2010,** *62* (1), 268-79.

110. Korneliussen, H., Fenestrated Blood Capillaries and Lymphatic Capillaries in Rat Skeletal Muscle. *Cell Tiss. Res.* **1975,** *163*, 169-174.

111. Chorro, L.; Geissmann, F., Development and homeostasis of 'resident' myeloid cells: the case of the Langerhans cell. *Trends in immunology* **2010,** *31* (12), 438-45.

112. Monteiro-Riviere, N. A.; Bristol, D. G.; Manning, T. O.; Rogers, R. A.; Riviere, J. E., Interspecies and Interregional Analysis of the Comparative Histologic Thickness and Laser Doppler Blood Flow

Measurements at Five Cutaneous Sites in Nine Species. *Journal of Investigative Dermatology* **1990,** *95* (5), 582-586.

113. Kobayashi, M.; Asano, H.; Fujita, Y.; Hoshino, T., Development of ATPase-positive, immature Langerhans cells in the fetal mouse epidermis and their maturation during the early postnatal period. *Cell and Tissue Research* **1987,** *248*, 315-322.

114. Bianconi, E.; Piovesan, A.; Facchin, F.; Beraudi, A.; Casadei, R.; Frabetti, F.; Vitale, L.; Pelleri, M. C.; Tassani, S.; Piva, F.; Perez-Amodio, S.; Strippoli, P.; Canaider, S., An estimation of the number of cells in the human body. *Annals of human biology* **2013,** *40* (6), 463-71.

115. Imayama, S., Scanning and Transmission Electron Microscope Study on the Terminal Blood Vessels of the Rat Skin. *Journal of Investigative Dermatology* **1981,** *76* (3), 151-157.

116. Weldon, B. A.; Griffith, W. C.; Workman, T.; Scoville, D. K.; Kavanagh, T. J.; Faustman, E. M., In vitro to in vivo benchmark dose comparisons to inform risk assessment of quantum dot nanomaterials. *Wiley interdisciplinary reviews. Nanomedicine and nanobiotechnology* **2018**.

117. Tsang, M. P.; Hristozov, D.; Zabeo, A.; Koivisto, A. J.; Jensen, A. C. O.; Jensen, K. A.; Pang, C.; Marcomini, A.; Sonnemann, G., Probabilistic risk assessment of emerging materials: case study of titanium dioxide nanoparticles. *Nanotoxicology* **2017,** *11* (4), 558-568.

118. Pietroiusti, A.; Massimiani, M.; Fenoglio, I.; Colonna, M.; Valentini, F.; Palleschi, G.; Camaioni, A.; Magrini, A.; Siracusa, G.; Bergamaschi, A.; Sgambato, A.; Campagnolo, L., Low Doses of Pristine and Oxidized Single-Wall Carbon Nanotubes Affect Mammalian Embryonic Development. *ACS Nano* **2011,** *5* (6), 4624-4633.

119. Park, M. V.; Annema, W.; Salvati, A.; Lesniak, A.; Elsaesser, A.; Barnes, C.; McKerr, G.; Howard, C. V.; Lynch, I.; Dawson, K. A.; Piersma, A. H.; de Jong, W. H., In vitro developmental toxicity test detects

inhibition of stem cell differentiation by silica nanoparticles. *Toxicology and applied pharmacology* **2009,** *240* (1), 108-16.

120. Farcal, L.; Torres Andon, F.; Di Cristo, L.; Rotoli, B. M.; Bussolati, O.; Bergamaschi, E.; Mech, A.; Hartmann, N. B.; Rasmussen, K.; Riego-Sintes, J.; Ponti, J.; Kinsner-Ovaskainen, A.; Rossi, F.; Oomen, A.; Bos, P.; Chen, R.; Bai, R.; Chen, C.; Rocks, L.; Fulton, N.; Ross, B.; Hutchison, G.; Tran, L.; Mues, S.; Ossig, R.; Schnekenburger, J.; Campagnolo, L.; Vecchione, L.; Pietroiusti, A.; Fadeel, B., Comprehensive In Vitro Toxicity Testing of a Panel of Representative Oxide Nanomaterials: First Steps towards an Intelligent Testing Strategy. *PloS one* **2015,** *10* (5), e0127174.

121. Semmler-Behnke, M.; Lipka, J.; Wenk, A.; Hirn, S.; Schaffler, M.; Tian, F.; Schmid, G.; Oberdorster, G.; Kreyling, W. G., Size dependent translocation and fetal accumulation of gold nanoparticles from maternal blood in the rat. *Part Fibre Toxicol* **2014,** *11*, 33.

122. Amiri, S.; Yousefi-Ahmadipour, A.; Hosseini, M. J.; Haj-Mirzaian, A.; Momeny, M.; Hosseini-Chegeni, H.; Mokhtari, T.; Kharrazi, S.; Hassanzadeh, G.; Amini, S. M.; Jafarinejad, S.; Ghazi-Khansari, M., Maternal exposure to silver nanoparticles are associated with behavioral abnormalities in adulthood: Role of mitochondria and innate immunity in developmental toxicity. *Neurotoxicology* **2018,** *66*, 66-77.

123. Yamashita, K.; Yoshioka, Y.; Higashisaka, K.; KazuyaMimura; Morishita, Y.; Nozaki, M.; Yoshida, T.; Ogura, T.; Nabeshi, H.; Nagano, K.; Abe, Y.; Kamada, H.; Monobe, Y.; Imazawa, T.; Aoshima, H.; Shishido, K.; Kawai, Y.; Mayumi, T.; Tsunoda, S.-i.; Itoh, N.; Yoshikawa, T.; Yanagihara, I.; Saito, S.; Tsutsumi, Y., Silica and titanium dioxide nanoparticles cause pregnancy complications in mice. *Nature nanotechnology* **2011,** *6*, 321-328.

124. Paul, E.; Franco-Montoya, M. L.; Paineau, E.; Angeletti, B.; Vibhushan, S.; Ridoux, A.; Tiendrebeogo, A.; Salome, M.; Hesse, B.; Vantelon, D.; Rose, J.; Canoui-Poitrine, F.; Boczkowski, J.;

Lanone, S.; Delacourt, C.; Pairon, J. C., Pulmonary exposure to metallic nanomaterials during pregnancy irreversibly impairs lung development of the offspring. *Nanotoxicology* **2017,** *11* (4), 484-495.

125. Lim, J. H.; Kim, S. H.; Lee, I. C.; Moon, C.; Kim, S. H.; Shin, D. H.; Kim, H. C.; Kim, J. C., Evaluation of Maternal Toxicity in Rats Exposed to Multi-Wall Carbon Nanotubes during Pregnancy. *Environmental health and toxicology* **2011,** *26*, e2011006.

126. Organization, W. H., Characterization and Application of Physiologically Based Pharmacokinetic Models in Risk Assessment. IPCS, Ed. World Health Organization: Geneva, Switzerland, 2010; Vol. Harmonization Proect Document No. 9.

127. Scientific and Technical Assessment Report on Cadmium. Agency, U. S. E. P., Ed. National Environmental Research enter: Washington, D.C. , 1975.

128. Feng, Q.; Liu, Y.; Huang, J.; Chen, K.; Huang, J.; Xiao, K., Uptake, distribution, clearance, and toxicity of iron oxide nanoparticles with different sizes and coatings. *Scientific reports* **2018,** *8* (1), 2082.

129. WANG, B.; HE, X.; ZHANG, Z.; ZHAO, Y.; FENG, A. W., Metabolism of Nanomaterials in Vivo: Blood Circulation and Organ Clearance. *ACCOUNTS of chemical research* **2013,** *46* (3), 761-769.

130. Gustafson, H. H.; Holt-Casper, D.; Grainger, D. W.; Ghandehari, H., Nanoparticle Uptake: The Phagocyte Problem. *Nano today* **2015,** *10* (4), 487-510.

131. Alalaiwe, A.; Roberts, G.; Carpinone, P.; Munson, J.; Roberts, S., Influence of PEG coating on the oral bioavailability of gold nanoparticles in rats. *Drug delivery* **2017,** *24* (1), 591-598.

132. Chen, K. H.; Lundy, D. J.; Toh, E. K.; Chen, C. H.; Shih, C.; Chen, P.; Chang, H. C.; Lai, J. J.; Stayton, P. S.; Hoffman, A. S.; Hsieh, P. C., Nanoparticle distribution during systemic inflammation is size-dependent and organ-specific. *Nanoscale* **2015,** *7* (38), 15863-72.

133. Organization, W. H., Characterization and Application of Physiologically Based Pharmacokinetic Models in Risk Assessment. *International Programme on Chemical Safety* **2010,** *9*, 1-91.

134. Poulin, P.; Jones, H. M.; Jones, R. D.; Yates, J. W.; Gibson, C. R.; Chien, J. Y.; Ring, B. J.; Adkison, K. K.; He, H.; Vuppugalla, R.; Marathe, P.; Fischer, V.; Dutta, S.; Sinha, V. K.; Bjornsson, T.; Lave, T.; Ku, M. S., PhRMA CPCDC initiative on predictive models of human pharmacokinetics, part 1: goals, properties of the PhRMA dataset, and comparison with literature datasets. *Journal of pharmaceutical sciences* **2011,** *100* (10), 4050-73.

135. BAZIN-REDUREAU, M. I.; RENARD, C. B.; SCHERRMANN, J.-M. G., Pharmacokinetics of Heterologous and Homologous Immunoglobulin G, F(ab')2 and Fab after Intravenous - Administration in the Rat. *J. Pharm. Pharmacol.* **1997,** *49*, 277-281.

136. Vasicek, L. A.; Spellman, D. S.; Hsieh, S.; Seghezzi, W.; Zhang, S.; Santostefano, M.; Bateman, K. P., Quantitation of a Therapeutic Antibody in Serum Using Intact Sequential Affinity Capture, Trypsin Digestion, and LC-MS/MS. *Analytical chemistry* **2018,** *90* (1), 866-871.

137. Park, J.; Cho, W.; Park, H. J.; Cha, K. H.; Ha, D. C.; Choi, Y. W.; Lee, H. Y.; Cho, S. H.; Hwang, S. J., Biodistribution of newly synthesized PHEA-based polymer-coated SPION in Sprague Dawley rats as magnetic resonance contrast agent. *International journal of nanomedicine* **2013,** *8*, 4077-89.

138. Cho, W. S.; Cho, M.; Jeong, J.; Choi, M.; Cho, H. Y.; Han, B. S.; Kim, S. H.; Kim, H. O.; Lim, Y. T.; Chung, B. H.; Jeong, J., Acute toxicity and pharmacokinetics of 13 nm-sized PEG-coated gold nanoparticles. *Toxicology and applied pharmacology* **2009,** *236* (1), 16-24.

139. Chiarelli, P. A.; Revia, R. A.; Stephen, Z. R.; Wang, K.; Jeon, M.; Nelson, V.; Kievit, F. M.; Sham, J.; Ellenbogen, R. G.; Kiem, H. P.; Zhang, M., Nanoparticle Biokinetics in Mice and Nonhuman Primates. *ACS nano* **2017,** *11* (9), 9514-9524.

140. Wenger, Y.; Schneider, R. J., 2nd; Reddy, G. R.; Kopelman, R.; Jolliet, O.; Philbert, M. A., Tissue distribution and pharmacokinetics of stable polyacrylamide nanoparticles following intravenous injection in the rat. *Toxicology and applied pharmacology* **2011,** *251* (3), 181-90.

141. Tosi, G.; Vergoni, A. V.; Ruozi, B.; Bondioli, L.; Badiali, L.; Rivasi, F.; Costantino, L.; Forni, F.; Vandelli, M. A., Sialic acid and glycopeptides conjugated PLGA nanoparticles for central nervous system targeting: In vivo pharmacological evidence and biodistribution. *Journal of controlled release : official journal of the Controlled Release Society* **2010,** *145* (1), 49-57.

142. Abellan-Pose, R.; Rodriguez-Evora, M.; Vicente, S.; Csaba, N.; Evora, C.; Alonso, M. J.; Delgado, A., Biodistribution of radiolabeled polyglutamic acid and PEG-polyglutamic acid nanocapsules. *European journal of pharmaceutics and biopharmaceutics : official journal of Arbeitsgemeinschaft fur Pharmazeutische Verfahrenstechnik e.V* **2017,** *112*, 155-163.

143. Jennings, L.; Ivashchenko, O.; Marsman, I. J.; Laan, A. C.; Denkova, A. G.; Waton, G.; Beekman, F. J.; Schosseler, F.; Mendes, E., In vivo biodistribution of stable spherical and filamentous micelles probed by high-sensitivity SPECT. *Biomaterials science* **2016,** *4* (8), 1202-11.

144. Fischer, H. C.; Liu, L.; Pang, K. S.; Chan, W. C. W., Pharmacokinetics of Nanoscale Quantum Dots: In Vivo Distribution, Sequestration, and Clearance in the Rat. *Advanced Functional Materials* **2006,** *16* (10), 1299-1305.

145. Chen, Z.; Chen, H.; Meng, H.; Xing, G.; Gao, X.; Sun, B.; Shi, X.; Yuan, H.; Zhang, C.; Liu, R.; Zhao, F.; Zhao, Y.; Fang, X., Bio-distribution and metabolic paths of silica coated CdSeS quantum dots. *Toxicology and applied pharmacology* **2008,** *230* (3), 364-71.

146. Liang, X.; Wang, H.; Zhu, Y.; Zhang, R.; Cogger, V. C.; Liu, X.; Xu, Z. P.; Grice, J. E.; Roberts, M. S., Short- and Long-Term Tracking of Anionic Ultrasmall Nanoparticles in Kidney. *ACS nano* **2016,** *10* (1), 387-95.

147. Su, Y.; Peng, F.; Jiang, Z.; Zhong, Y.; Lu, Y.; Jiang, X.; Huang, Q.; Fan, C.; Lee, S. T.; He, Y., In vivo distribution, pharmacokinetics, and toxicity of aqueous synthesized cadmium-containing quantum dots. *Biomaterials* **2011,** *32* (25), 5855-62.

148. Brambell, F. W. R.; Hemmings, W. A.; Morris, I. G., A Theoretical Model of γ-Globulin Catabolism. *Nature* **1964,** *203*, 1352.

149. Henderson, L. A.; Baynes, J. W.; Thorpe, S. R., Identification of the sites of IgG catabolism in the rat. *Archives of Biochemistry and Biophysics* **1982,** *215* (1), 1-11.

150. Tan, Q.; Ferrier, G. A.; Chen, B. K.; Wang, C.; Sun, Y., Quantification of the specific membrane capacitance of single cells using a microfluidic device and impedance spectroscopy measurement. *Biomicrofluidics* **2012,** *6* (3), 34112.

151. Filippov, A. N.; Iksanov, R. K.; Volkov, A. V., Interaction of a charged spherical particle with a pore of a charged hydrophobic membrane in an electrolyte solution. *Petroleum Chemistry* **2011,** *51* (7), 536-541.

152. Lipka, J.; Semmler-Behnke, M.; Sperling, R. A.; Wenk, A.; Takenaka, S.; Schleh, C.; Kissel, T.; Parak, W. J.; Kreyling, W. G., Biodistribution of PEG-modified gold nanoparticles following intratracheal instillation and intravenous injection. *Biomaterials* **2010,** *31* (25), 6574-81.

153. Contado, C., Nanomaterials in consumer products: a challenging analytical problem. *Frontiers in chemistry* **2015,** *3*, 48.